SCHOOL OF SCIENCE
Department of Industrial Chemistry “Toso Montanari”

Master’s degree in
Industrial Chemistry

Class LM-71 – Science and Technology in Industrial Chemistry

Synthesis and surface characterization of metal (Mn, Ti) hexacyanoferrate electrodes

Experimental thesis

CANDIDATE

Francesca Sgarbi Stabellini

SUPERVISOR

Illustrious Professor Marco Giorgetti

CO-SUPERVISORS

Illustrious Professor Dr. Reinhard Denecke

M. Sc. Thomas Ruf

Dr. Min Li

Academic year 2020-2021

ABSTRACT

Due to the limited resources of lithium, new chemistries based on the abundant and cheap sodium and even zinc have been proposed for the battery market.

Prussian Blue Analogues (PBAs) are a class of compounds which have been explored for many different applications because of their intriguing electrochemical and magnetic properties.

Manganese and titanium hexacyanoferrate (MnHCF and TiHCF) belong to the class of PBAs. In this work, MnHCF and TiHCF electrodes were synthetized, cycled with cyclic voltammetry (CV) in different setups and subsequently, the surfaces were characterized with X-ray Photoelectron Spectroscopy (XPS). The setups chosen for CVs were coin cell with zinc aqueous solution for the MnHCF series, three-electrode cell and symmetric coin cell with sodium aqueous solution for the TiHCF series.

The electrodes were treated with different number of cycles to evaluate the chemical changes and alterations in oxidation states during cycling.

CONTENTS

1. INTRODUCTION

1.1. Sodium and zinc ion batteries

In 1800, Alessandro Volta realized the first electrochemical battery made with zinc and copper plates and [1] then, different types of batteries were studied and discovered, such as the Daniell cell, the alkaline battery and so on.

A battery is a power source made up of electrochemical cells that are connected in series or in parallel to provide a certain voltage and capacity. The cell is composed by a positive and a negative electrode separated by an electrolyte solution which aids the ions transfer. When a battery is connected to an external electric load, the redox reactions begin at the electrodes and the chemical energy is converted to electric energy. [2]

Today, the lithium-ion batteries (hereafter called LIBs) are widespread due to their high energy density and design flexibility. [3] The "secondary" LIBs are rechargeable, and they are commonly used for portable electronic devices and electric vehicles. LIBs have no memory effect and low self-discharge, but they can be a safety hazard since they contain flammable electrolytes. Furthermore, LIBs are expensive because the lithium resources are limited.

The sodium-ion batteries (hereafter called SIBs) have relatively low cost due to the higher abundance of sodium in nature. Since 2008, the number of research on SIBs increased rapidly and during the past years, several materials with potentially interesting insertion and release capability for sodium were tested. [4] The battery components and the electrical storage mechanism of SIBs and LiBs are basically the same except for their ion carriers. In terms of cathode materials, the intercalation chemistry of sodium is very similar to that of lithium, making it possible to use similar compounds for both systems. [5]

The zinc-ion batteries (hereafter called ZIBs) use zinc ions as charge carriers, metallic Zn as anode and zinc-intercalating materials as cathode. The ZIBs holds a high theoretical volumetric capacity and natural abundance of zinc is high. [6] Aqueous Zn-based batteries show the highest energy density at low cost and, in comparison to other high-capacity metals like Li and Ca, Zn is non-flammable, chemically stable in air and recyclable. [7]

1.2. Prussian blue and metal hexacyanoferrates

Prussian blue (hereafter called PB) was the first modern synthetic pigment, his chemical formula is $Fe_4[Fe(CN)_6]_3$ and it is dark blue. PB is also known as Berlin blue or Parisian blue, and it is used in paints as a colour [3] and in medicine as an antidote for heavy metal poisoning. [8] PB has a face centred cubic open framework formed by iron (II) and iron (III) respectively coordinated to the carbon and the nitrogen of the cyanide. [9] The structure has large interstitial site, a wide range of different intercalation ions are possible, including alkali metals, divalent ions, and even small molecules. [10]

$$– Fe^{II} – C \equiv N – Fe^{III} –$$

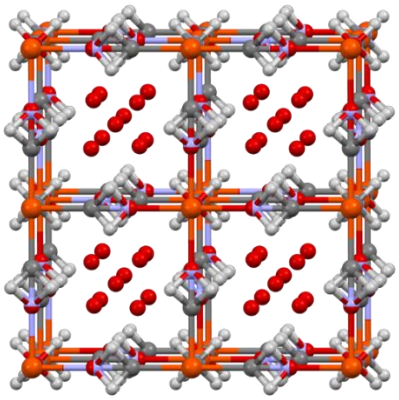

Figure 1: unit cell of Prussian Blue determined by neutron diffraction [11]

Prussian Blue Analogues (hereafter called PBAs) have been explored for many different applications because of their ease of synthesis and intriguing electrochemical and magnetic properties. Their general chemical formula is $A_xP[R(CN)_6]_{1-y}V_y \cdot nH_2O$ where A are the mobile cations, P is the transition metal coordinated to the nitrogen of the cyanide, R is the transition metal coordinated to the carbon of the cyanide and V is the vacancy ($0 \leq x \leq 2$ and $0 \leq y < 1$). PBAs have the same open-framework lattice structure of the PB where the iron is coordinated to the carbon and the other transition metal is coordinated to the nitrogen of the cyanide. [12,13]

$$– Fe – C \equiv N – M –$$

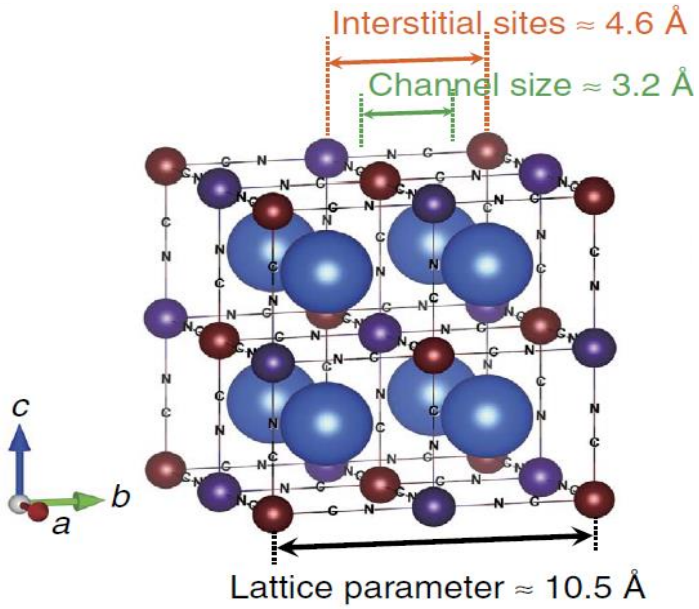

Figure 2: open-framework lattice structure for metal hexacyanoferrates. The red sphere is the iron, the dark blue sphere is the transition metal (Mn, Ti) and the big blue spheres are the large cavities inside the structure [12]

Each unit cell consists of eight subunit cells and therefore contains eight interstitial sites that can host various ions, such as Li^+, Na^+, K^+, NH^+, Rb^+, alkaline earth divalent ions and zeolitic water. The open-framework nature of the cubic structure, with contains open channels (3.2 Å in diameter) and interstitial sites (4.6 Å in diameter) in the case of PB, enables rapid solid state-diffusion of a wide variety of ions. [12]

1.3. Titanium and manganese hexacyanoferrates

Manganese hexacyanoferrate (hereafter called MnHCF) and titanium hexacyanoferrate (TiHCF) belong to the class of PBAs.

In previous work, the powder of MnHCF was studied with different techniques (XRD and XAS) and the obtained formula was $Na_{1.9}Mn_{1.1}Fe(CN)_6$. Manganese hexacyanoferrate is electroactive and it is constituted of only abundant elements. This material features high specific capacities at high potential when compared to other materials of the same class. [13,14] In MnHCF, the iron and the manganese are respectively coordinated to the carbon and to the nitrogen of the cyanide.

$$– Fe^{II} – C \equiv N – Mn^{II} –$$

In another previous work, the powder of titanium hexacyanoferrate was studied with XRD and the obtained formula for the structure was $Na_{0.86}Ti_{0.73}[Fe(CN)_6] \cdot 3H_2O$ [15]. TiHCF showed electrochemical activity: it exhibited high capacity, long cycle life and good rate capability. [16] In TiHCF, the iron is coordinated to the carbon of the cyanide and the titanium is coordinated to the nitrogen of the cyanide.

$$– Fe^{II} – C \equiv N – Ti^{IV} –$$

1.4. Electrochemical cell and Cyclic Voltammetry (CV)

An electrochemical cell is a device that generates electrical energy by performing chemical reactions (galvanic cell) or it uses electrical energy to supply it, facilitating chemical reactions in it (electrolytic cell). The electrolytic cell converts electrical energy into chemical energy and the species are oxidized at the cathode and reduced at the anode. [17]

Cyclic voltammetry (CV) is an electrochemical technique used for qualitative and quantitative analyses of redox couples. With this method, it is possible to determine the reaction mechanism, the stability of the reaction products, the presence of intermediates in redox reactions, the kinetics of the electron transfer and so on. The electrode potential is ramped linearly versus time starting from an initial potential (E_i) until the final potential (E_f) then, the potential scan is performed in the opposite direction back to E_i. These cycles of ramps in potential may be repeated as many times as needed. [18]

Usually, CV measurements applied to the batteries are split in two segments: the first is the "charge" and the second one is the "discharge". During the charge segment there is the oxidation of the species, while they are reduced during the discharge part. In the case of a reversible redox couple, an oxidation peak in the charge segment as well as a reduction peak in the discharge part are observed. The more reversible is the redox couple, the more similar the oxidation peak will be in shape to the reduction peak. [4]

When the potential is scanned during the cyclic voltammetry experiment, the concentration of the species in solution near the electrode changes over the time in accordance with the Nernst equation (1):

$$E = E^0 + {}^{RT}/_{nF} \cdot \ln {}^{Ox}/_{Red} \qquad (1)$$

where:

- E is the cell potential at the temperature of interest (V).
- E^0 is the standard cell potential (V).
- R is the universal gas constant ($8.31\ ^{J}/_{K\ \cdot\ mol}$).
- T is the temperature (K).
- N is the number of electrons transferred in the cell reaction.
- F is the Faraday constant, the number of coulombs per mole of electrons ($96485\ ^{C}/_{mol}$).
- Ox is the concentration of the oxidized species.
- Red is the concentration of the reduced species.

As a first approximation, for a solid electrode inserted in a solution containing electroactive species, if a negative potential is applied the species are reduced locally at the electrode, resulting in the measurement of a current and depletion of oxidized species at the electrode surface. Crucially, the concentration of the species relative to the distance from the surface of the electrode are dependent on the potential applied and how species move between the surface and the bulk solution. These factors all contribute to the "duck"-shaped voltammograms. The two peaks are separated due to the diffusion of the analyte to and from the electrode. If the reduction process is chemically and electrochemically reversible, the difference between the anodic and the cathodic peak potentials (ΔE_p) is 59 mV. [19]

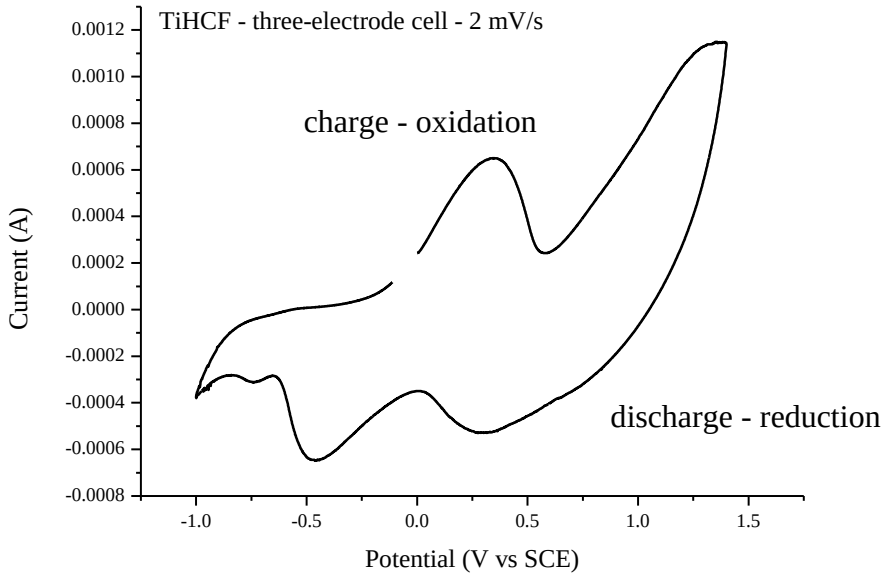

Figure 3: cyclic voltammogram scan with charge and discharge segments for TiHCF pellet pressed inside the aluminium mesh in the three-electrode cell (scan rate = 2 mV/s)

The peak current, I_p, of the reversible redox process is described by the Randles-Sevcik equation at 298 K (2):

$$I_p = (2.69 \cdot 10^5) \cdot n^{3/2} \cdot A \cdot C \cdot D^{1/2} \cdot v^{1/2} \quad (2)$$

where:

- n is the number of electrons.
- A is the electrode area (cm^2).
- C is the concentration (mol/cm^3).
- D is the diffusion coefficient (cm^2/s).
- v is the potential scan rate (V/s). [20]

1.5. X-Ray Photoelectron Spectroscopy (XPS)

X-Ray Photoelectron Spectroscopy is a non-destructive technique used for qualitative and quantitative analysis of different samples. This technique can obtain the chemical composition of the top few atomic layers because the mean free path of electron in solid is very small (λ = 10-20 Å). In quantitative analysis by XPS, the elemental surface composition can be determined. Furthermore, a chemical analysis is possible by assigning binding energies (BE) to different chemical states. In simple cases, a higher binding energy can be attributed to a higher formal oxidation state of an element. Moreover, it is also possible to obtain depth profiles when paired with ion-beam etching. [21]

XPS analyses are performed under ultra-high vacuum (UHV-10^{-9} mbar) to guarantee a sufficient mean free path of the photoelectrons after ejection from the solid and to reduce the dissipation of energy on the surface due to the inelastic scattering, as well as adsorbed gaseous species. In an XPS spectrum different signals can be recorded, which will be further explained in the following chapters:

- Photoelectron lines: excited core electrons assigned to an element and the respective orbital.
- X-ray satellites: for each photoelectron peak that results from the routinely used Al Kα (non-monochromate) x-ray photons, there is a family of minor peaks at lower binding energies, with the intensity and spacing characteristic of the x-ray anode material.

- Shake up and shake off processes: these processes will be explained in the following chapters.
- Energy loss lines: some materials show an enhanced probability for loss of a specific amount of energy due to the interaction between the photoelectron and the other electrons on the surface of the sample. This phenomenon produces a distinct and rather sharp hump above the binding energy of the main line.
- Auger lines: the emission of an Auger electron as a relaxation process after ejection of a core electron. This mechanism is more common in light elements.
- Multiplet splitting: a final state effect after ionization of elements that already have unpaired electrons. [22]

1.5.1. Photoelectrons

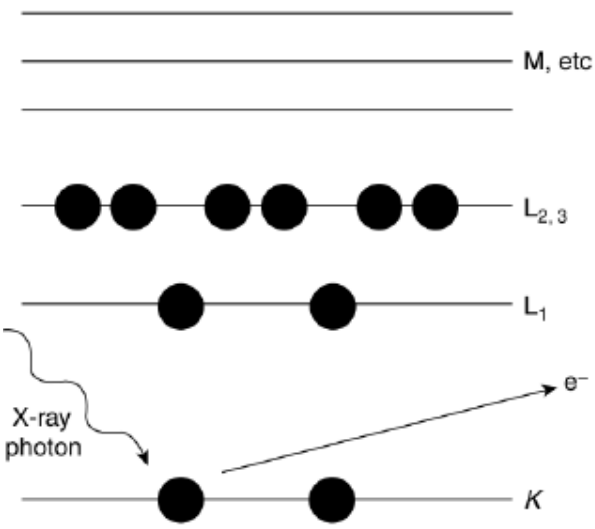

Figure 4: ejection of the photoelectron and formation of a core hole after photoionization [23]

XPS is based on the photoelectric effect (see Figure 4). It refers to what happens when electrons are emitted from a material that has adsorbed electromagnetic radiation. Inside the instrument there is an x-ray tube that produces the excitation radiation by x-ray fluorescence. The x-ray photons generated are directed to the sample and the photons interact with the electron of the material. When the x-ray photon hits the surface, it causes the ejection of a core electron.

Such an electron is called photoelectron, and its kinetic energy depends upon the energy of the incident photon as shown in Equation (3):

$$KE = h\nu - BE - \varphi \quad (3)$$

- KE is the kinetic energy of the photoelectron.
- hν is the known energy of the incident photon.
- BE is the binding energy of the atomic orbital from which the electron is originated.
- φ is the known a work function of the analyzer: it needs to be determined once and then, the kinetic energy can be recalculated as binding energy. It depends on how the KE is defined.

The BE is determined by measuring the KE with the electron energy analyzer. For homogeneous sample, the relative concentrations of the various constituents can be determined by measuring the peak area that is related to the number of atoms as follows:

$$I = nf\sigma\theta y\lambda AT \quad (4)$$

- I is the intensity of the peak (number of photoelectron per second).
- n is the number of atoms of the element per cm^3 of the sample.
- f is the x-ray flux in photons/$cm^2 \cdot$ sec.
- σ is the photoelectric cross-section for the atomic orbital of interest in cm^2.
- θ is an angular efficiency factor for the instrumental arrangement based on the angle between the photon path and detected electron.
- y is the efficiency in the photoelectric process for formation of photoelectrons of the normal photoelectron energy.
- λ is the mean free path of the photoelectrons in the sample (for homogeneous samples).
- A is the area from which photoelectrons are detected.
- T is the detection efficiency for electrons emitted from the sample. [22]

Photoelectron lines are named according to their total momentum ($J = l + s$), where $l = 0,1,2,3$ – denoted as s,p,d,f – and $s = \pm 1/2$ are quantum numbers of the core energy level from which the photoelectrons are expelled. For example: Fe $2p_{3/2}$ where $3/2 = 1 + ½ = l + s$. [24] In case of *l* being non-zero (so all orbitals apart the *s*-orbital), the electron spins can align with or opposite to the orbital momentum *l*. This results in doublet signals for all electrons expelled from non-*s* orbitals and a singlet for those *s*-orbitals core electrons.

1.5.2. Shake up and shake off processes

During the photoionization of the atom by x-rays it is possible to have “shake-up” and “shake-off” processes, both causing energy reduction of the photoelectron. During a shake off process the energy of the photoelectron is used to eject a secondary electron, whereas in the shake-up process the electron is promoted to a higher energy level. This results in the formation of a satellite peak a few electron volts higher in binding energy than the main peak. [22]

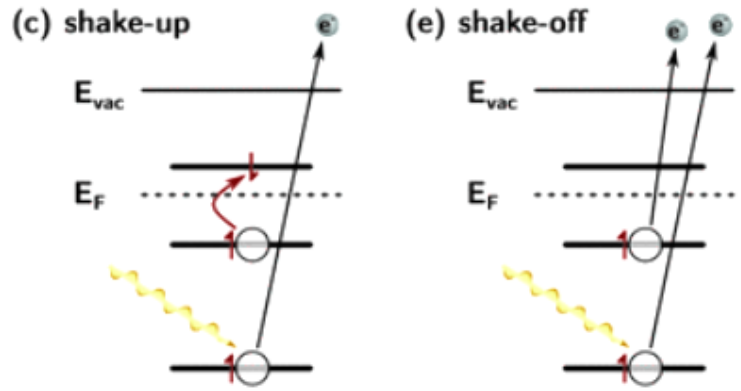

Figure 5: examples of shake up and shake off processes [25]

1.5.3. Auger electrons

After the ejection of the photoelectron, the remaining ion is energetically excited because of the vacancy in the core-level. There are two possible relaxation processes:

- emission of Auger electron: this is a frequent phenomenon for lighter elements ($Z < 75$) after photoionization and cylindrical mirror analyzer could be used to detect Auger electron emitted by the surfaces of the sample.
- x-ray fluorescence is the emission of a high energy photon after bombarding with x-rays, which is more intense for heavier elements ($Z > 75$). The related technique is X-Ray Fluorescence (XRF).

The Auger electrons are secondary electrons which are emitted after the ejection of a photoelectron from a core level in a two electron process. As in an XPS experiment, electrons of different kinetic energies are detected, signals due to Auger electrons can also be assigned.

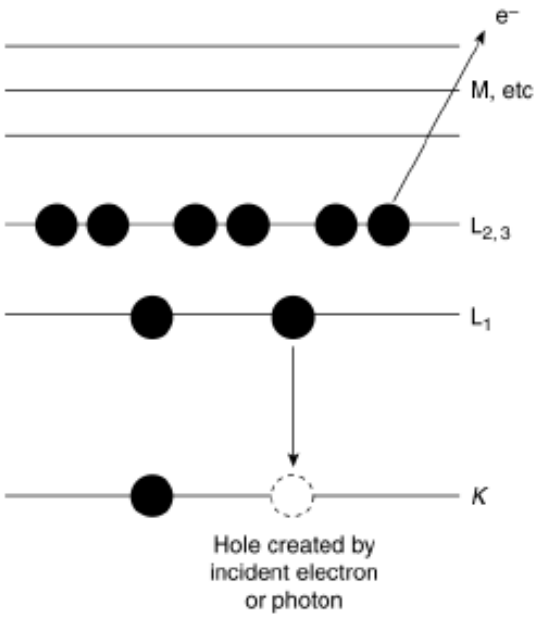

Figure 6: exemplary ejection of a KLL Auger electron [23]

This one step process includes relaxation of one electron from a higher energy orbital who fills the vacancy on the core level and the ejection of an Auger electron. The Auger electron possesses kinetic energy equal to the difference between the energy of the initial ion and the doubly charged final ion. The kinetic energy of the Auger electron is independent of the ionizing radiation; hence the kinetic energy of the Auger line will not shift if the source changes. The related technique is the Auger Electron Spectroscopy (AES).

The Auger line is identified by specifying the initial and the final vacancies in the Auger transition: the KLL series includes the processes where the initial vacancy is in the K shell and the final double vacancy is in the L shell. The electron is ejected from the K shell, then the electron on the L shell relaxes to fill the vacancy on the K shell and an Auger electron is ejected from the L shell. The final atom is doubly ionized, which is energetically more favorable than the singly ionized atom.

1.5.4. Multiplet splitting

The emission of an electron from an element that itself has unpaired spins can create a vacancy in two or more ways. After the photoionization, the coupling of the unpaired electron with other unpaired electron of the atom can create an ion with several possible final state configurations. This results in a photoelectron line which is split asymmetrically into several components. Multiplet splitting also occurs in the ionization of *p* levels, but the result is more complex and

subtle. In favorable cases, it results in an apparent slight increase in the spin doublet separation evidenced in the separation of the $2p_{1/2}$ and $2p_{3/2}$ lines in first-row transition metals and in the generation of a less easily noticed asymmetry in the line shape of the components. [22]

In the case of Fe 2p photoelectron line, iron low-spin complexes show little or no multiplet splitting, as there are no or one unpaired electron initially, depending on the oxidation state.

1.5.5. XPS quantification

The intensity of the photoelectron lines needs to be normalized to allow for quantification by comparing normalized peak areas. In the setup of this work, this is realized in the evaluation software Unifit 2021 by dividing the intensity by a sensitivity factor SF_x. This sensitivity factor is the product of the photoelectric cross-section σ_x of element x, the inelastic mean free path of the element x, λ_x and the measurement made dependent transmission function F (for homogeneous samples). The surface concentration in atomic percent of the element x is then calculated by using the Equation (5):

$$C\ (\text{at. \%}) = \frac{{}^{I_A}/_{SF_A}}{\sum {}^{I_X}/_{SF_X}} \tag{5}$$

2. EXPERIMENTS AND CHARACTERIZATION

In this chapter, the synthesis of the powder and their formulation are described. Afterwards, the pellets were treated with cyclic voltammetry and the oxidation states of the different elements were investigated with XPS analyses.

2.1 Synthesis of the metal hexacyanoferrates

2.1.1. Preparation of MnHCF powder

Manganese hexacyanoferrate powder was synthetized by co-precipitation method. The aqueous solution of manganese sulphate monohydrate (0.1 M $MnSO_4 \cdot H_2O$, Aldrich-Merk) and sodium ferrocyanide decahydrate (0.1 M $Na_4Fe(CN)_6 \cdot H_2O$, supplier Aldrich-Merk) were simultaneously dropwise poured to an aqueous solution of sodium sulphate (0.1 M Na_2SO_4, supplier Aldrich-Merk) by means of a peristaltic pump [14]. The reaction was conducted at 40°C. The solution was aged for five days, assuring complete decantation, then, the solution was centrifugated to separate the aqueous solution from product powder. The obtained powder was washed with ethanol-water solution for three times and finally test tubes were placed in the oven at 60°C for two days for drying.

2.1.2. Preparation of TiHCF powder

Titanium hexacyanoferrate powder was synthetized by co-precipitation method. The solution of tetrabutyltitanate was added to the sodium ferrocyanide solution.

- 0.1 M $Na_4Fe(CN)_6$ solution (Sigma Aldrich): 4.8427 ± 0.0001 g of sodium iron cyanide and 11.5 ± 0.1 mL of hydrochloric acid 37% were added to 100 mL of water.
- 0.1 M TBT solution (Sigma Aldrich): 1.71 ± 0.01 mL of tetrabutyltitanate were added to 50 mL with ethanol.

$Na_4Fe(CN)_6$ solution was transferred into two-necked flask and it was covered with a paper of aluminum. TBT solution was added dropwise to $Na_4Fe(CN)_6$ solution and then, the reaction was conducted under N_2 atmosphere at 40°C for 6 hours. Flask was covered because the product is sensitive to light and the reaction needed N_2 atmosphere because titanium reacts easily with oxygen. TiHCF solution was aged for five days thus reaction proceeded, afterwards it was transferred into test tubes, and they were centrifugated to separate aqueous solution from product powder. The obtained powder was washed with ethanol-water solution for three times and finally test tubes were placed in the oven at 60°C for two days for drying.

2.1.3. Preparation of the pellets

For preparation of the pellets, two active materials were used: MnHCF and TiHCF. Pellets were prepared with:

- 70 % of active material (AM) – MnHCF and TiHCF powders.
- 25 % of carbon black (conductive material).
- 5 % of PTFE (binder).

First, the active material was crushed to become homogeneous fine powder and carbon black was added. After, PTFE was mixed and manually pressed with carbon-active material powder to obtain the pellets. Thirteen pellets were prepared for MnHCF and nine pellets were prepared for TiHCF series.

2.2. Electrical characterization and treatment

2.2.1. Preparation of the electrical setup

Three-electrode cell and symmetric coin cell setup were chosen to perform cyclic voltammetry on the TiHCF pellets because they were already used in previous work. For the symmetric coin cell setup, TiHCF pellets were used as a cathode and as an anode because titanium hexacyanoferrate shown two distinct, reversible redox systems. Coin cell setup was chosen for the MnHCF series with zinc as an anode because it was already used in previous works. [26] Cyclic voltammetry was performed by means of CH Instruments Model 660.

The pellet of TiHCF was soaked into sodium nitrate solution (0.1 M) under vacuum for two hours. For the three-electrode cell (see Figure 7), the pellets were fixed inside the aluminium mesh with a clip, and it was inserted in the cell:

- working electrode (WE) is the TiHCF pellet inside the aluminium mesh.
- counter electrode (CE) is platinum electrode.
- reference electrode (RE) is saturated calomel electrode (SCE).

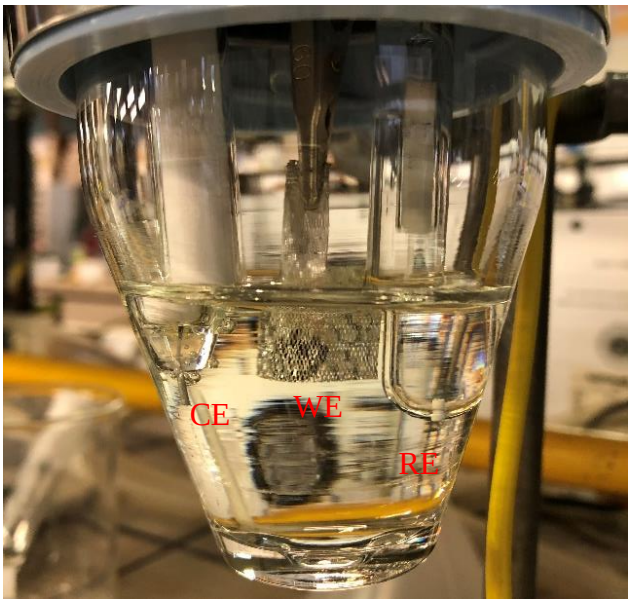

Figure 7: three-electrode cell with $NaNO_3$ as electrolyte used for TiHCF series

For the symmetric coin cell (shown in Figure 8), the pellets were inserted inside the cell: TiHCF pellets were used as cathode and as anode.

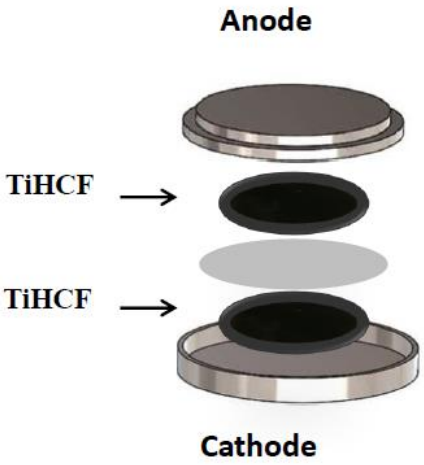

Figure 8: symmetric coin cell used for TiHCF series

The manganese hexacyanoferrate pellet was soaked into zinc sulphate solution (3 M) under vacuum for two hours. Then, the pellet was inserted inside the coin cell (compare in Figure 9) where:

- zinc is the anode.
- MnHCF is the cathode.

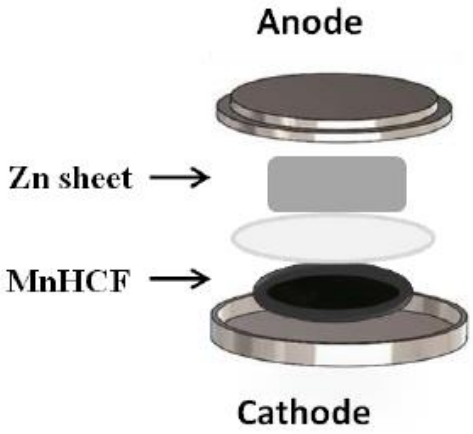

Figure 9: coin cell used for MnHCF series

2.2.2. Cyclic Voltammetry (CV): treatment and characterization

Hereafter the cyclic voltammetry parameters are reported in Table 1.

	MnHCF – coin cell	**TiHCF – three-electrode cell**	**TiHCF – symmetric coin cell**
Initial potential	1.3 V (vs Zn^0/Zn^{2+})	0 V (vs SCE)	0 V
High potential	2 V (vs Zn^0/Zn^{2+})	1.4 V (vs SCE)	1.4 V
Low potential	1 V (vs Zn^0/Zn^{2+})	-1 V (vs SCE)	-1 V
Initial scan polarity	Positive	Positive	Positive
Scan rate	0.0002 V/s	0.0001 V/s	0.0001 V/s
Sweep segments	n	n	n
Sample interval	0.001 V	0.001 V	0.001 V
Quiet time	2 s	2 s	2 s
Sensitivity	$2 \cdot 10^{-2}$ A/V	$2 \cdot 10^{-2}$ A/V	$2 \cdot 10^{-2}$ A/V

Table 1: parameters of Cyclic Voltammetry

The pellets of the two series were treated with different number of cycles using CV. The metals inside the structure should have different oxidation states depending on the number of cycles performed.

Three types of samples were prepared:

- The pristine (P) pellet was not treated with cyclic voltammetry.
- The "charged" (hereafter called C) pellets were treated with one or more cycles of charge and the metals should be oxidized (Fe^{III}, Mn^{III}, Ti^{IV}).

  The sample C1 was treated with one segment of charge: it means that the electrode potential is ramped linearly versus time starting from an initial potential (E_i) until the final potential (E_f). The sample C2 was treated with three segments (one of charge, one of discharge and another one of charge) and the sample C10 was treated with nineteen segments.

- The "discharged" (hereafter called D) pellets were treated with one or more cycles of discharge and the metals should be reduced (Fe^{II}, Mn^{II}, Ti^{III}).

  The sample D1 was treated with one cycle composed by one segment of charge and one segment of discharge: it means that the electrode potential is ramped linearly versus time starting from an initial potential (E_i) until the final potential (E_f) then, the potential scan is performed in the opposite direction back to E_i. The sample D2 was treated with two cycles (or four segments) and the sample D10 was treated with ten cycles (or twenty segments).

For the symmetric coin cell – TiHCF series, pellets were used as an anode and as a cathode:

- The "charged 1 – anode" (hereafter called C1 – A) and "discharged 1 – anode" (hereafter called D1 – A) samples were treated with one segment and one cycle of CV respectively and metals should be reduced (Fe^{II}, Ti^{III}).
- The "charged 1 – cathode" (hereafter called C1 – C) and "discharged 1 – cathode" (hereafter called D1 – C) samples were treated with one segment and one cycle of CV respectively and metals should be oxidized (Fe^{III}, Ti^{IV}).

2.2.2.1. Manganese hexacyanoferrate

Hereafter, the weights of the different pellets treated with cyclic voltammetry are reported in Table 2:

MnHCF	1st batch	2nd batch
P	3.8 ± 0.1 mg	-
C1	4.0 ± 0.1 mg	-
D1	3.2 ± 0.1 mg	-
C2	4.3 ± 0.1 mg	4.2 ± 0.1 mg
D2	4.1 ± 0.1 mg	4.1 ± 0.1 mg
C5	-	3.6 ± 0.1 mg
D5	-	4.2 ± 0.1 mg
C10	2.6 ± 0.1 mg	5.1 ± 0.1 mg
D10	4.8 ± 0.1 mg	5.6 ± 0.1 mg

Table 2: overview of different samples of cycled MnHCF with respective mass of total formulation

2.2.2.2. Titanium hexacyanoferrate

The weight of the pellets treated with cyclic voltammetry are reported hereafter in Tables 3 and 4:

TiHCF	P	C1	D1	D2	D10
Three-electrode cell	3.6 ± 0.1 mg	3.1 ± 0.1 mg	1.4 ± 0.1 mg	3.8 ± 0.1 mg	4.1± 0.1 mg

Table 3: overview of different samples of TiHCF series with respective mass of total formulation – three-electrode cell

TiHCF	P	C1 - A	C1 - C	D1 - A	D1 - C
Symmetric coin cell	3.6 ± 0.1 mg	3.4 ± 0.1 mg	3.4 ± 0.1 mg	3.9 ± 0.1 mg	3.9 ± 0.1 mg

Table 4: overview of different samples of TiHCF series with respective mass of total formulation - symmetric coin cell

2.3. X - Ray Photoelectron Spectroscopy (XPS)

The XPS measurements were performed in a VG Escalab 220i-XL spectrometer with a model 220 analyzer and six channeltrons. The x-ray tube has a twin anode source with Mg and Al and the non-monochromate Al Kα radiation was selected. The pressure of the analysis chamber was around 10^{-8} mbar during the measurements. Hereafter, the measurement parameters for all the surveys and detailed spectra are reported in Tables 5 and 6. For all measurements the lens mode LAE was used, since the samples with a diameter of around 8 mm were big enough to use this mode providing good resolution and intensity.

Acquisition parameters	Survey spectra	Detailed spectra
Range (eV)	-5 – 1200 eV	-
Pass energy (eV)	50 eV	50 eV
Number of scans	1	4 – 6
Dwell time (ms)	100 ms	300 ms
Step size	0.5	0.1

Table 5: acquisition parameters for survey and detailed spectra for the different samples of the MnHCF and TiHCF series

MnHCF	Range (eV)	TiHCF	Range (eV)
Mn 3p, Fe 3p and Na 2s	35 - 80 eV	**Ti 3p, Fe 3p and Al 2p**	20 - 135 eV
C 1s	270 - 310 eV	**C 1s**	270 - 310 eV
N 1s	385 - 415 eV	**N 1s**	385 - 415 eV
O 1s	520 - 550 eV	**O 1s**	520 - 550 eV
Mn 2p, F 1s and Fe 2p	630 - 745 eV	**F 1s and Fe 2p**	675 - 750 eV
Na 1s and Zn 2p	1005 - 1090 eV	**Zn 2p and Na 1s**	1005 - 1090 eV
		Ti 2p	445 - 480 eV

Table 6: measured energy range for detailed spectra for different elements of the MnHCF and TiHCF series

Charge correction was performed to the N 1s signal of cyanide to 397.6 eV. [26] For cross-checking of the charge correction, the signal of conductive carbon was observed to be in the range of 284.5 eV ± 0.3 eV. Peak fitting was performed with the software Unifit 2021 using Voigt profiles (convolution of Gaussian and Lorentzian functions). XPS quantification in Unifit 2021 was realized by measuring intensities and normalizing them with sensitivity factors. These sensitivity factors are calculated in the program as a product of the transmission function, photoelectric cross-section, and inelastic mean free path (for homogeneous samples).

3. RESULTS AND DISCUSSION

In this chapter, the results of the cyclic voltammetry and the XPS measurements are discussed. Emphasis is put on systematic changes between different cycled samples and correlation of cyclic voltammetry and the XPS results.

3.1. Cyclic Voltammetry (CV)

For MnHCF coin cell with Zn as a cathode (≈ -0.76 V vs SHE – saturated hydrogen electrode), papers suggested to use a potential range between 1.0 – 2.0 V. [26] For TiHCF three-electrode cell, in previous work CVs were performed between -1.3 – 1.3 V vs SCE (≈ 0.24 V vs SHE) in aqueous electrolyte at different scan rate. [27] For all setups, a wide range was tested at a high scan rate with cyclic voltammetry and then the potential was chosen according to the position of the peaks. In this work, the chosen range was between 1.0 – 2.0 V for MnHCF series and -1.0 – 1.4 V for TiHCF series. For the TiHCF in symmetric coin cell setup, electrodes are made with the same material, therefore the peaks are in a different position than TiHCF three-electrode cell where the reference was SCE.

Herein, the results of cyclic voltammetry of MnHCF in the coin cell setup and TiHCF in the three-electrode cell and symmetric coin cell setups are described.

3.1.1. Manganese hexacyanoferrate – coin cell

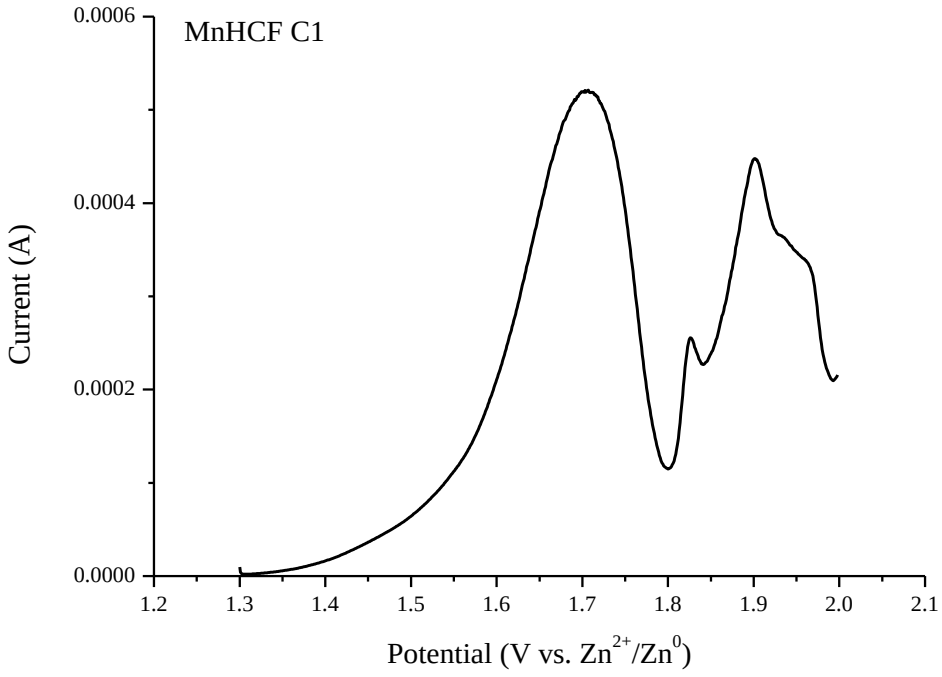

Figure 10: CV scan which leads to the sample C1 of MnHCF series

In the cyclic voltammetry scan of the sample “charged 1” of the MnHCF series (Figure 10) there are four peaks: as seen above in Chapter 1.4, during the charge segment there is the oxidation of the species. The main peak at 1.72 V could be assigned to the oxidation of iron and the other peaks around 1.85 V, 1.92 V and 1.98 V are probably due to the oxidation of manganese [28] with concomitant Na-ion removal from the MnHCF structure.

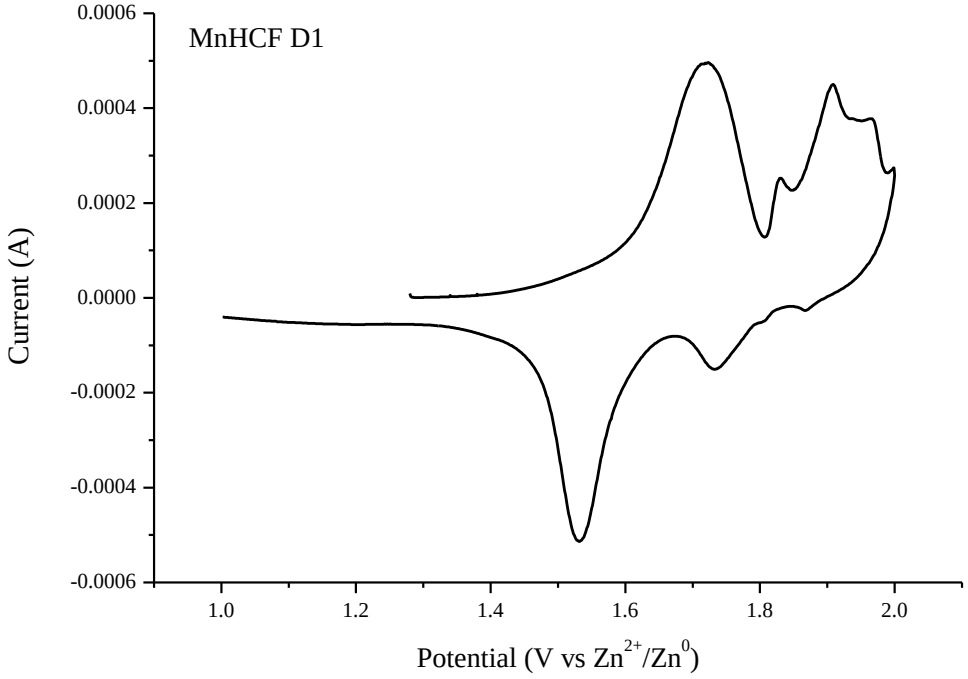

Figure 11: CV scan which leads to the sample D1 of MnHCF series

In the cyclic voltammetry scan of the sample “discharged 1” of the MnHCF series (Figure 11) there are both charge and discharge segments. As seen above in Chapter 1.4, in the discharge part there is the reduction of the species, and four peaks are observed. The main peak at 1.55 V could be assigned to the reduction of the iron and the other peaks around 1.75 V, 1.82 V and 1.90 V are probably due to the reduction of manganese [28] with concomitant Zn-ion intercalation into the MnHCF structure during the discharge segment.

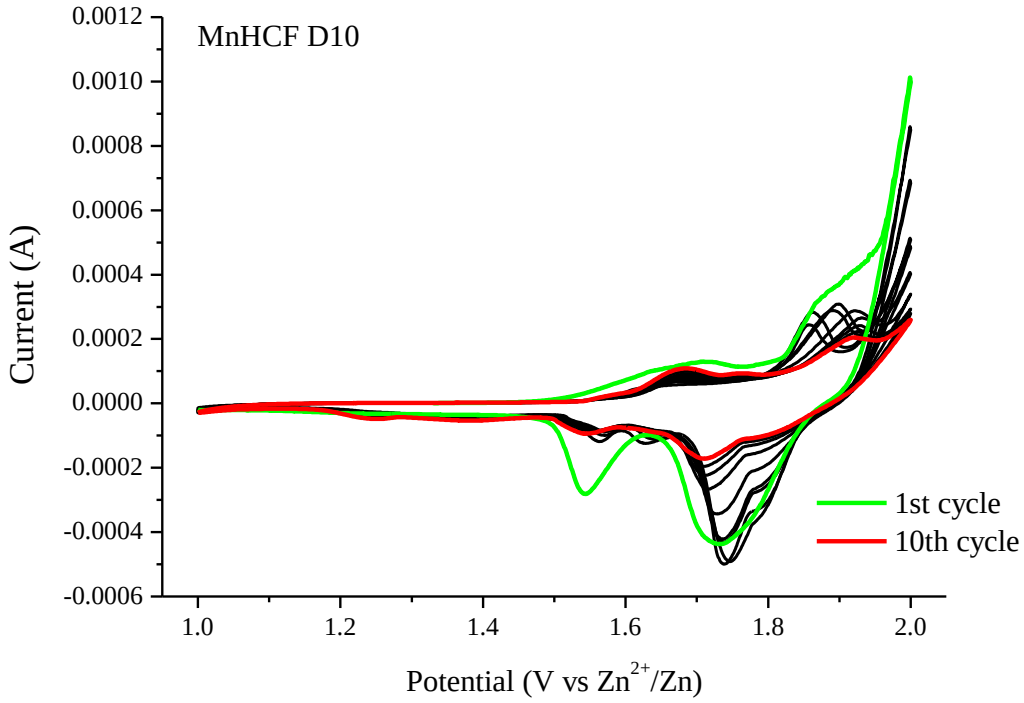

Figure 12: CV scan which leads to the sample D10 of the MnHCF series

Cyclic voltammetry scan of the D10 sample of the MnHCF is reported in Figure 12 and the scan changes during cycling. This is most likely due to the modification of the structure which is due to the substitution of manganese by the Zn ions during cycling. [26,28]

3.1.2. Titanium hexacyanoferrate – three-electrode cell

Hereafter, an exemplary cyclic voltammetry scan for the TiHCF pellets is reported. This pellet was pressed inside the aluminium mesh to have good surface contact, and CV was performed. It was not possible to recover it for the subsequently measurements, so XPS analyses were performed on the pellets treated with CVs and fixed inside the aluminium mesh with a clip. This CV scan is useful to identify the positions of the oxidation and reduction peaks.

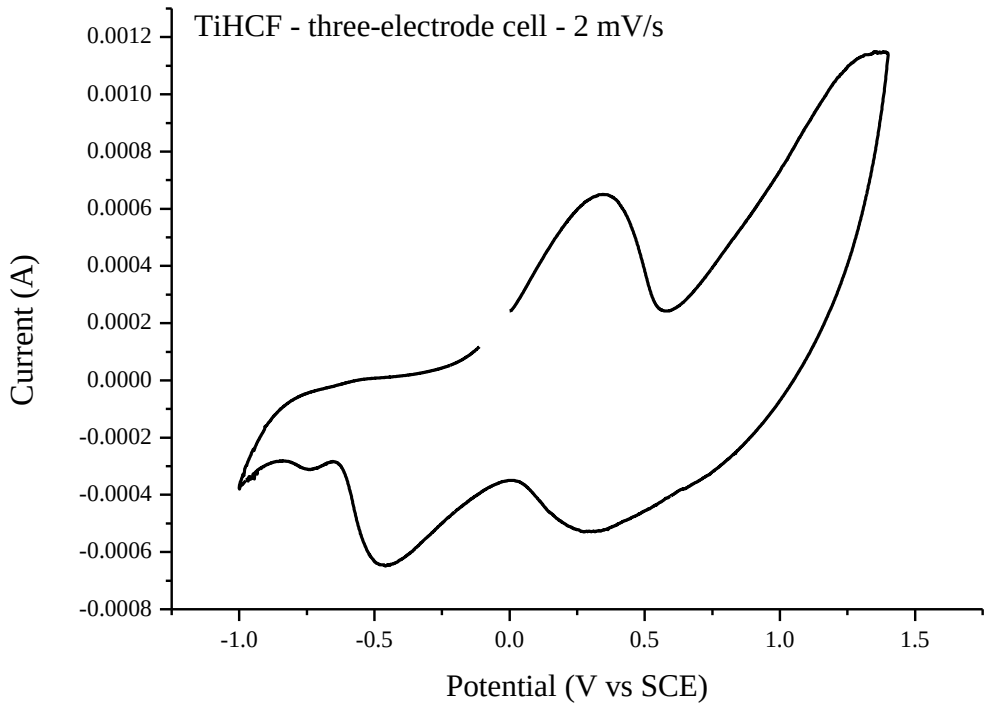

Figure 13: exemplary cyclic voltammetry (scan rate = 2 mV) of the pristine pellet pressed inside the aluminium mesh for TiHCF series – three-electrode cell and treated with one cycle of CV

In Figure 13, cyclic voltammetry of pristine pellet for the TiHCF series is reported: two peaks are observed in both charge and discharge segments. The peaks around 0.48 V in charge segment and 0.42 V in discharge part could be assigned to the $Ti^{3+/4+}$ redox couple, instead the other small hump around 1.1 V in the charge part is due to the oxidation of iron. [27] The peak of the oxidation of the iron is not observed in the CV and it should be around 0.7 V in the discharge segment. [27] The other peaks around -0.50 V and -0.75 V in discharge part were not assigned.

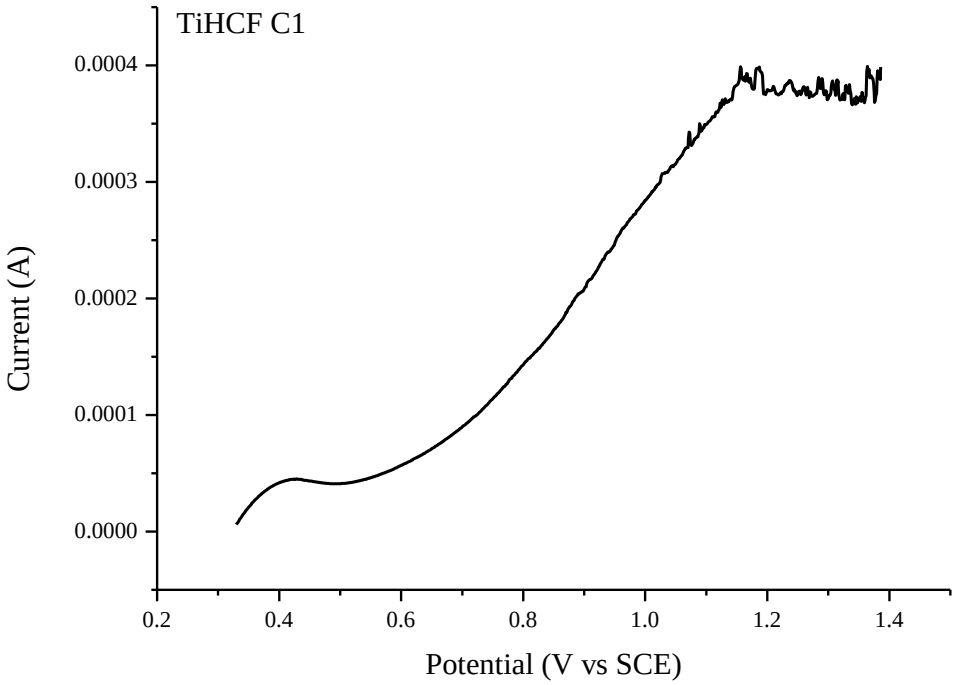

Figure 14: CV scan which leads to the sample C1 fixed inside the aluminium mesh with a clip for TiHCF series – three-electrode cell

Figure 14 shows the CV scan of the C1 pellet fixed inside the aluminium mesh with a clip with the aim of recovering it after the cyclic voltammetry to perform XPS measurement. Cyclic voltammetry scan does not show the peak around 1.2 V, and this is probably due to the loss of the surface contact.

3.1.3. Titanium hexacyanoferrate – symmetric coin cell

As seen above in Chapter 3.1.2, CVs performed with three-electrode cell were not as expected and this is the reason why afterwards cyclic voltammetry was performed with symmetric coin cell for the TiHCF series to have a good surface contact and, consequently, a better CV scan. In this case, TiHCF pellets were used as a cathode and as an anode, and the electrolyte was always $NaNO_3$.

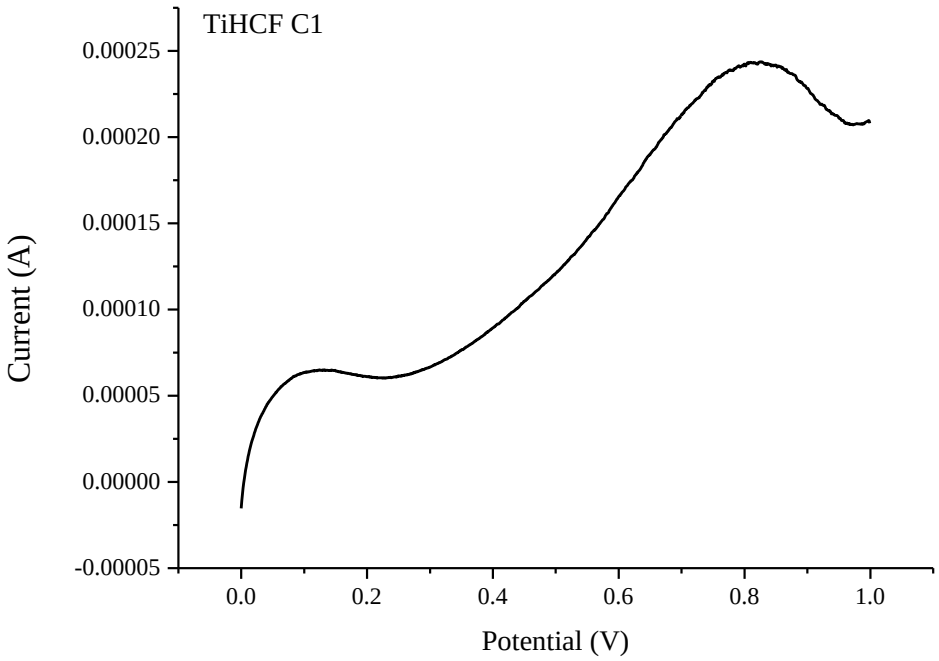

Figure 15: CV scan which leads to the sample C1 of the TiHCF series – symmetric coin cell

In Figure 15, cyclic voltammetry scan for the sample "charged 1" of the TiHCF series is reported. Herein, two peaks are observed: the peak at 0.1 V could be assigned to the oxidation of titanium and the peak around 0.8 eV is due to the oxidation of iron according to CV scans shown in Chapter 3.1.2. The positions of the redox peak are different between the two cells because in three-electrode cell the reference was the SCE and, in symmetric coin cell, cathode is a TiHCF pellet.

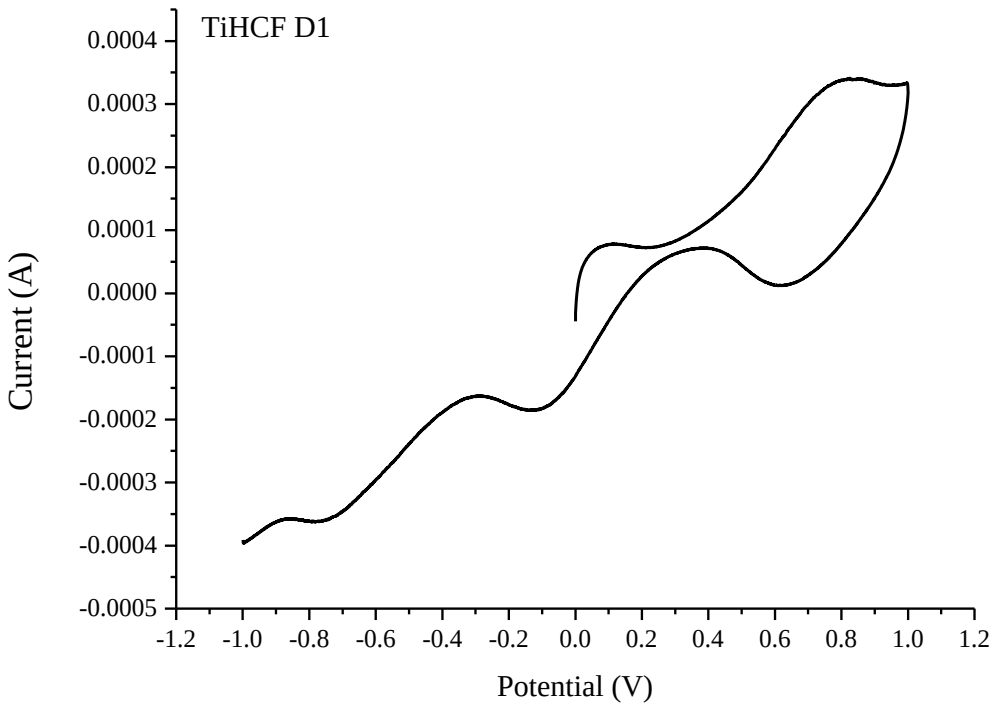

Figure 16: CV scan which leads to the sample D1 of the TiHCF series – symmetric coin cell

In the cyclic voltammetry for the sample "discharged 1" of the TiHCF series (Figure 16) there are the charge and the discharge segments. In the discharge part, two peaks are observed: the peak at -0.05 V was assigned to the reduction of titanium and the peak around 0.65 eV is due to the reduction of iron according to CV scans shown in Chapter 3.1.2. The peak around -0.75 V in the discharge segment was not assigned.

3.2. X-Ray Photoelectron Spectroscopy

The following Chapters 3.2.1, 3.2.2, 3.2.3 encompass the XPS investigation of the MnHCF and TiHCF in different electrical setups. The focus is on chemical changes in the hexacyanoferrates structure and oxidation states of the transition metals during electrical cycling.

In the MnHCF series, a redox chemistry in line with cyclic voltammetry as well as significant chemical changes can be recorded. In contrast, the TiHCF series only reveals less chemical changes and no measurable change in oxidation states. This is further explained in the upcoming chapters.

In the case of Mn 2p, Mn 3p, Fe 2p, Fe 3p and Zn 2p the information about binding energies refer to $2p_{3/2}$ energy, if not otherwise stated.

3.2.1. Manganese hexacyanoferrate - coin cell

First, representative survey spectra of the MnHCF series are shown. Then, the applied fits and comparative detailed spectra are used to describe alterations during electrochemical cycling. Complete XPS quantification of the samples of the MnHCF series as well as TiHCF series could be found in the Appendix.

3.2.1.1. Survey spectra of the MnHCF powder and exemplary formulated samples

Hereafter, the survey spectra of different samples for the MnHCF series are reported and every spectrum shows photoelectron and Auger lines for the different expected elements.

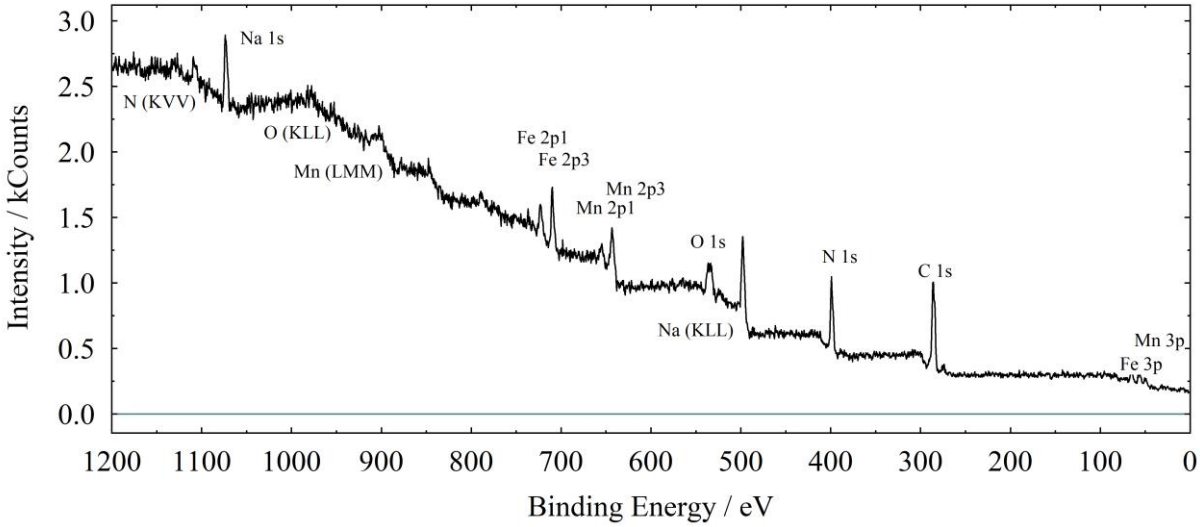

Figure 17: survey spectrum of the MnHCF powder used for formulation of the samples in the MnHCF series

In Figure 17, the survey spectrum of the powder of the MnHCF series are shown. Peaks of different elements are observed: as expected, there are the main signal of manganese (641 eV – 2p doublet), iron (708 eV – 2p doublet), nitrogen (397.6 eV – 1s singlet) and carbon (around 285 eV – 1s singlet) that compose the structure of the manganese hexacyanoferrate. [22]

Moreover, there is the peak of sodium (1071 eV – 1s singlet) which derives from the synthesis, and it is most likely inside the large cavities in the structure. Also, the oxygen peaks (around 530 – 532 eV – 1s singlet) are due to the presence of water in the cavities because of the aqueous solution.

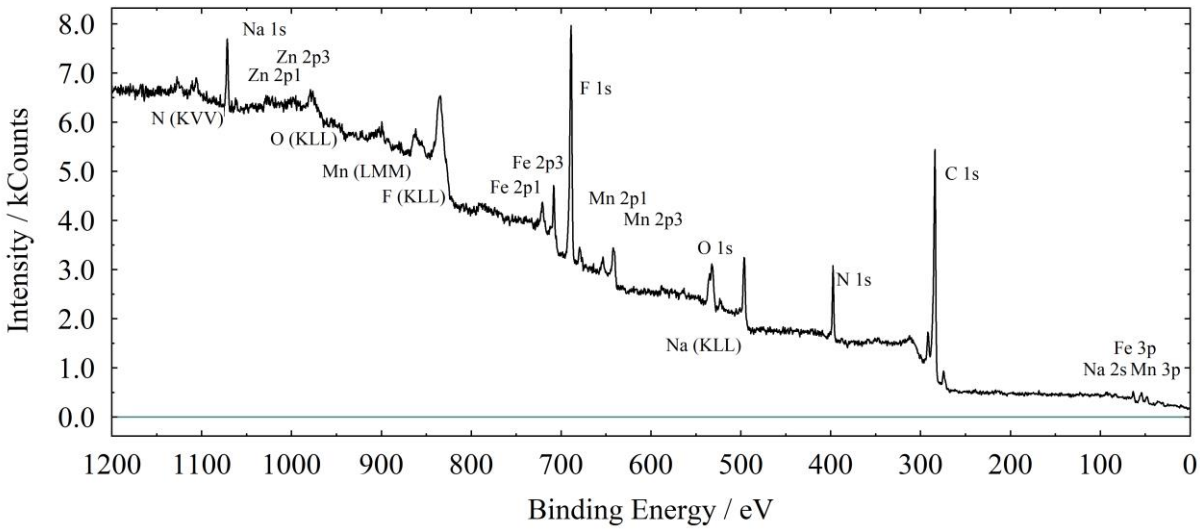

Figure 18: survey spectrum of the pristine pellet of MnHCF series

In the survey spectrum of the pristine pellet of the MnHCF series (Figure 18), a peak due to the fluorine is observed around 690 eV (F 1s – singlet). [22] This intense peak is due to the polytetrafluoroethylene (PTFE) used for the preparation of the pellets. Furthermore, unexpected Zn 2p signals are observed at 1021 eV and 1044 eV: these peaks are probably due to a contamination of the sample during the preparation of the pellets.

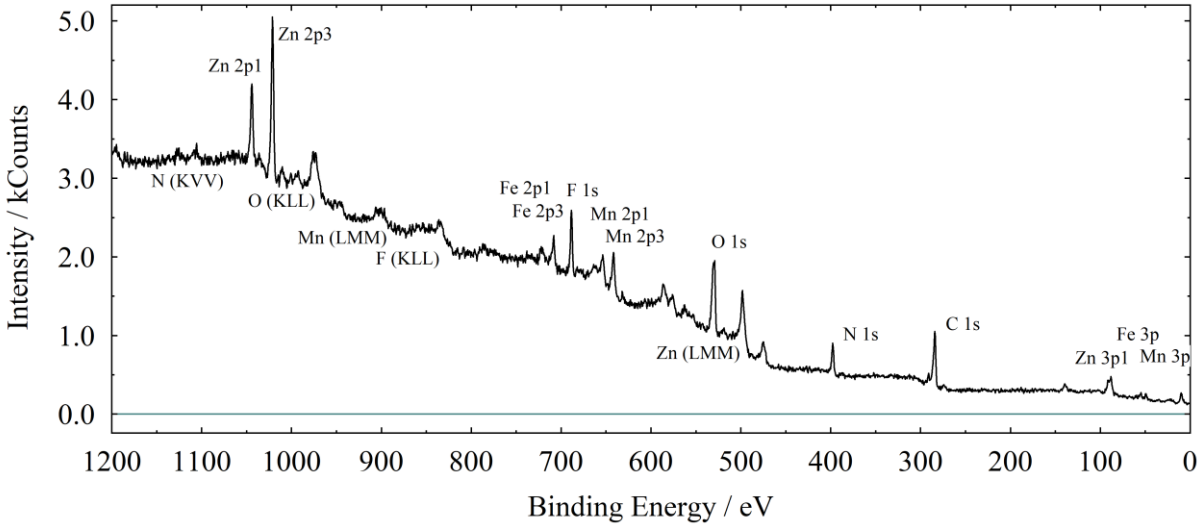

Figure 19: survey spectrum of the C10 pellet of MnHCF series

In the survey spectrum of the "charged 10" pellet of the MnHCF series in Figure 19, there are again two peaks due to the zinc: the $2p_{3/2}$ is at 1021 eV and $2p_{1/2}$ is around 1044 eV but with a larger intensity than the pristine pellet. [22] The presence of zinc can be related to the transformation of the MnHCF cathode during cycling as independent XAFS measurements

suggest a progressively manganese substitution with Zn in the cathode material. [14] The peaks of zinc are observed for all the pellets of the MnHCF treated with cyclic voltammetry and it derives from the aqueous electrolyte.

3.2.1.2. Quantification of the MnHCF powder

Hereafter, the atomic percentages of the different elements for the pristine powder used for formulation of the MnHCF series are reported in Table 7 and the ratios between N 1s of the cyanide and the metals of the pristine powder are shown in Table 8. The quantification was calculated with the fit obtained from the detailed spectra and, for the pristine powder, the Fe 2p peaks were used for the quantification because there are not the loss structure of F 1s under the Fe 2p signals.

	N	**Na**	**C**	**O**	**Mn**	**Fe**
Pristine powder	22.5	5.1	56.2	8.9	3.9	3.4

Table 7: atomic percentages of the different elements for pristine powder of the MnHCF series

	$[N_{(CN)}]/[Fe_{2p}]$	**$[N_{(CN)}]/[Mn_{2p}]$**	**$[Fe_{2p}]/[Mn_{2p}]$**
Pristine powder	6.5	5.8	0.9
Theoretical ratios	6.0	6.0	1.0
Ratios from previous work [14]	6.0	5.5	0.9

Table 8: ratios between nitrogen of the cyanide (397.6 eV) and the metals of the powder used for the formulation of the pellets of the MnHCF series

The XPS quantification of the powder and the ratios between the nitrogen of the cyanide and the metals suggest successful synthesis of the MnHCF powder. The higher content of Na is due to the synthesis procedure and will be removed during cycling, as shown later. The oxygen derives from water in the cavities and a quantification of carbon relative to the metals is difficult since adventitious hydrocarbons overlap with C 1s cyanide signal.

3.2.1.3. XPS fitting of the detailed spectra in MnHCF series

A set of fitting parameters for all detailed scans Mn 3p, Fe 3p, C 1s, N 1s, O 1s, Mn 2p and Fe 2p were extracted from the MnHCF powder sample and used for the fitting of the series of cycled MnHCF samples. The width of the Gaussian and Lorentzian functions in the convolutions were set constant resulting in FWHM/eV of 2.6 for Mn 3p doublet, 2.6 for Fe 3p doublet, 1.8 for C 1s singlet, 1.9 for N 1s singlet, 2.3 for O 1s singlet, 3.3 for Mn 2p doublet and 2.3 Fe 2p doublet. Binding energy positions of components in the detailed spectra were allowed to vary a range of ± 0.3 eV.

Hereafter, exemplary fittings are reported using detailed spectra of the formulated pellet of MnHCF without cycling complemented by other examples if needed.

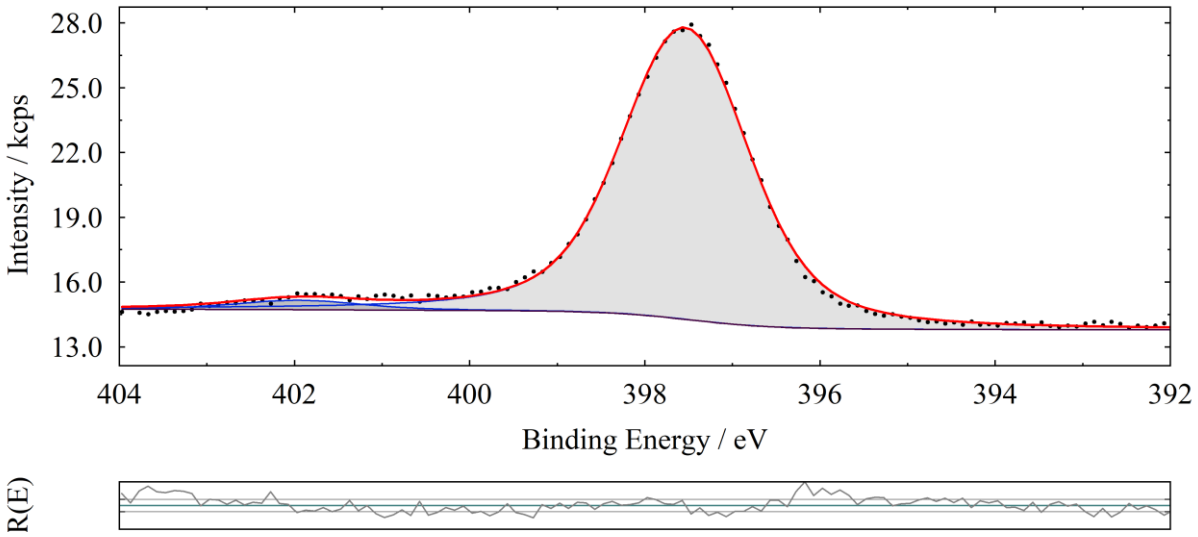

Figure 20: N 1s peaks of the pristine pellet for the MnHCF series

As seen above in Chapter 2.3, charge correction was performed on N 1s signal, and the main peak was fixed at 397.6 eV.

In Figure 20, the fit of the N 1s signals for the pristine pellet of the MnHCF series is reported and two different peaks are observed: the main peak around 397.6 eV was assigned to the nitrogen of the cyanide and the other peak around 402 eV was assigned to the nitrogen coordinated to the oxygen of the water that is inside the large cavities of the MnHCF structure. [29,30]

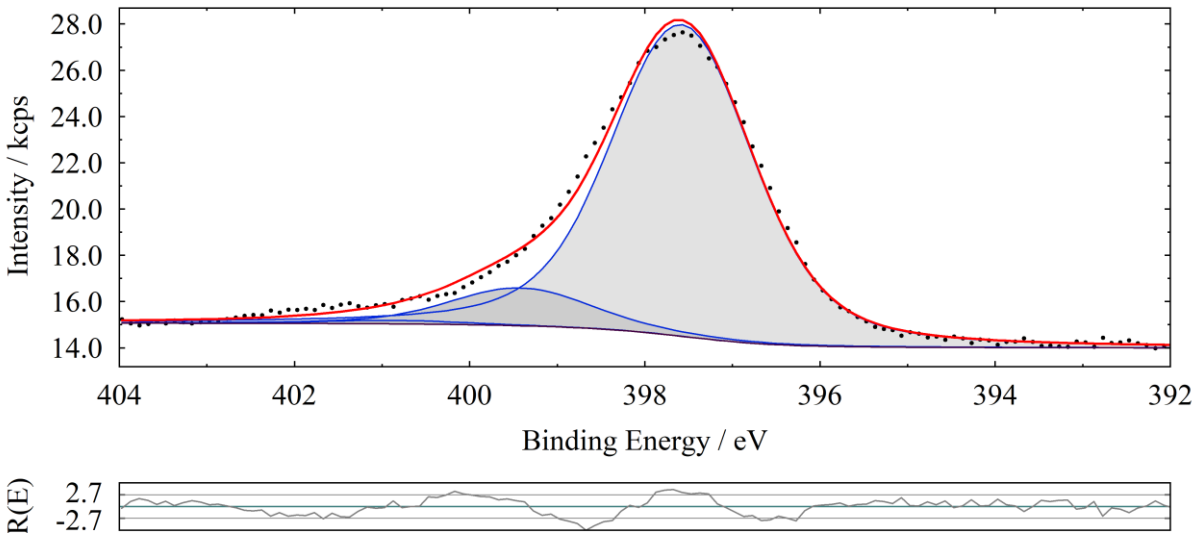

Figure 21: N 1s peaks of the C1 pellet for the MnHCF series

In the fit of N 1s peaks of the C1 pellet and all further cycled samples for the MnHCF series (Figure 21), a new peak is observed around 399.4 eV, and this could be assigned to the nitrogen coordinated to the hydrogen of the water that is inside the large cavities of the structure. [30]

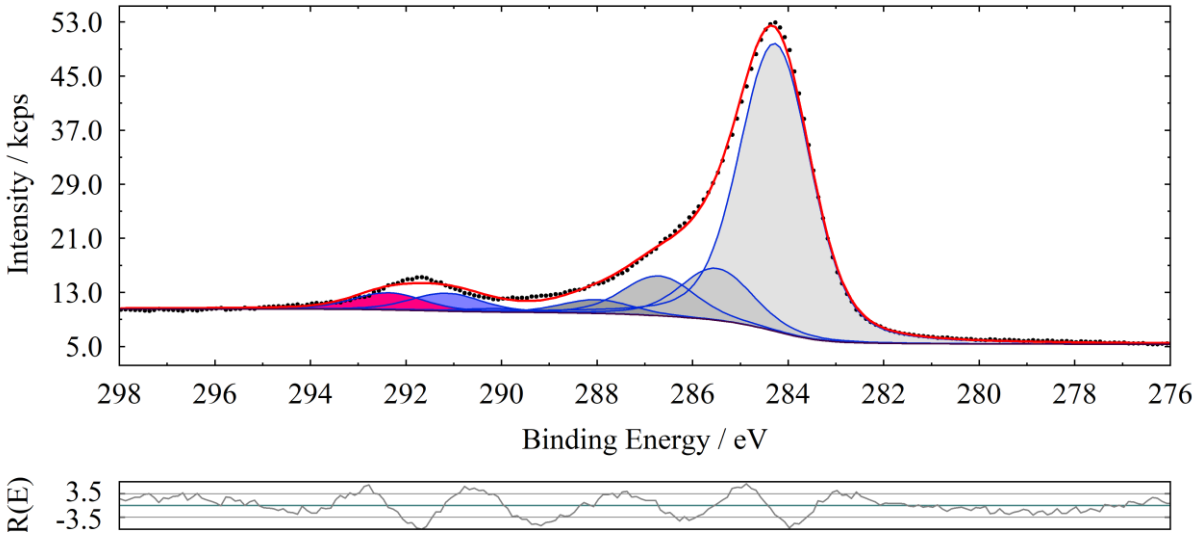

Figure 22: C 1s peaks of the pristine pellet for the MnHCF series

As seen above in Chapter 2.3, for cross-checking of the charge correction, the signal of conductive carbon was observed to be in the range of 284.5 eV ± 0.3 eV.

Figure 22 shows the C 1s peaks for the pristine pellet of the MnHCF series, six peaks are observed: the main signal at 284.3 eV could be assigned to the carbon of the cyanide [31] and the signal of conductive carbon, which cannot be deconvoluted since they are close in binding energy. The other peak at 285.5 eV, 286.7 eV and 288 eV could be assigned to aliphatic

hydrocarbon, carbon-hydroxil bonds and carbonyl or –FCH–CH–F bonds respectively. [32] The peaks around 291.1 eV and 292.4 eV could be assigned to the $–CF_2–$ bonds of the PTFE. [32,33]

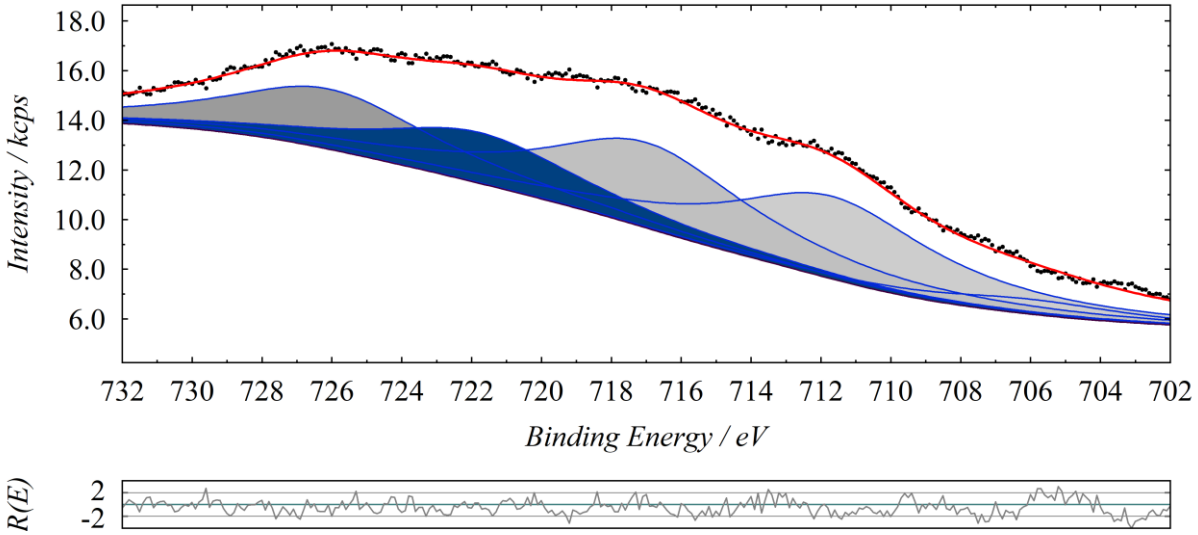

Figure 23: loss structure peaks of F 1s of PTFE

The F 1s spectrum exhibits a significant loss structure around 20-30 eV to higher binding energies, which interferes with the Fe 2p signal. For a better interpretation of the Fe 2p peaks in the same region, the F 1s region of a pure PTFE sample (Figure 23) was analysed with XPS, and the spectrum was fitted with Unifit 2021. The width of the Gaussian and Lorentzian functions in the convolutions were set constant resulting in FWHM/eV of 7.27 for F 1s loss structure. The heights of the loss structure peaks were related to the F 1s height for the PTFE, then the fluorine loss structures were included in the detailed spectra of the Fe 2p for all the samples. Hereafter, Table 9 reports the ratios between the height of the loss structure peaks and the F 1s signal for the pure PTFE sample.

Loss structure position	706.0 eV	711.7 eV	717.0 eV	721.8 eV	726.1 eV
$\frac{\textbf{height loss structure}}{\textbf{height F 1s signal}}$	$5.3 \cdot 10^{-3}$	$2.8 \cdot 10^{-2}$	$3.0 \cdot 10^{-2}$	$1.8 \cdot 10^{-2}$	$2.1 \cdot 10^{-2}$

Table 9: ratios between the height of the loss structure peaks and the F 1s signal for the pure PTFE sample

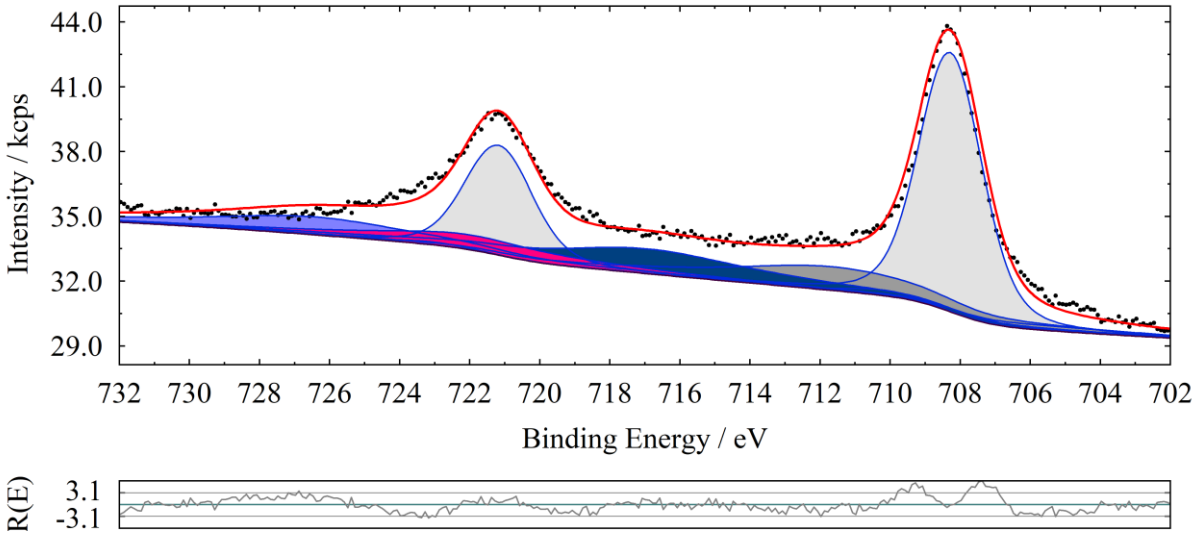

Figure 24: Fe 2p peaks of the pristine pellet for the MnHCF series

In Figure 24, Fe 2p peaks for the pristine pellet of the MnHCF series are shown: the main peak around 708.2 eV was assigned to Fe^{2+} according to literature [34,35] and the other wider peaks are due to the loss structures because of the F 1s signal of PTFE used as a binder.

The Fe $2p_{3/2}$ signal has associated satellite peaks and the satellite peak of Fe $2p_{3/2}$ for Fe^{2+} is located approximately at 714.7 eV. [36] This satellite peak was not included in the detailed spectra of the Fe 2p signals for all the samples. For appropriate fitting of the Fe 2p signals, the spin-orbit coupling energy of 13.2 eV for the Fe 2p had to be adjusted to 12.9 eV and the Lorentzian and Gaussian width of the Fe $2p_{1/2}$ was not hold equal to the respective values of the Fe $2p_{3/2}$. [37]

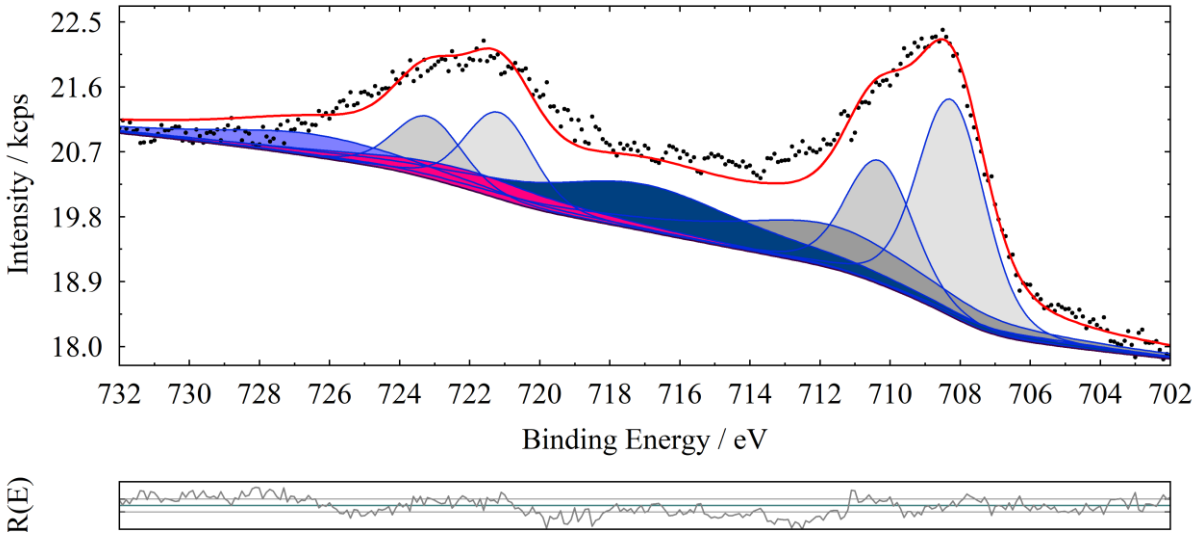

Figure 25: Fe 2p peaks of the C2 pellet for the MnHCF series

In the fit of the Fe 2p peaks for the C2 pellet of the MnHCF series (Figure 25), the main peak around 708.2 eV was assigned to Fe^{2+} as seen before and the second peak at 710.3 eV could be assigned to the Fe^{3+} according to literature [31,35]. The signal around 710.3 eV is more intense for all the charged samples compared to the discharged ones. This will be further demonstrated in the next chapter. The Fe $2p_{3/2}$ signal has associated satellite peaks and these satellite peaks of Fe 2p for Fe^{3+} are located approximately at 718.8 eV for the Fe $2p_{3/2}$ and 729.5 eV for the $2p_{1/2}$ signal respectively. [36] These satellite peaks were not included in the detailed spectra of the Fe 2p signals for all the samples.

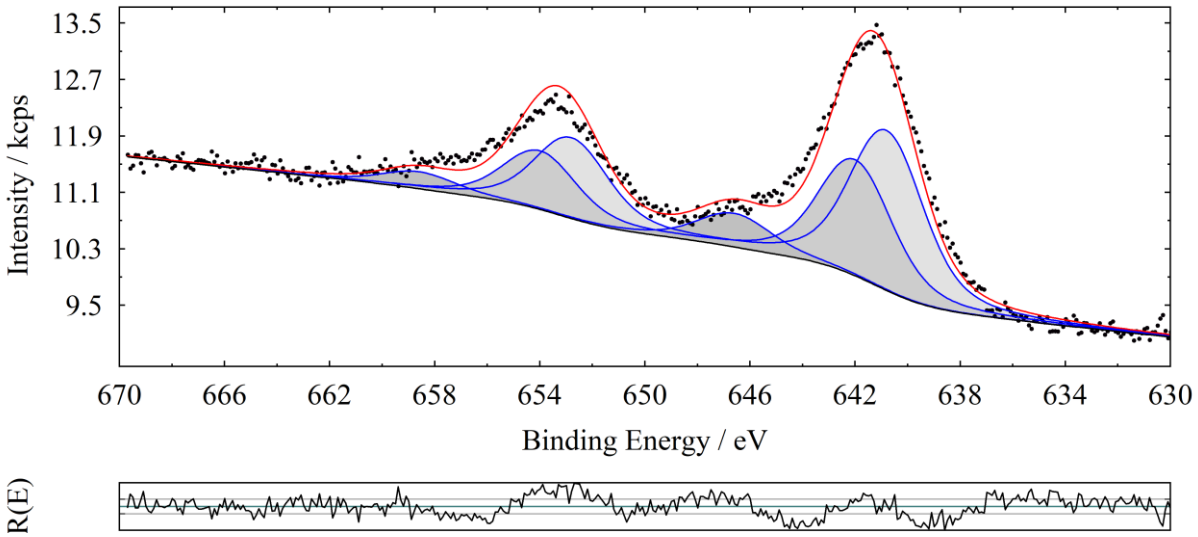

Figure 26: Mn 2p peaks of the powder used for the formulation of MnHCF series

Mn 2p peaks of the pristine powder are shown in Figure 26: the peak around 640.8 eV was attributed to Mn^{2+} according to literature and the signal at 642.0 eV was attributed to Mn^{3+} according to literature [38]. The minor signal at 646.6 eV could be a satellite structure of the high spin manganese coordinated to the nitrogen of the cyanide. [39]

If there is manganese oxide inside the samples, it is probably overlapping with the signals of the Mn at 640.8 eV and 642.0 eV, and it should be around 641.3 eV. [40]

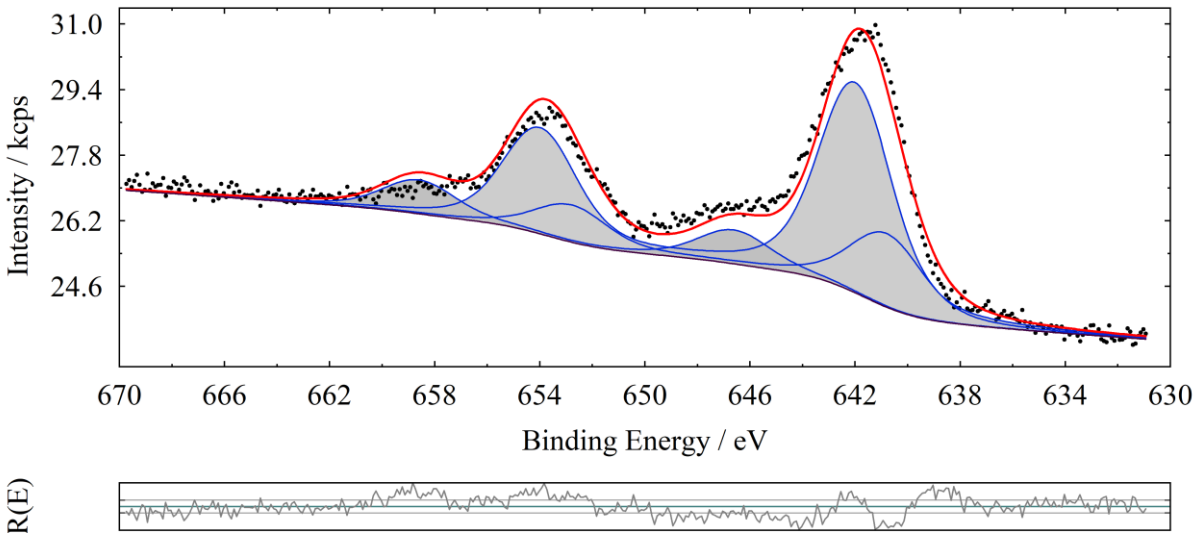

Figure 27: Mn 2p peaks of the pristine pellet for the MnHCF series

In Figure 27, it is observed that Mn^{3+} signal for the pristine pellet of the MnHCF series is higher than Mn^{3+} for the pristine powder: this might indicate that the manganese was partially oxidized during the preparation of this pellet.

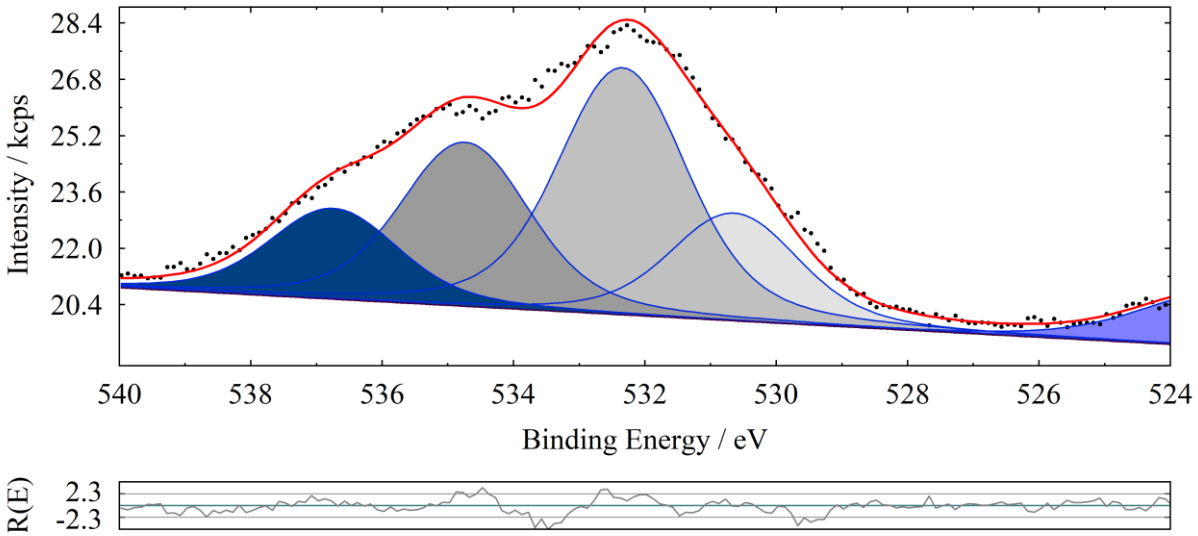

Figure 28: O 1s peaks of the pristine pellet for the MnHCF series

Figure 28 shows the O 1s peaks of the pristine pellet for the MnHCF series and four peaks are observed: the peaks at 530.7 eV and 532.4 eV were assigned to the oxygen coordinated to the nitrogen and to the oxygen of the water that is inside the cavities of the structure. [29]

Moreover, there are other signals at 524.0 eV, 534.8 eV and 536.8 eV, and these peaks were assigned to Na KLL Auger Lines. [22] The KLL Auger lines of sodium were not counted in the quantification of oxygen.

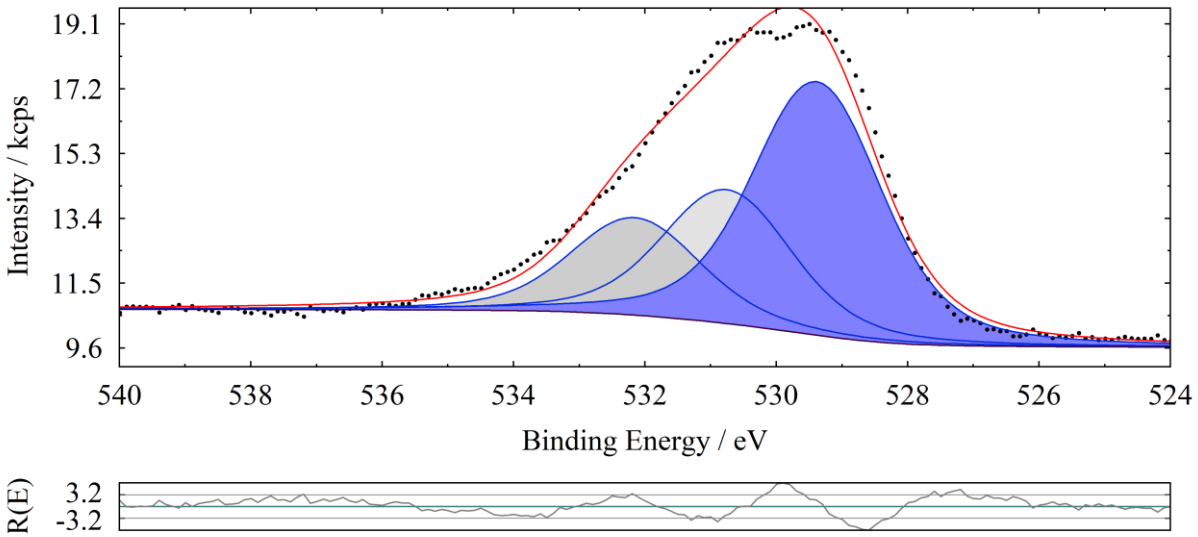

Figure 29: O 1s peaks of the C10 pellet for the MnHCF series

In the fit of the O 1s peaks of the C10 pellet for the MnHCF series (Figure 29), there is a additional signal around 529.3 eV: this low binding energy component in O 1s singlet is found for the charged samples and this peak could be assigned to the oxygen coordinated to the manganese according to literature. [40] Furthermore, for the cycled samples, zinc could go inside the large cavities of the structure or substitute the manganese: in this case the signal at 530.7 eV could be also due to the oxygen coordinated to the zinc [41]. It is probably overlapping with the peak of the oxygen coordinated to the nitrogen and it is not possible to distinguish them. Further discussion can be found in the following chapter. Moreover, the two peaks around 534.8 eV and 536.8 eV are missing because the sodium is removed from the structure during cycling.

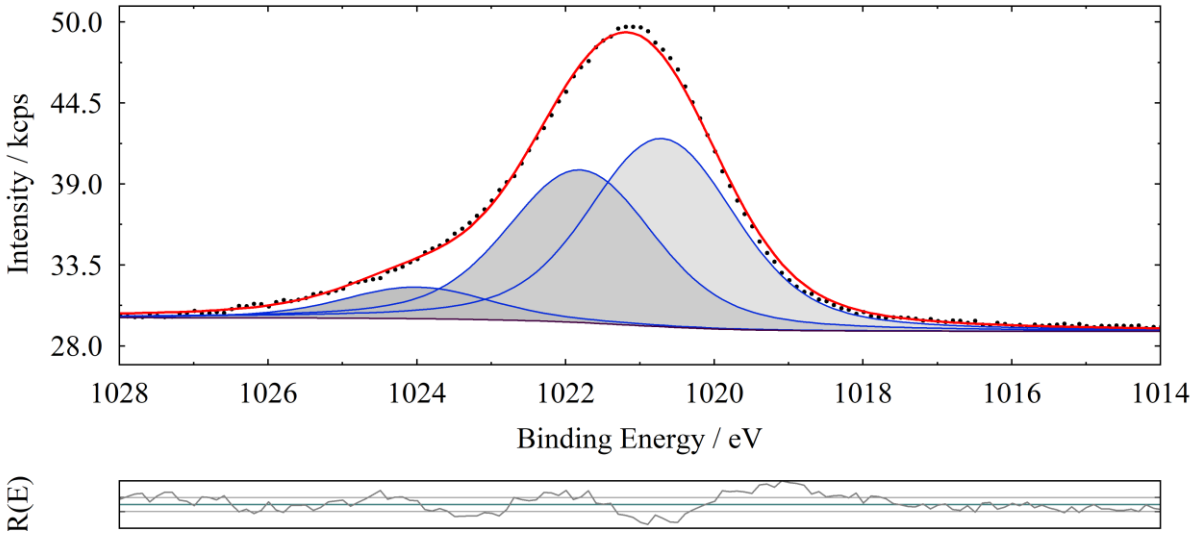

Figure 30: Zn 2p peaks of the C10 pellet for the MnHCF series

The fit of the Zn $2p_{3/2}$ peak for the C10 pellet of the MnHCF series is shown in Figure 30 and three peaks are observed: the first peak around 1020.7 eV was assigned to the zinc that substitute the manganese inside the MnHCF structure [28] and the second peak at 1021.8 eV is probably due to zinc coordinated to the oxygen. [42] The third peak around 1024 eV could be assigned to the zinc coordinated to the oxygen of two hydroxyl groups, since in literature is reported the signal of $Zn(OH)_2$ at 1023.2 eV. [43]

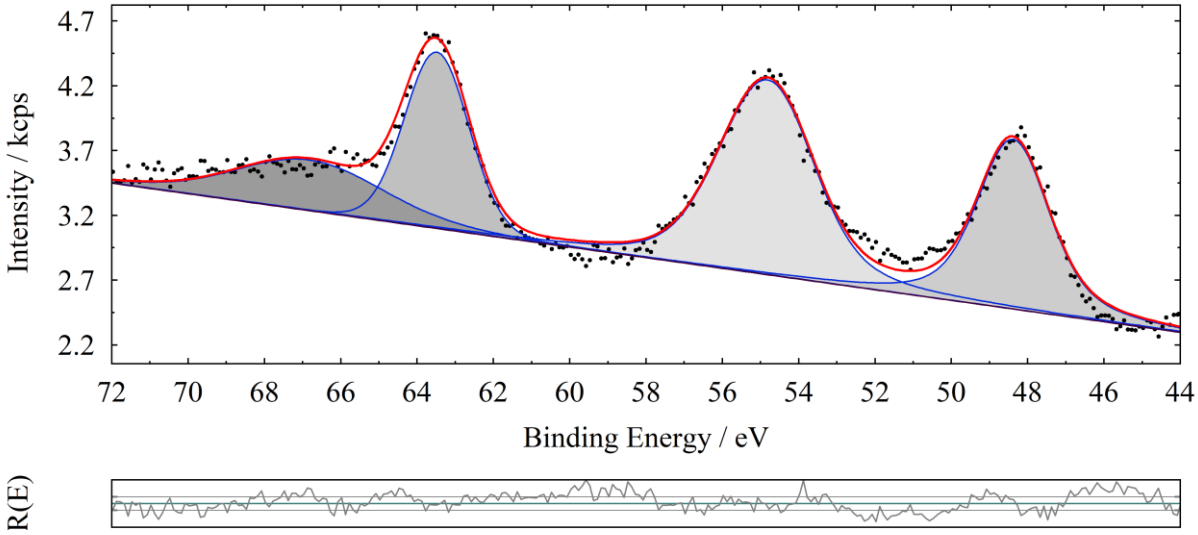

Figure 31: Na 2s, Fe 3p and Mn 3p peaks of the pristine pellet for the MnHCF series

Figure 31 shows different peaks of the pristine pellet for the MnHCF series: the peak at 54.6 eV is Fe 3p signal and it was assigned to Fe^{2+} according to literature [34] and to previous detailed spectrum (Figure 24). The Fe 3p signal was also used for the quantification of the iron inside the sample. The peak around 48.5 eV is Mn 3p signal and it was not assigned to any oxidation state because in literature the same BE value is reported for Mn^{2+} and Mn^{3+}. [40] For uncycled samples, the manganese is situated in the building framework of the hexacyanoferrate structure and through cycling in the aqueous Zn^{2+} solution, some Mn-ions get replaced by the Zn-ions and can migrate in the cavities. In the latter, the Mn-ions can coordinate to water, which is also situated in the cavities. The other peak at 63.5 eV is Na 1s signal.

The overview of the fitting results and quantification can be found in the Appendix.

3.2.1.4. Comparative spectra for cycled samples in the MnHCF series

Subsequently, the comparative spectra are reported for the evaluation of the change of the oxidation states for different samples and other chemical changes after cycling. Since the detailed spectra of the samples were scanned 4 to 6 times, absolute intensities as counts/sec are displayed. As the only data processing a constant background was subtracted, which was equal to the base line on the low-binding energy side.

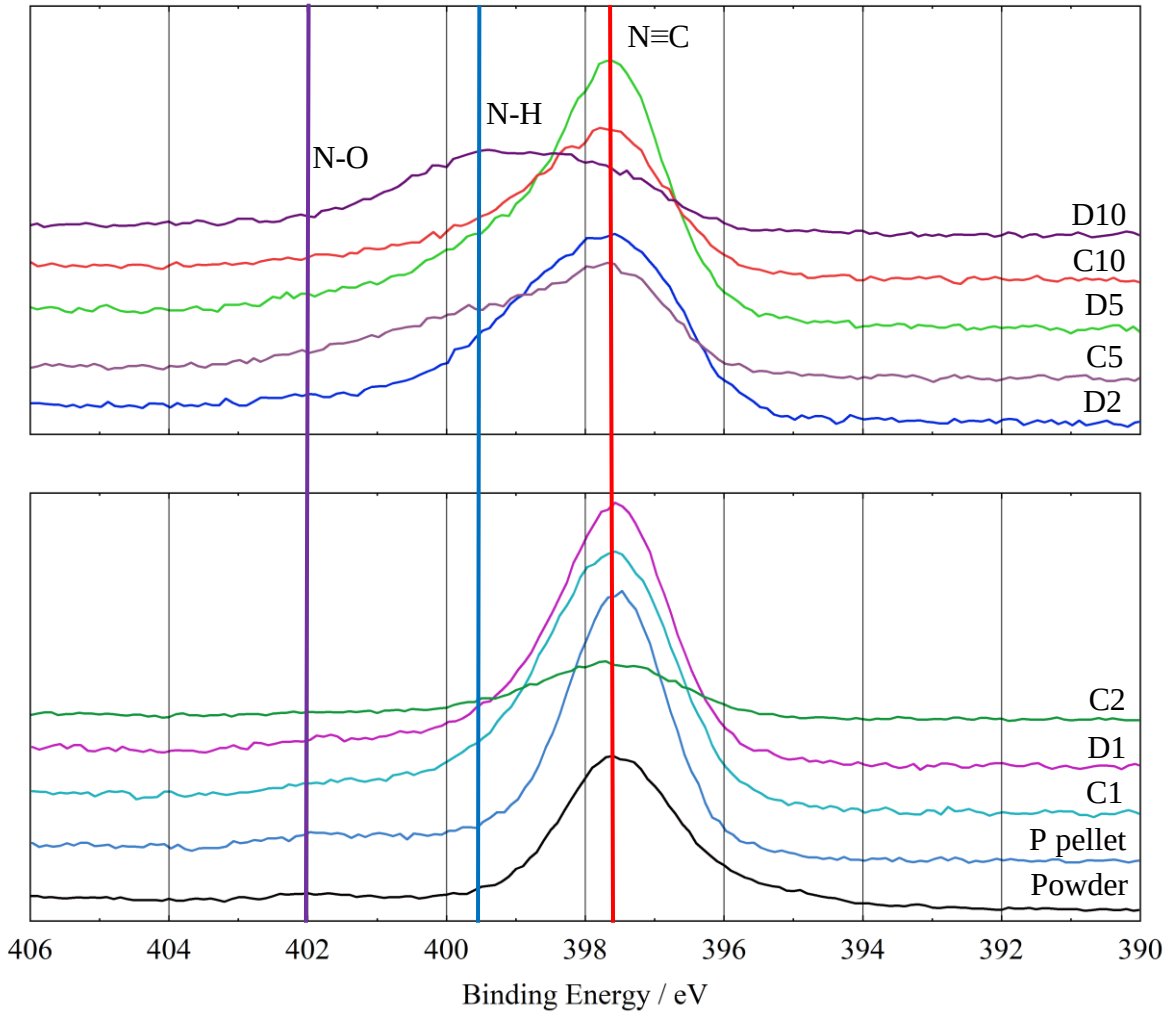

Figure 32: comparative spectra of N 1s peaks of the different samples for the MnHCF series

In Figure 32, the comparative spectra of N 1s peaks of the MnHCF series are shown: a second peak around 399.4 eV increases during cycling and it is intense for the D10 sample. As seen above in Chapter 3.2.1.3, this peak was assigned to the nitrogen coordinated to the hydrogen of the water that goes inside the large cavities of the structure during cycling. Furthermore, the signal at 402.0 eV increases during cycling but not as much as the peak around 399.4 eV. As already described, the signal at 402.0 eV is attributed to nitrogen coordinated to the oxygen and

it could be due to the $NaNO_3$ used as electrolyte. The relative contributions of the N-H and N-O species increase along with the overall oxygen content during cycling (see Figure 34).

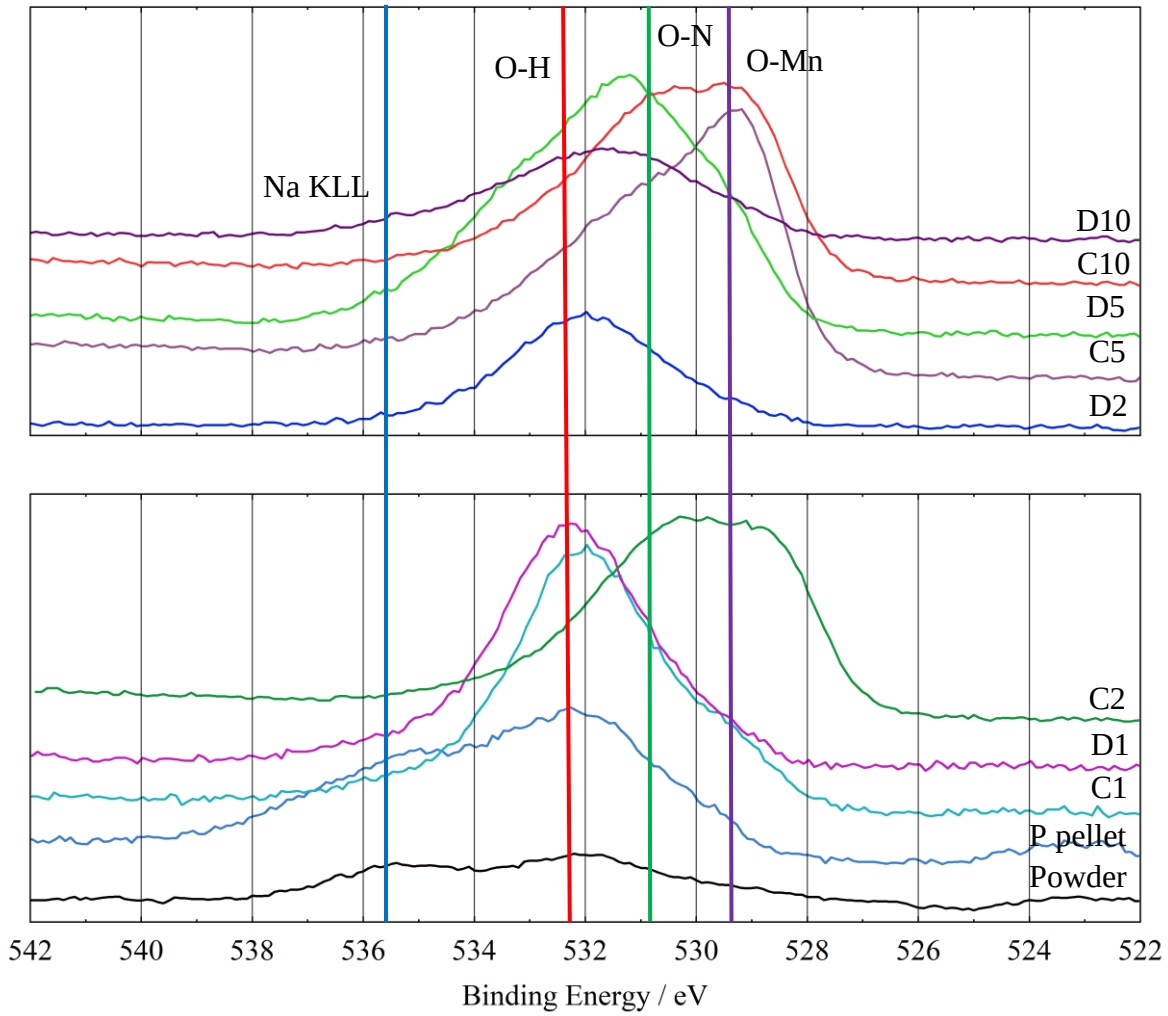

Figure 33: comparative spectra for O 1s peaks of the different samples for the MnHCF series

In the comparative spectra of the O 1s peaks for the MnHCF series (Figure 33), charged pellets show a peak around 529.4 eV that increases during cycling and it is higher for the charged samples and it is attributed to oxygen both coordinated by manganese and zinc. As shown below in the discussion of the Mn 2p comparative spectra, the charged samples always show significantly higher manganese content in XPS compared to the discharged ones.

As seen before in Chapter 3.2.1.3, the Na KLL lines around 524.0 eV, 534.8 eV and 536.8 eV disappear upon the first cycle due to the removal of the sodium from the structure.

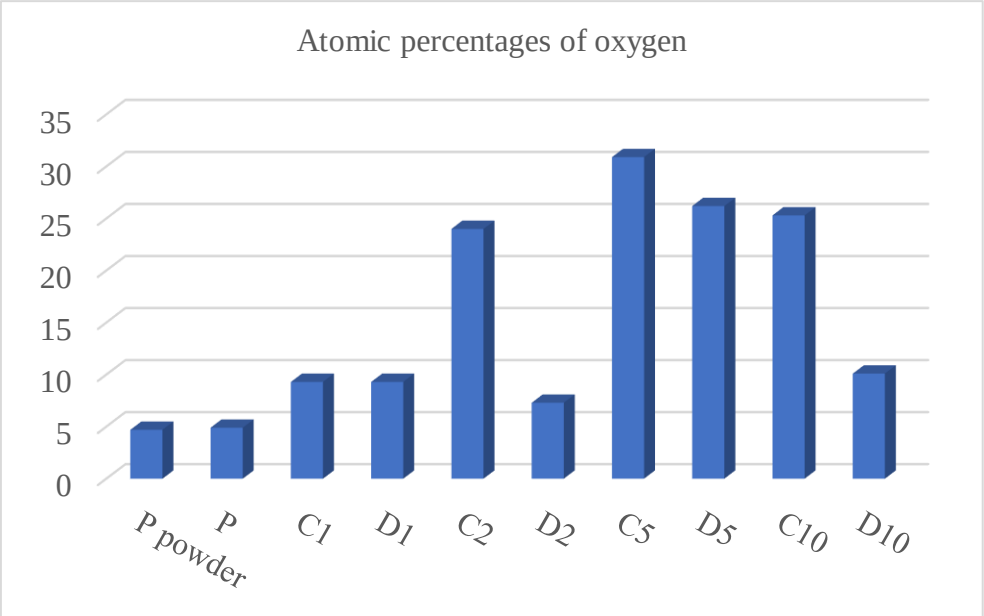

Figure 34: atomic percentages of oxygen in different samples in MnHCF series

As shown in Figure 34, the atomic percentage of oxygen is usually higher for the charged samples, granted the outlier D5.

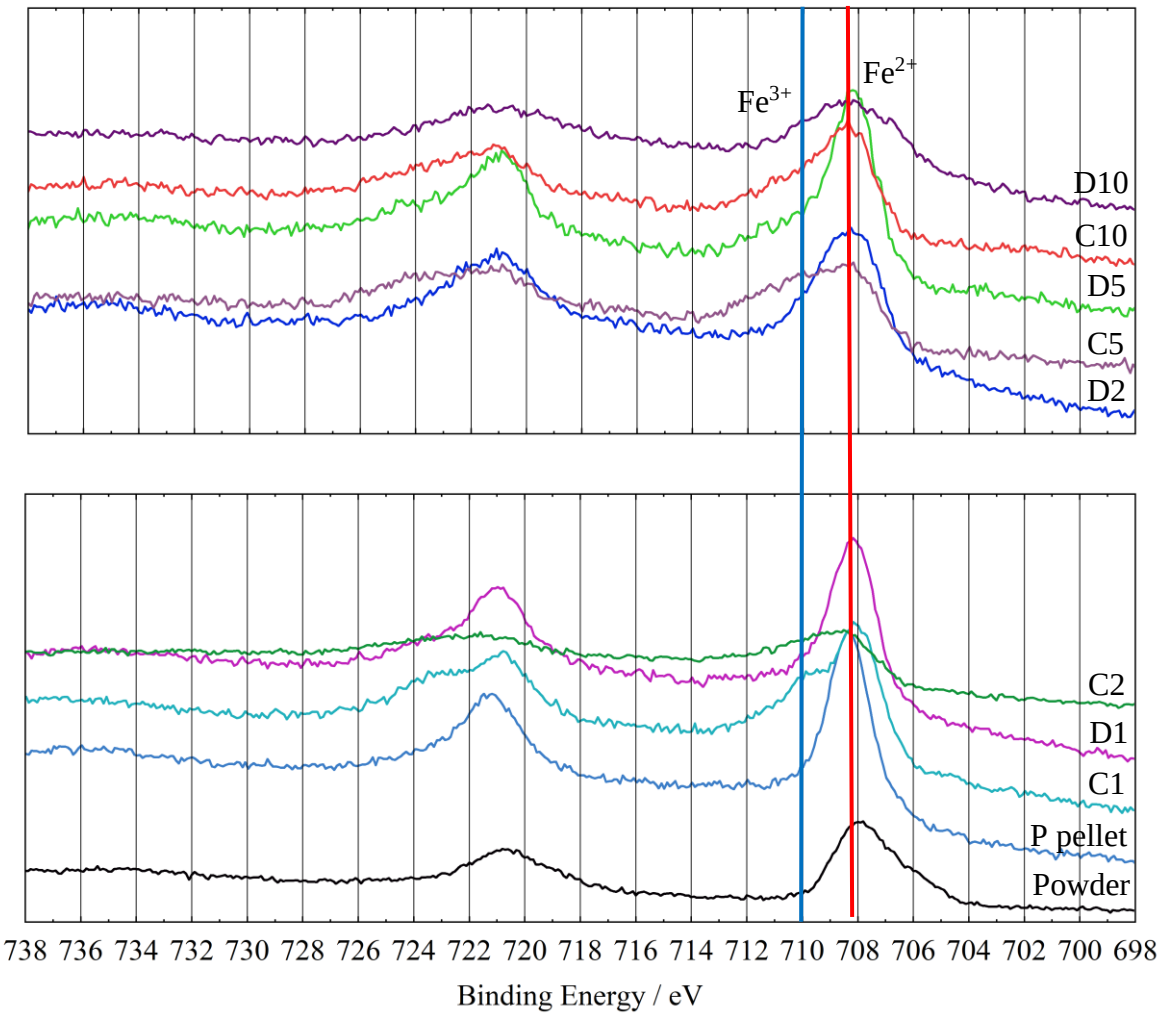

Figure 35: comparative spectra of Fe 2p peaks of the different samples for the MnHCF series

In Figure 35, the comparative spectra of the Fe 2p peaks of the different samples of the MnHCF series are reported and different oxidation states are observed. As expected, the powder, the pristine pellet and the discharged samples show a main peak around 708.3 eV and this peak was attributed to the Fe^{2+}. The C1 shows a second peak around 710 eV, and this was assigned to the Fe^{3+}. The other charged samples show a broad peak for Fe $2p_{3/2}$ and this is probably due to the oxidation of the iron. Also, the overall intensity of the Fe 2p signal of the charged samples seems to be lower.

Hereafter, the ratio between Fe^{2+} and Fe^{3+} in different samples in MnHCF series is reported in Figure 36. It is observed that the amount of Fe^{2+} is higher for discharged samples and the ratio decreases for the charge samples, except for the D10 pellet which is probably an outlier. This histogram confirms that iron is oxidized during the charge and reduced during the discharge segment.

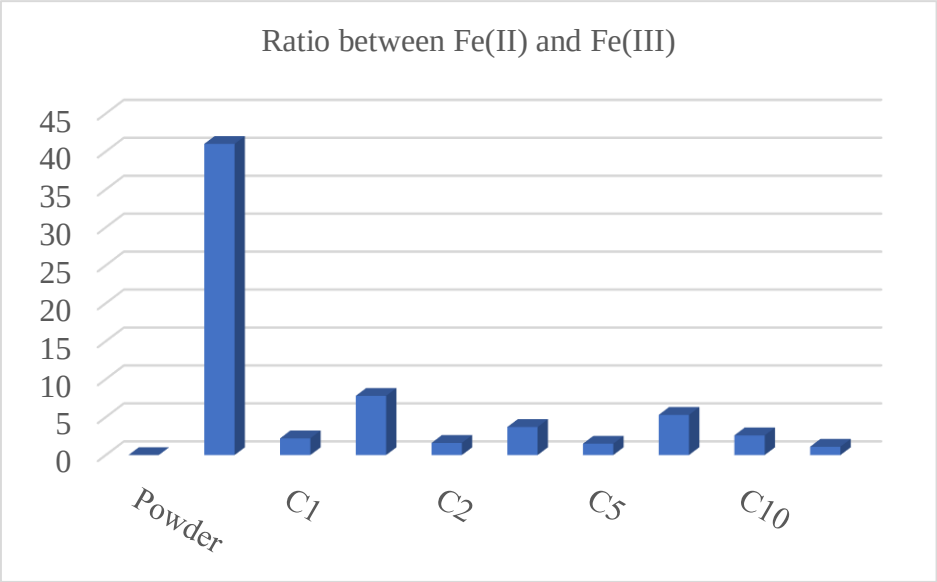

Figure 36: ratio between Fe^{2+} and Fe^{3+} in different samples in MnHCF series

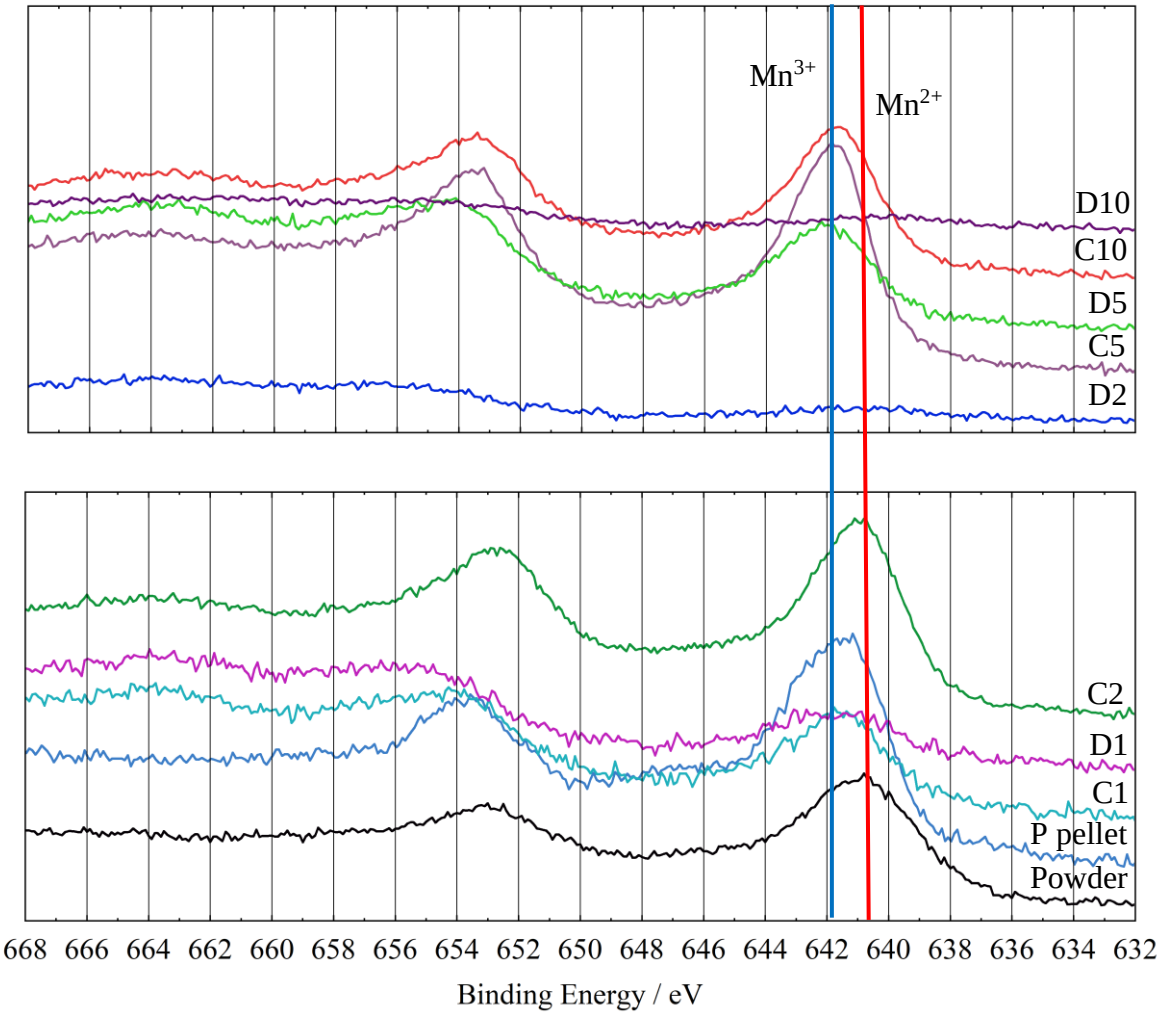

Figure 37: comparative spectra of Mn 2p peaks of the different samples for the MnHCF series

In the comparative spectra of the Mn 2p peaks of the different samples of the MnHCF series (Figure 37), there are many differences between the samples. In the pristine powder and in the C2 sample the signal is around 640.8 eV, it was assigned to Mn^{2+}. For the pristine pellet, C1, C5 and the C10 pellets, the peak is shifted to higher binding energies (641.8 eV) and this peak was attributed to Mn^{3+} as seen before in Chapter 3.2.1.3.

D5 sample show a lower amount of manganese and the peak is around 641.8 eV as the charged samples: this could be due to a non-complete reduction of the manganese during the last discharge segment. D1 show a low amount of manganese and D2, D10 samples don't show any Mn 2p signal: this could be due to the substitution of manganese with the zinc during cycling.

In contrast to that, in the comparative spectra of Mn 2p, the surface of the charged samples compared to the discharged ones enriches in Mn. As discussed before in the O 1s comparative spectra, the charged samples also exhibit a low binding energy component around 529.4 eV. A possible explanation could be that, during the charge segment, Mn-ions migrates to the cavities in the structure and the resident water molecules show a shift in O 1s due to the bonding to manganese while, during the discharge segment, manganese goes outside from the structure, and it is solved in the aqueous electrolyte solution. So, the electroactivity during charging would not be only due to the oxidation of Fe^{2+} to Fe^{3+}, but also the enrichment of the surface with Mn-ions.

Sample	**[O $1s_{529.4\ eV}$]/[Mn 3p]**
Pristine powder	0.3
Pristine pellet	0
C1	2
D1	0
C2	4.7
D2	0
C5	3.8
D5	0
C10	4.5
D10	0

Table 10: ratios between O 1s peak at 529.4 eV and Mn 3p signal at 48.5 eV

The ratio between the concentration of oxygen coordinated to the manganese and Mn-ions (Table 10) increases during cycling and it is almost constant for the samples treated with a high

number of cycles. This indicate that manganese goes inside the structure from the first cycle and the amount of water in the cavities increases during cycling.

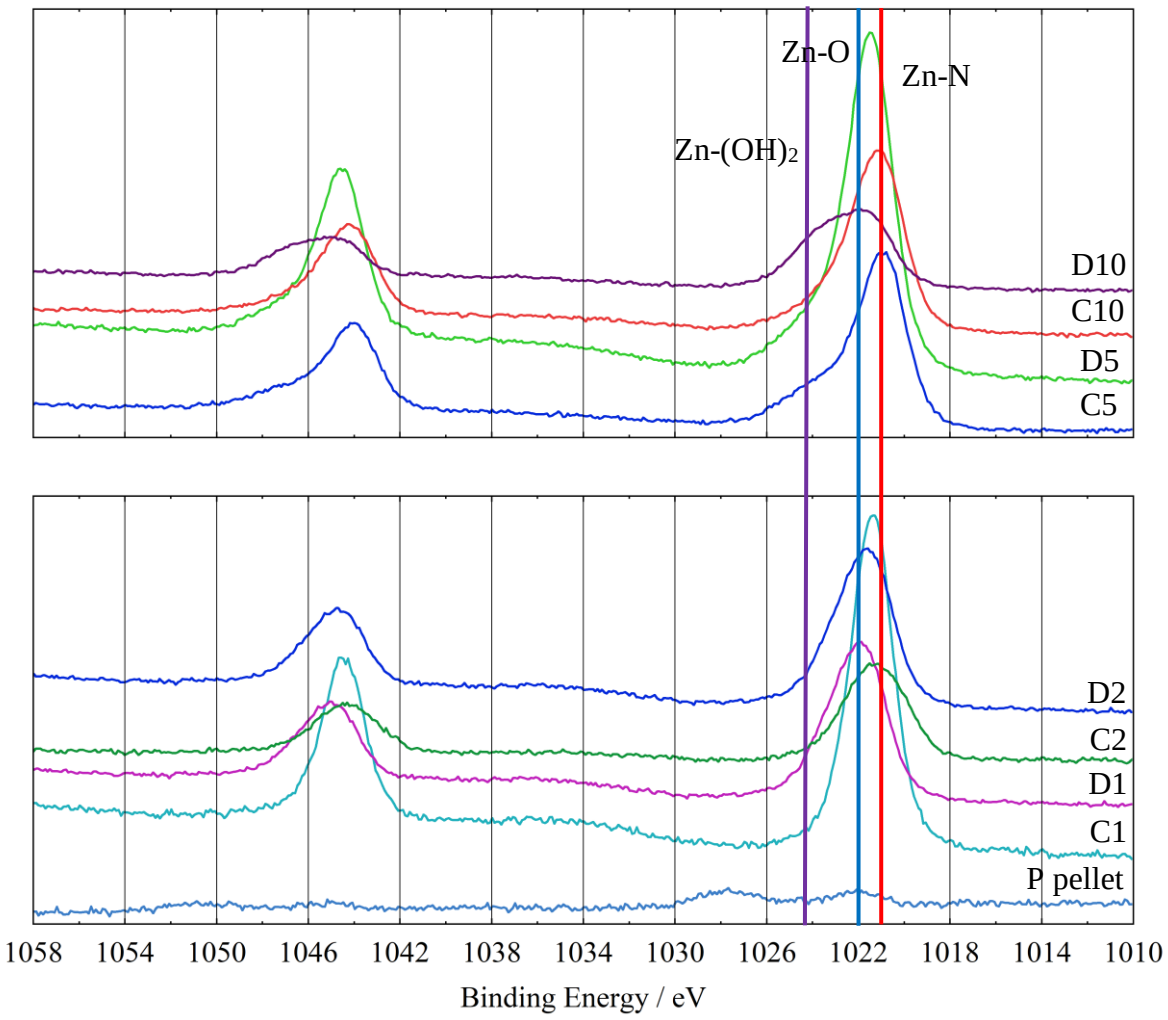

Figure 38: comparative spectra of Zn 2p peaks of the different samples for the MnHCF series

In the comparative spectra of Zn 2p peaks for the MnHCF series shown in Figure 38, the peak at 1024 eV increases during cycling but mostly for the discharged samples and this could be due to the presence of the zinc coordinated to two hydroxyl groups or water molecules inside the large cavities of the structure. Moreover, the charged samples show the Zn $2p_{3/2}$ peak more shifted to 1020.7 eV so it can be assumed that zinc substitute the manganese in the framework from the first cycle. The Zn $2p_{3/2}$ is more shifted to 1021.8 eV for the discharged samples, and this could be due to the insertion of the Zn in the large cavities of the structure during the discharge segment while it goes outside from the interstitial sites during the charge.

Hereafter, the atomic percentage of zinc (for the Zn $2p_{3/2}$ peak at 1021.8 eV) in different samples in MnHCF series is reported in Figure 39. It is observed that the concentration of zinc is higher

for discharged samples, and it decreases for the charge pellets, except for the D10 which is probably an outlier. This histogram supports the idea of the insertion of the zinc in the interstitial sites during the discharge and the removal of the Zn-ions from the cavities during the charge segment.

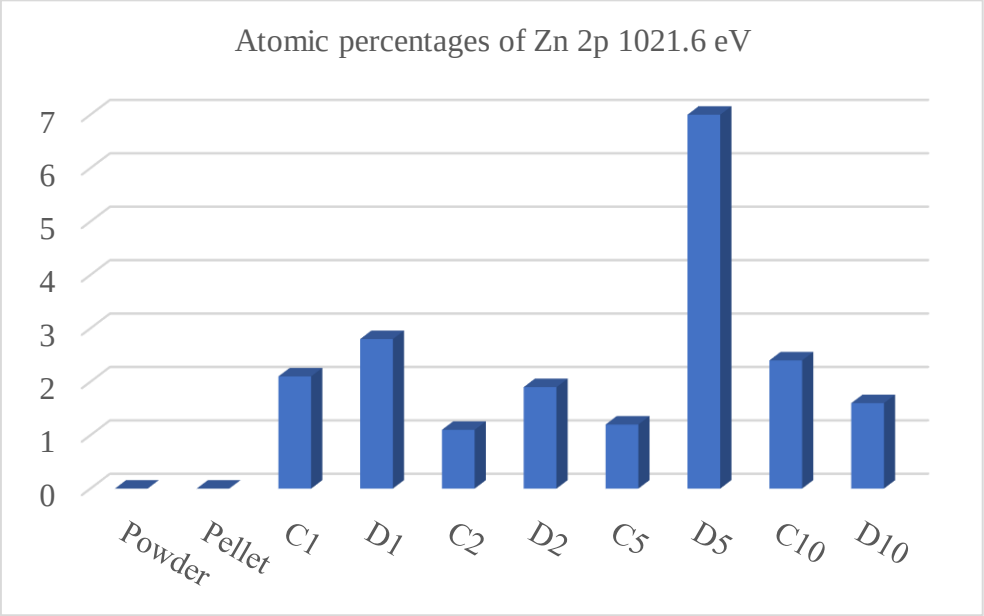

Figure 39: atomic percentages of Zn 2p 1021.8 eV in different samples in MnHCF series

3.2.2. Titanium hexacyanoferrate – three-electrode cell

It should be remarked that cyclic voltammetry measurements of these samples in the three-electrode cell did not show any clear oxidation and reduction peaks. Therefore, a comparative interpretation concerning the redox chemistry with XPS is not possible. So, in this chapter only a general characterization with XPS can be given and chemical changes other than alterations of oxidation states are determined.

3.2.2.1. Survey spectra of the TiHCF powder and exemplary formulated samples

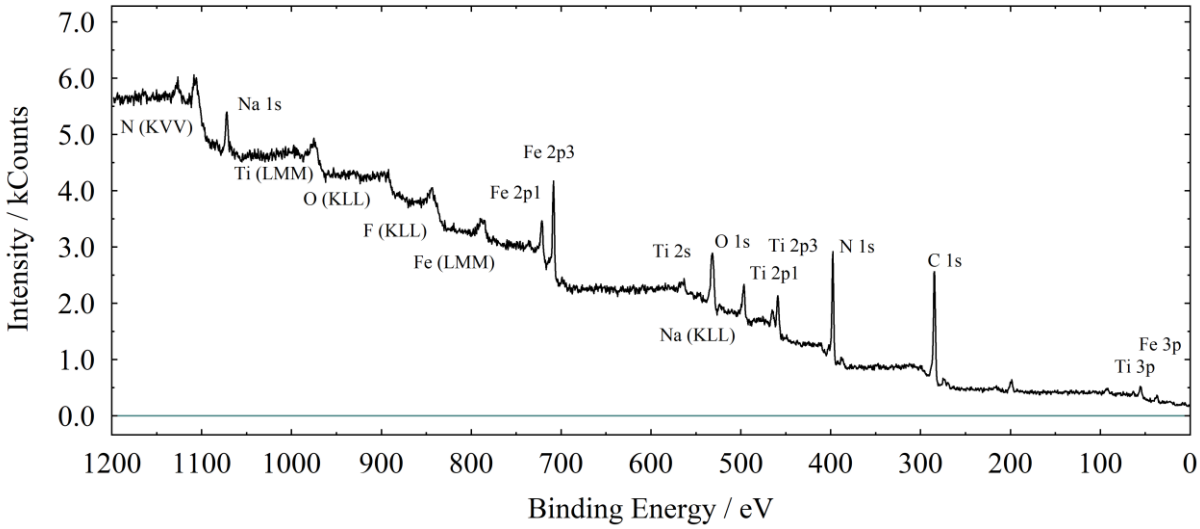

Figure 40: survey spectrum of the TiHCF powder used for formulation of the samples in the TiHCF series

In the survey spectrum of the powder of the TiHCF series (Figure 40), peaks of different elements are observed. As expected, there are the peaks of the titanium (458.7 eV – Ti 2p doublet) [22], iron (708 eV – Fe 2p doublet), nitrogen (397.6 eV – N 1s singlet) and carbon (around 285 eV – C 1s singlet) that compose the structure of the manganese hexacyanoferrate. Moreover, there is the peak of sodium (1071 eV – Na 1s singlet) which derive from the synthesis, and it is probably inside the large cavities in the structure. Also, the oxygen peaks (around 531 eV – O 1s singlet) are probably due to the presence of water in the cavities because of the aqueous solution.

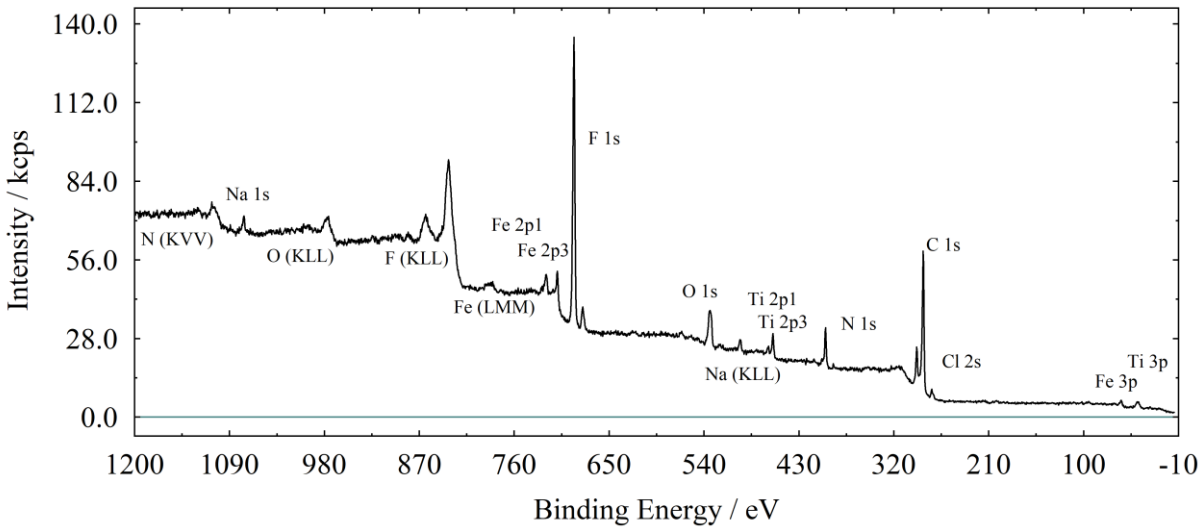

Figure 41: survey spectrum of the pristine pellet for the TiHCF series

In the survey spectrum of the pristine pellet of the TiHCF series shown in Figure 41, an additional F 1s singlet peak is observed around 690 eV. This intense peak is due to the polytetrafluoroethylene (PTFE) used for the preparation of the pellets.

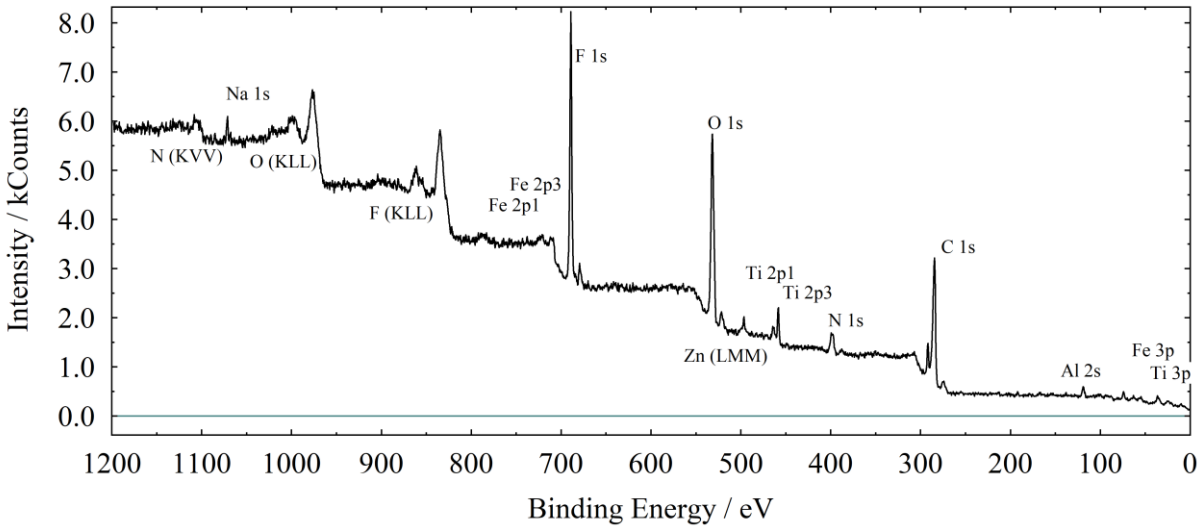

Figure 42: survey spectrum of the D10 pellet for the TiHCF series

In Figure 42, the survey spectrum of the "Discharged 10" pellet of the TiHCF series is reported. The Al 2s singlet peak is observed around 120 eV [22], and this probably comes from the aluminium mesh where the pellet was fixed for the three-electrode cell. Also, the O 1s peak is

obviously far more intense than in the pristine pellet survey. This will be further discussed in later chapters.

3.2.2.2. Quantification of the TiHCF powder

Hereafter, the atomic percentages of the different elements for the pristine powder used for formulation of the TiHCF series are reported in Table 11 and the ratios between N 1s of the cyanide and the metals of the pristine powder are shown in Table 12. The quantification was calculated with the fit obtained from the detailed spectra and, for the pristine powder, the Fe 2p peaks were used for the quantification because there are not the loss structure of F 1s under the Fe 2p signals.

	N	**Na**	**C**	**O**	**Ti**	**Fe**	**Cl**
Pristine powder	23.6	3.8	49.6	12.7	3.9	3.9	2.5

Table 11: atomic percentages of the different elements for the pristine powder of the TiHCF series

The XPS quantification of the powder suggests successful synthesis of the TiHCF powder. The content of Na is due to the synthesis procedure, oxygen derives from water in the cavities and chlorine comes from the synthesis since hydrochloric acid was used for the preparation of TiHCF powder. A quantification of carbon relative to the metals is difficult since adventitious hydrocarbons overlap with C 1s cyanide signal.

	$[N_{(CN)}]/[Fe_{2p}]$	**$[N_{(CN)}]/[Ti_{2p}]$**	**$[Fe_{2p}]/[Ti_{2p}]$**
Pristine powder	5.5	5.5	1.0
Theoretical ratios	6.0	6.0	1.0
Ratios from previous work [15]	8.2	6.0	1.4

Table 12: ratios between nitrogen of the cyanide (397.6 eV) and the metals of the powder used for the formulation of the pellets of the MnHCF series

As expected, the ratios between the nitrogen of the cyanide and the metals are around 5.5 and theoretically, iron and titanium centres are surrounded by six cyanides in the TiHCF structure.

3.2.2.3. XPS fitting of detailed spectra of the TiHCF series - the three-electrode cell

A set of parameters for all detailed scans Fe 3p, C 1s, N 1s, O 1s, Ti 2p and Fe 2p were extracted from the TiHCF powder sample and used for the fitting of the series of cycled TiHCF samples. The width of the Gaussian and Lorentzian functions in the convolutions were set constant resulting in FWHM/eV of 2.6 for Fe 3p doublet, 1.8 for C 1s singlet, 1.9 for N 1s singlet, 2.3 for O 1s singlet, 2.0 for Ti 2p doublet and 2.3 Fe 2p doublet. Binding energy positions of components in the detailed spectra were allowed to vary a range of ± 0.3 eV.

For the TiHCF – three-electrode cell, the analysed samples were mainly reduced (pristine powder, pristine pellet and discharged pellets), only the C1 should be oxidized and this is why a full comparison is not possible.

Hereafter, exemplary fittings are reported using detailed spectra of the formulated pellet of TiHCF without cycling complemented by other examples if needed.

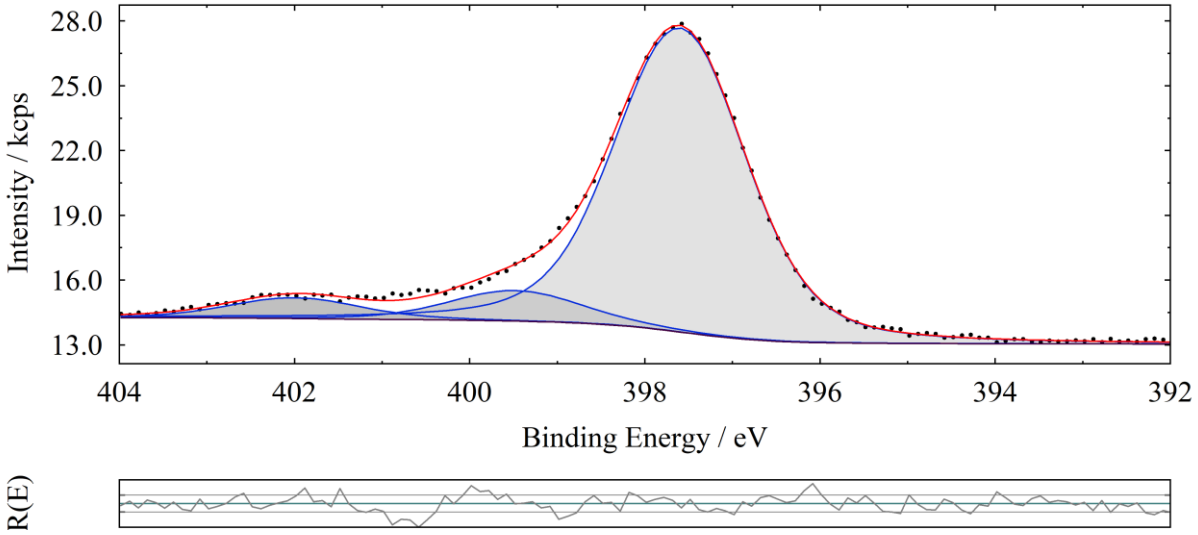

Figure 43: N 1s peaks of the pristine pellet for the TiHCF series

As seen above in Chapter 2.3, charge correction was performed on N 1s signal, and the main peak was fixed at 397.6 eV.

In the fit of the N 1s peaks for the pristine pellet of the TiHCF series (Figure 43), three peaks are observed: the main peak around 397.6 eV was assigned to the nitrogen of the cyanide [29], the peaks around 399.4 eV and 402 eV could be due to the nitrogen coordinated to the hydrogen and to the nitrogen coordinated to the oxygen of the water that is inside the large cavities in the

structure. [29,30] As in the case of the MnHCF series explained in Chapter 3.2.1.3, this can be correlated to an increase in oxygen during cycling. Demonstrative comparative spectra will be shown in the next chapter.

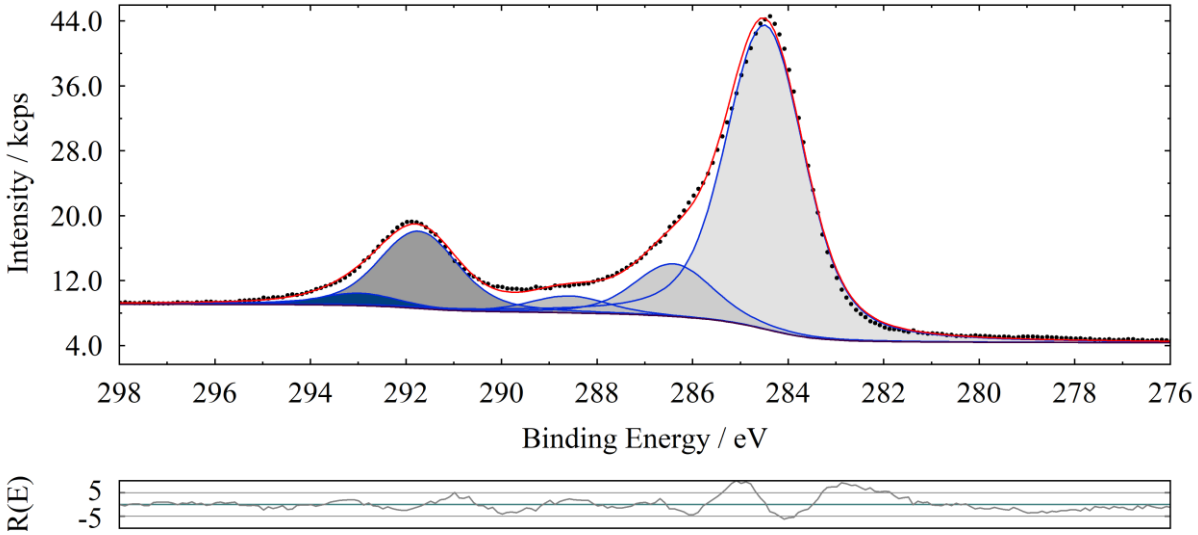

Figure 44: C 1s peaks of the pristine pellet for the TiHCF series

As seen above in Chapter 2.3, for cross-checking of the charge correction, the signal of conductive carbon was observed to be in the range of 284.5 eV ± 0.3 eV.

In Figure 44, the fit of the C 1s peak for the pristine pellet of the TiHCF series is shown and five peaks are observed: the main signal at 284.5 eV could be assigned to the carbon of the cyanide [31]. We cannot do a deconvolution of C 1s (-CN) and C 1s (conductive carbon) because they are too close in binding energy. The other peak at 286.4 eV and 288.6 eV could be assigned to simple carbon-oxygen bonds and –CHF–CHF– bonds as well as carboxylate groups respectively. [30,32] The peaks around 291.8 eV and 293 eV could be assigned to the –CF_2– bonds of the PTFE. [44,45] The interpretation of the C 1s is therefore analogous to the MnHCF series.

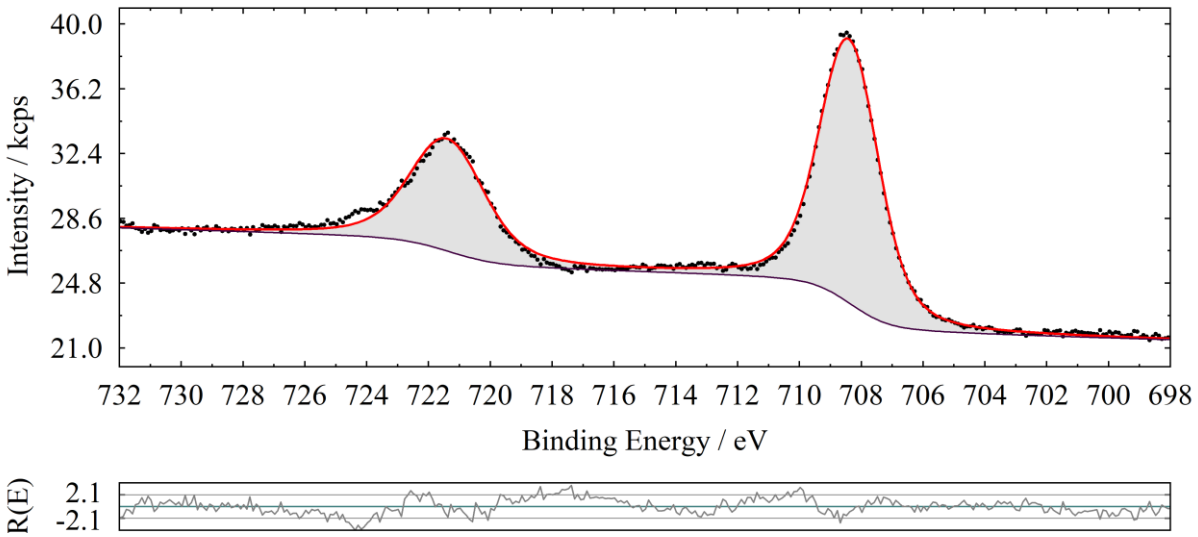

Figure 45: Fe 2p peaks of the TiHCF powder used for formulation of the samples in the TiHCF series

In the fit of the powder used for the formulation of the samples in the TiHCF (Figure 45), the Fe $2p_{3/2}$ is around 708.4 eV, and it was assigned to Fe^{2+} according to literature [34,35].

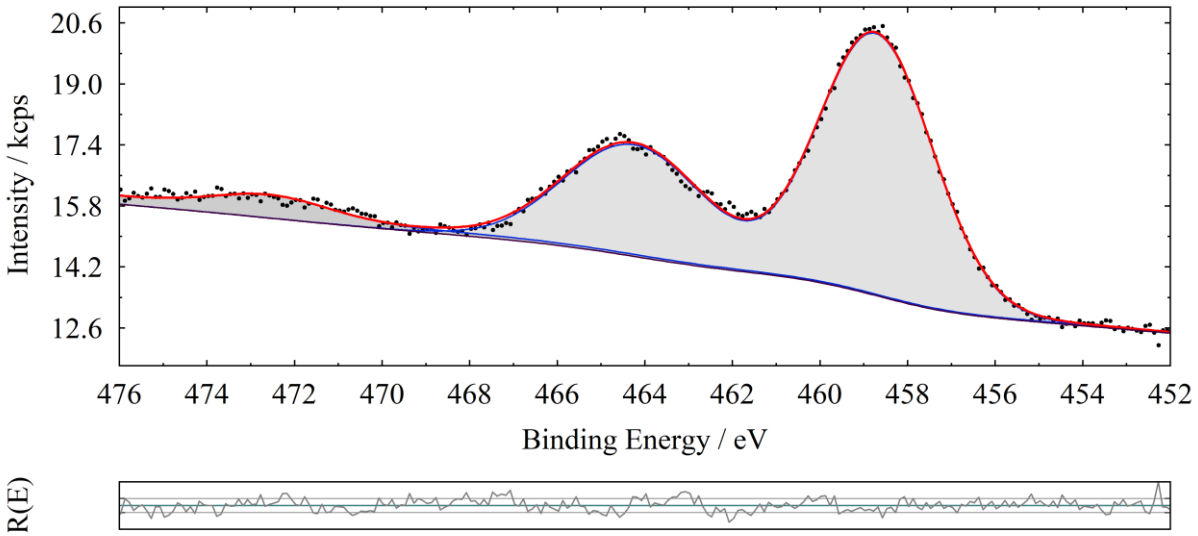

Figure 46: Ti 2p peaks of the TiHCF powder used for formulation of the samples in the TiHCF series

In the fit of the Ti 2p peaks of the pristine pellet for the TiHCF series shown in Figure 46, there is the $2p_{3/2}$ peak at 458.7 eV and this peak could be assigned to the Ti^{4+} coordinated to the nitrogen of the cyanide. [16]

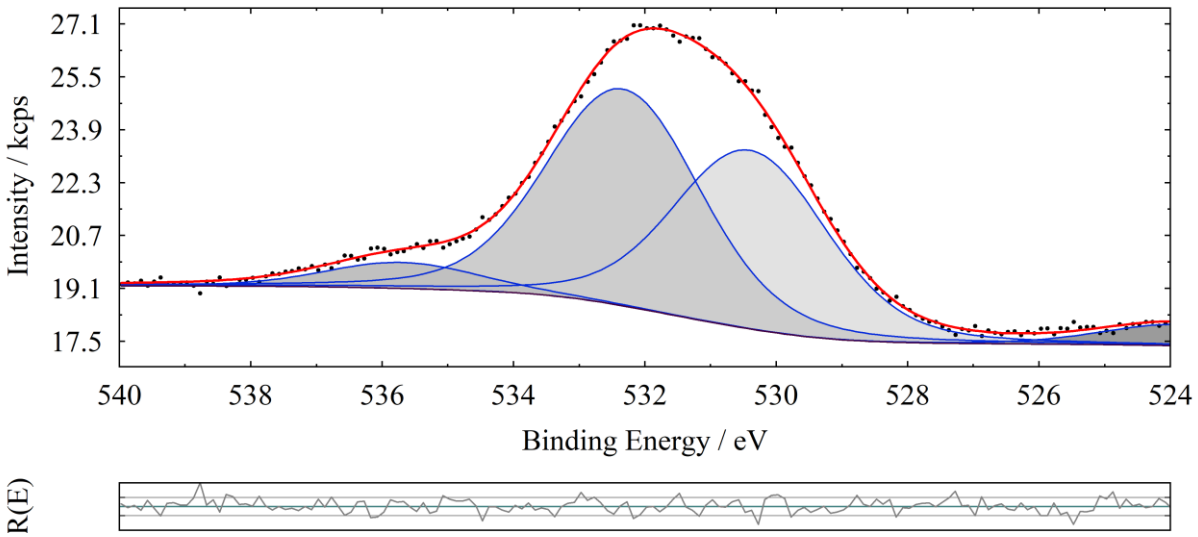

Figure 47: O 1s peaks of the TiHCF powder used for formulation of the samples in the TiHCF series

In the fit of O 1s of powder used for the formulation of TiHCF pellets (Figure 47), there are four signals: the peaks around 530.4 eV and 532.3 eV were attributed to the oxygen coordinated to the nitrogen and to the oxygen of the water that is inside the cavities of the structure. [29] Moreover, the two signals at 524.1 eV and 535.7 eV were assigned to Na KLL Auger Lines [22] and they were not counted in the quantification of the oxygen.

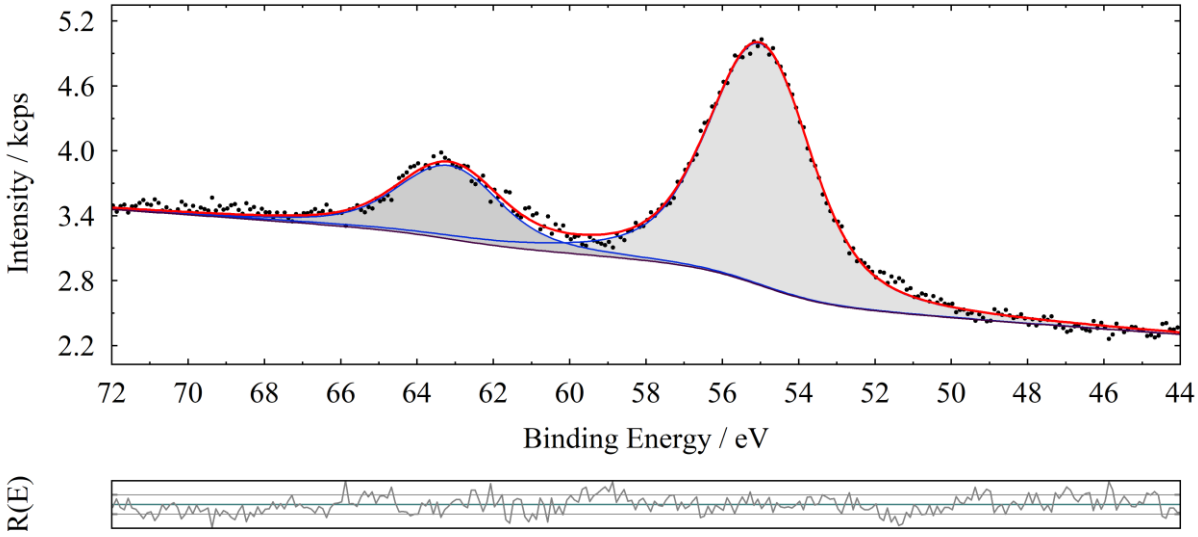

Figure 48: Fe 3p peak of the TiHCF powder used for formulation of the samples in the TiHCF series

Figure 48 shows the Fe 3p and Na 1s peaks of the powder used for formulation of the samples in the TiHCF series, the peak at 54.7 eV was assigned to Fe^{2+} according to literature [34,35]

and to previous detailed spectra (Figure 45) and the peak at 63.4 eV is Na 2s signal. [22] The Fe 3p signal was used for the quantification of the iron inside the sample.

The overview of the fitting results and quantification can be found in the Appendix.

3.2.2.4. Comparative spectra for the samples of the TiHCF series - three-electrode cell

Subsequently, the comparative spectra are reported for the evaluation of the change of the oxidation states for different samples and other chemical changes after cycling

As in Chapter 3.2.1.4, the comparative spectra include curves of absolute intensity in counts/sec. A constant background has been removed equalling the base line at the lower binding energy side.

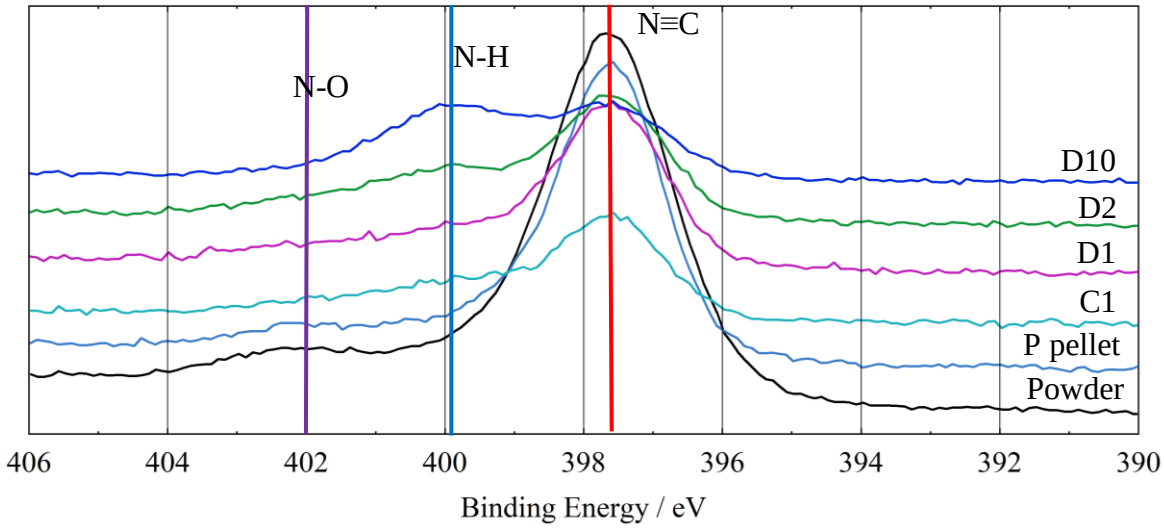

Figure 49: comparative spectra of N 1s peak of the different samples for the TiHCF – three-electrode cell

In Figure 49, the comparative spectra of the N 1s of the different samples for the TiHCF series are shown: a second peak around 399.4 eV increases during cycling and it is intense for the D10 sample. As seen above in Chapter 3.2.2.3, this peak was assigned to the nitrogen coordinated to the hydrogen of the water that goes inside the large cavities of the structure during cycling.

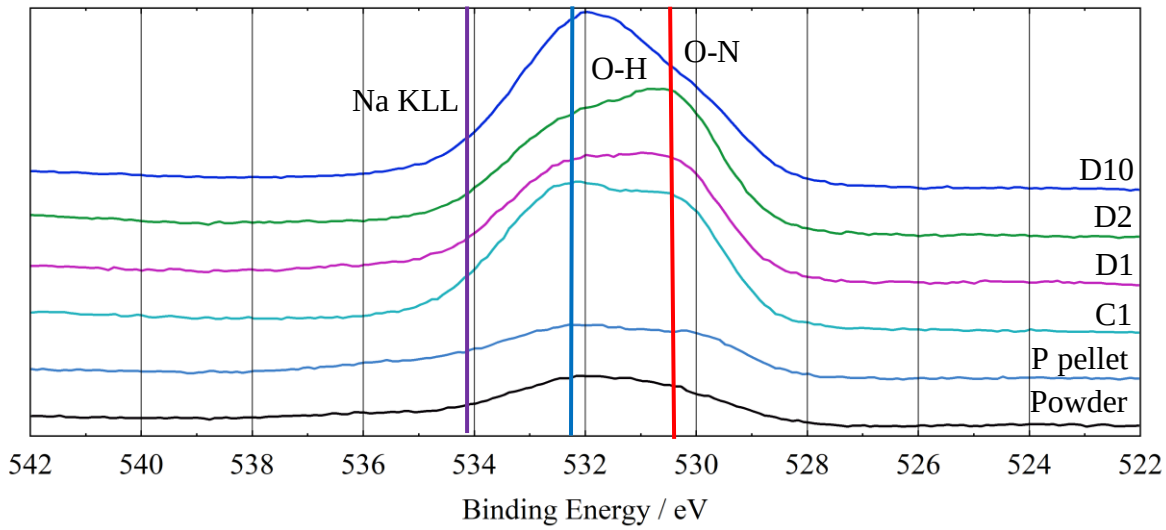

Figure 50: comparative spectra of O 1s peak of the different samples for the TiHCF – three-electrode cell

In the comparative spectra of the O 1s peaks for the TiHCF series (Figure 50), the peak around 532.5 eV increases during cycling and this is probably due to the insertion of water inside the large cavities of the structure.

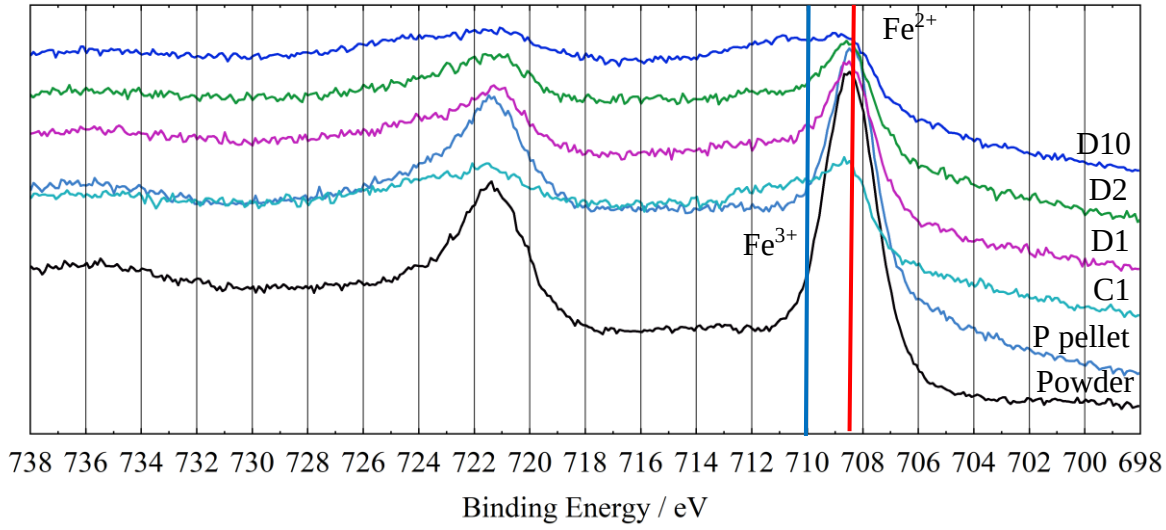

Figure 51: comparative spectra of Fe 2p peaks of the different samples for the TiHCF – three-electrode cell

In the comparative spectra of the Fe 2p peaks of the different samples of the TiHCF series shown in Figure 51, the iron signal is around 708.4 eV for the powder, the pristine pellet and the discharged sample and it was assigned to Fe^{2+}. The Fe $2p_{3/2}$ peak of the C1 sample is broader than other samples and this is probably due to the oxidation of the iron during the charge

segment. As seen above in Chapter 3.1.2, the cyclic voltammetry of the C1 sample does not show the peak around 1.2 V and, probably, this is the reason why the Fe 2p peak does not show a clear peak around 710.0 eV for the oxidation of the iron.

Here, the overlap of the F 1s loss structure must be kept in mind, which contributes to the shape of the curve. As already mentioned, the cyclic voltammetry of these samples does not show the expected oxidation and reduction features. So, it does not appear justified to assume higher or lower oxidation states for the transition metal for charged and discharged samples respectively.

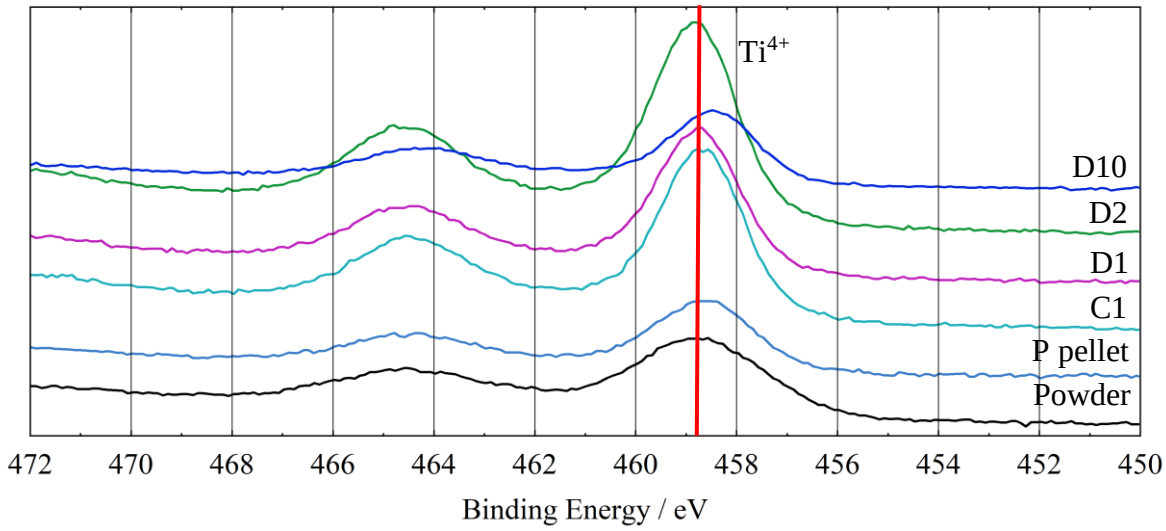

Figure 52: comparative spectra of Ti 2p peaks of the different samples for the TiHCF – three-electrode cell

In Figure 52, the comparative spectra of Ti 2p peaks of the different samples for the TiHCF series – three-electrode cell are shown: the peaks are almost in the same position for all the samples. Theoretically, for the C1 sample titanium should be oxidized and for the pristine powder, the pristine pellet and the discharged samples titanium should be reduced: but as seen above in the comparative spectra, the Ti 2p peaks of discharged samples were assigned to Ti^{4+}. CV scans of all the discharged samples are reported in the Appendix: in the CV scan of D1 sample is observed a small hump at 0.05 V which could be assigned to the reduction of titanium but for D2 and D10 pellets no reduction peak is observed for titanium.

Hereafter, Table 13 reports the binding energies of the peaks for titanium and it confirms the oxidation state does not change between the charged and the discharged samples.

	Pristine powder	Pristine pellet	C1	D1	D2	D10
Ti 2p peak positions	458.7	458.6	458.7	458.7	458.8	458.4

Table 13: binding energies of the main component in Ti 2p of the different samples of the TiHCF – three-electrode cell

3.2.3. Titanium hexacyanoferrate – symmetric coin cell

In this chapter, the comparative spectra acquired for TiHCF – symmetric coin cell will be discussed. Survey spectra, quantification of the powder and XPS fitting scheme of the detailed spectra will not be shown because it is analogous to the TiHCF – three-electrode cell previously discussed in Chapters 3.2.2.1, 3.2.2.2 and 3.2.2.3. In this case, the cyclic voltammetry measurements of the samples show clear oxidation and reduction peaks and all the CV scans are reported in the Appendix.

3.2.3.1. Comparative spectra for the samples of the TiHCF series – symmetric coin cell

As seen above in Chapter 3.2.2.4, the comparative spectra include curves of absolute intensity in counts/sec. Again, a constant background has been removed equalling the base line at the lower binding energy side. Hereafter, pellets are called: C1-A and C1-C are the anode (A) and cathode (C) after the first charging cycle, D1-A and D1-C are anode (A) and cathode (C) after the first discharging cycle respectively. The overview of the fitting results and quantification can be found in the Appendix.

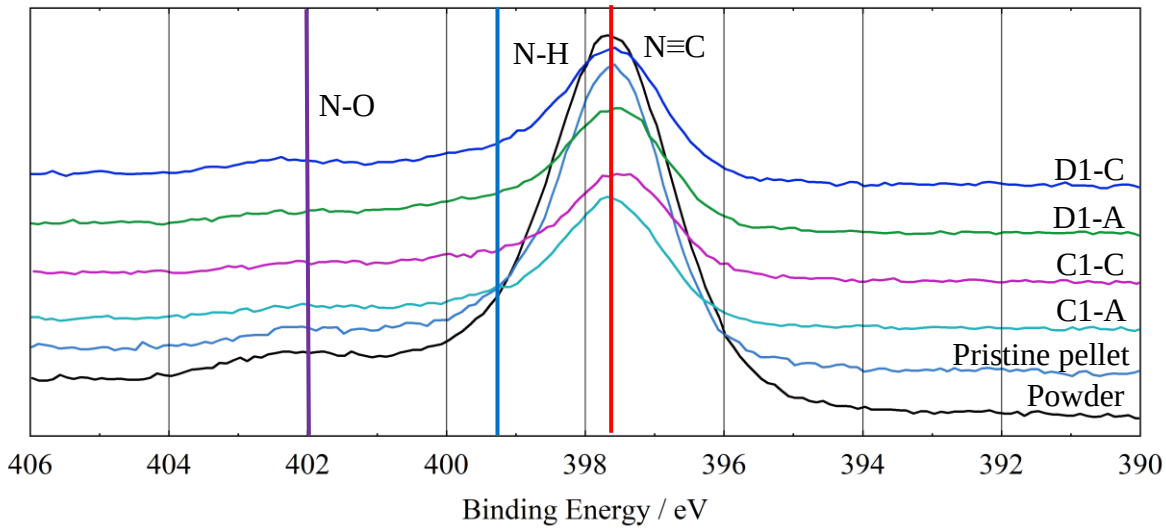

Figure 53: comparative spectra of N 1s peaks of the samples for the TiHCF series – symmetric coin cell

In Chapter 3.2.2.4, in the comparative spectra of N 1s peaks of the samples for the TiHCF three-electrode cell, a second peak around 399.4 eV increases during cycling and it is intense for the D10 sample. In Figure 53, the comparative spectra of the N 1s of the different samples for the TiHCF series – symmetric coin cell are shown and the samples do not show any relevant differences, this is most probably due to the performance of only one cycle.

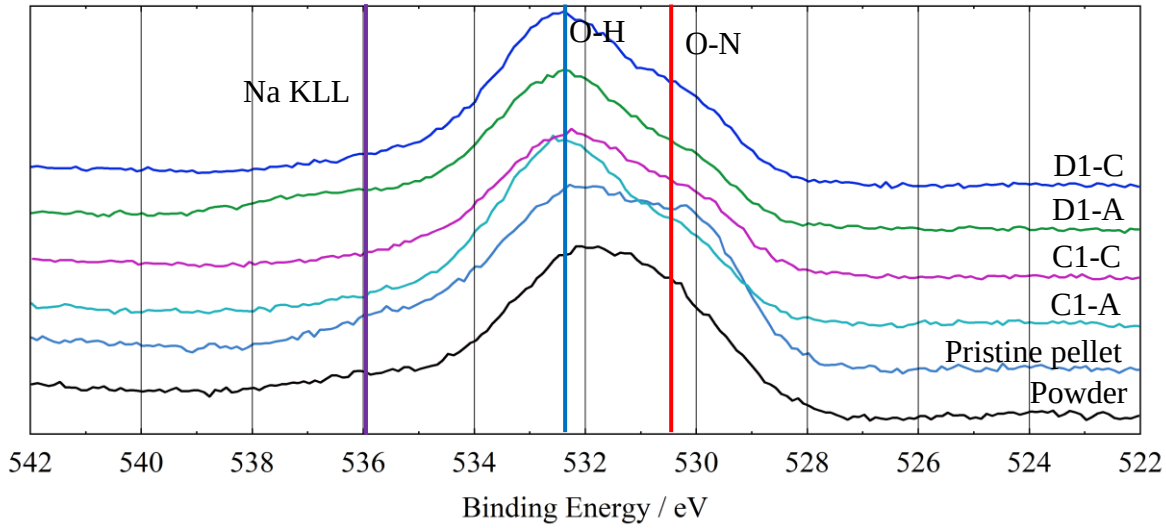

Figure 54: comparative spectra of O 1s peaks of the samples for the TiHCF series – symmetric coin cell

In Figure 54, the comparative spectra of O 1s peaks of the samples for TiHCF series are reported and it is observed that this series does not show strong increase in the intensity of the O 1s peak, since the samples shown are, almost, fully cycled once.

As seen above in Chapter 1.4, the metals should be oxidized in the cathode and reduced in the anode, the expected oxidation states for iron and titanium are:

- Fe^{3+} and Ti^{4+} in the cathode.
- Fe^{2+} and Ti^{3+} in the anode.

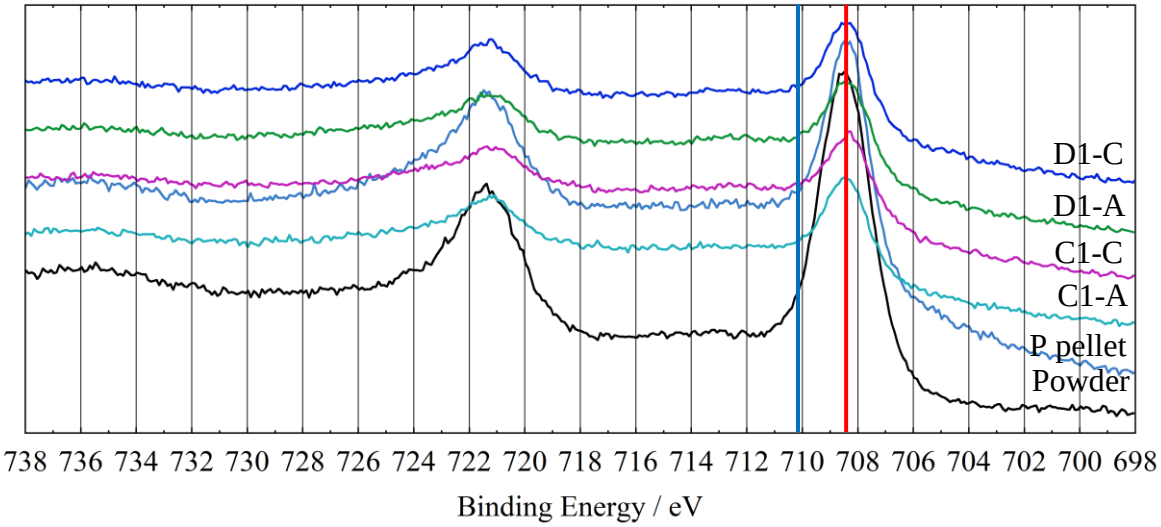

Figure 55: comparative spectra of Fe 2p peaks of the samples for the TiHCF series – symmetric coin cell

In the comparative spectra of the Fe 2p peaks of the different samples of the TiHCF series (Figure 55), the iron signal is around 708.4 eV for all the pellets, and it was assigned to Fe^{2+} according to literature. [34,35] Expected position of Fe^{3+} peak would be around 710.3 eV as reported in literature [31,35] and in these comparative spectra, no Fe $2p_{3/2}$ signal is observed at this BE.

Again, the overlap of the F 1s loss structure must be kept in mind, which contributes to the shape of the curve. In the symmetric coin cell setup, the samples showed distinct oxidation and reduction events in cyclic voltammetry so it may be speculated that, after removing the sample from the electrochemical setup, the oxidation states in the surface are not conserved. Comparing to the MnHCF series, the latter is characterized by major chemical changes (e.g., introduction of Zn-ions) which may stabilize the surface state also after removing from the electrochemical setup.

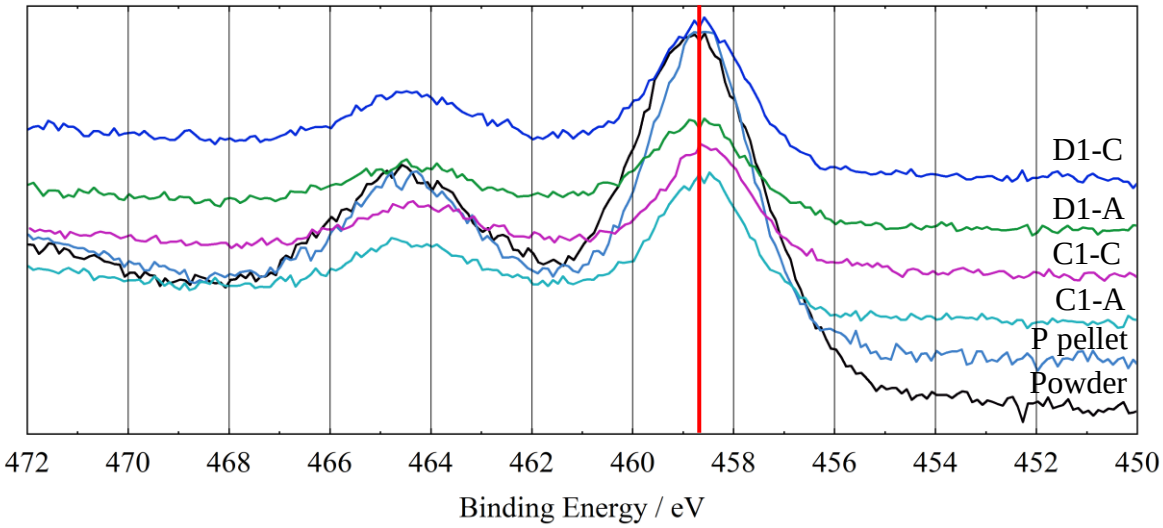

Figure 56: comparative spectra of Ti 2p peaks of the samples for the TiHCF series – symmetric coin cell

In Figure 56, the comparative spectra of Ti 2p peaks of the different samples for the TiHCF series – symmetric coin cell are shown: the peaks are in the same position for all the samples, and they were assigned to Ti^{4+} according to literature. [16] Theoretically, titanium that should be oxidized for C1-C and D1-C samples and it should be reduced for the pristine powder, the pristine pellet, the C1-A and D1-A samples. Again, the samples showed distinct oxidation and reduction events in cyclic voltammetry so it may be speculated that, after removing the sample from the electrochemical setup, the oxidation states in the surface are not conserved.

Hereafter, binding energies of the main component in Ti 2p and Fe 3p peaks for the different samples in TiHCF – symmetric coin cell are reported in Table 14, and it is not possible to observe any systematic chemical changes for the transition metals.

BINDING ENERGIES (eV)		
	Ti (2p)	**Fe (3p)**
Pristine powder	458.7	54.7
Pristine pellet	458.6	54.8
C1 – A	458.7	54.9
C1 – C	458.7	54.8
D1 – A	458.8	54.8
D1 – C	458.4	55.2

Table 14: binding energies of the main component in Ti 2p and Fe 3p for the different samples in TiHCF - symmetric coin cell

4. CONCLUSIONS

XPS analyses was fundamental to understand the chemical changes and alterations of the oxidation states of the metals for MnHCF and TiHCF series after the treatment with cyclic voltammetry.

For the manganese hexacyanoferrate electrodes treated with CV in coin cell, it was observed that there are many differences between samples treated with different number of cycles. Firstly, the oxidation state of iron changes during cycling because it is reduced for the discharge samples and oxidized for the charged ones. Secondly, zinc substitutes manganese in the framework from the first cycle. Moreover, the surface of the charged samples compared to the discharged ones enriches in manganese while the concentration of Zn-ions decreases during the charge and enhances during the discharge segment. A possible explanation could be that, during the charge segment, Mn-ions migrates in the interstitial sites and Zn-ions goes outside from the large cavities of the structure while, during the discharge segment, manganese goes outside, and zinc goes inside the interstitial sites. So, the electroactivity shown during cycling would not be only due to the oxidation and reduction of iron, but also the mobility of Mn and Zn-ions, as expected from electrochemical viewpoint. Finally, it can be assumed that Zn and Mn-ions are coordinated to the water inside the large cavities of the manganese hexacyanoferrate structure.

For the TiHCF series treated with CV in three-electrode cell and symmetric coin cell, there are not any relevant differences in oxidation state between samples treated with different number of cycles.

For the three-electrode cell, it must be kept in mind that titanium hexacyanoferrate has shown electrochemical activity when the pellet was pressed inside the aluminium mesh. Afterwards, the pellets were fixed inside the aluminium mesh with a clip with the aim of recovering them after the CV to perform XPS measurement. CVs were not as expected: they do not show any clear reduction peaks for the metals in discharged samples and, probably, the surface contact was lost during cycling.

In the symmetric coin cell setup, the samples showed distinct oxidation and reduction events in cyclic voltammetry. It may be speculated that, after removing the sample from the electrochemical setup, the oxidation states in the surface are not conserved. Comparing to the MnHCF series, the latter is characterized by major chemical changes and as seen above, the substitution of the manganese in the framework by the Zn-ions during cycling and the mobility

of Mn and Zn-ions could stabilize the surface state also after removing it from the electrochemical setup. So, for the MnHCF series, the electroactivity shown during cycling would not be only due to the oxidation and reduction of iron, but also the movement of Mn and Zn-ions while, for the TiHCF series, the electroactivity shown during cycling is probably due to the oxidation and reduction of the metals and maybe to the mobility of Na-ions.

5. APPENDIX

5.1. Cyclic voltammetry

5.1.1. Manganese hexacyanoferrate – coin cell

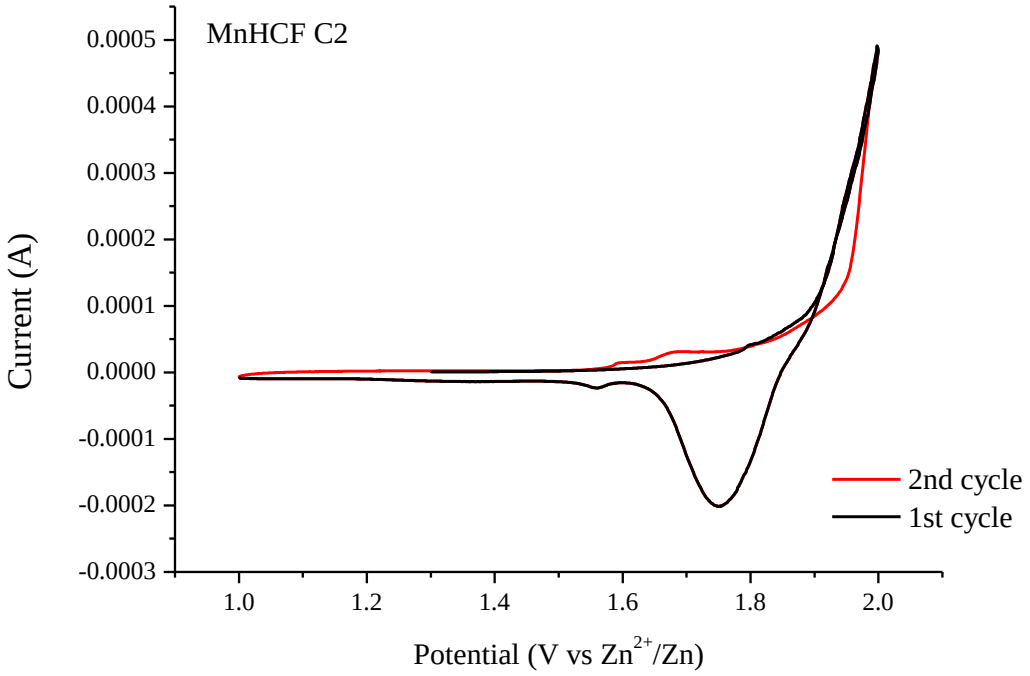

Figure 57: cyclic voltammetry scan for the sample C2 of the MnHCF series – coin cell

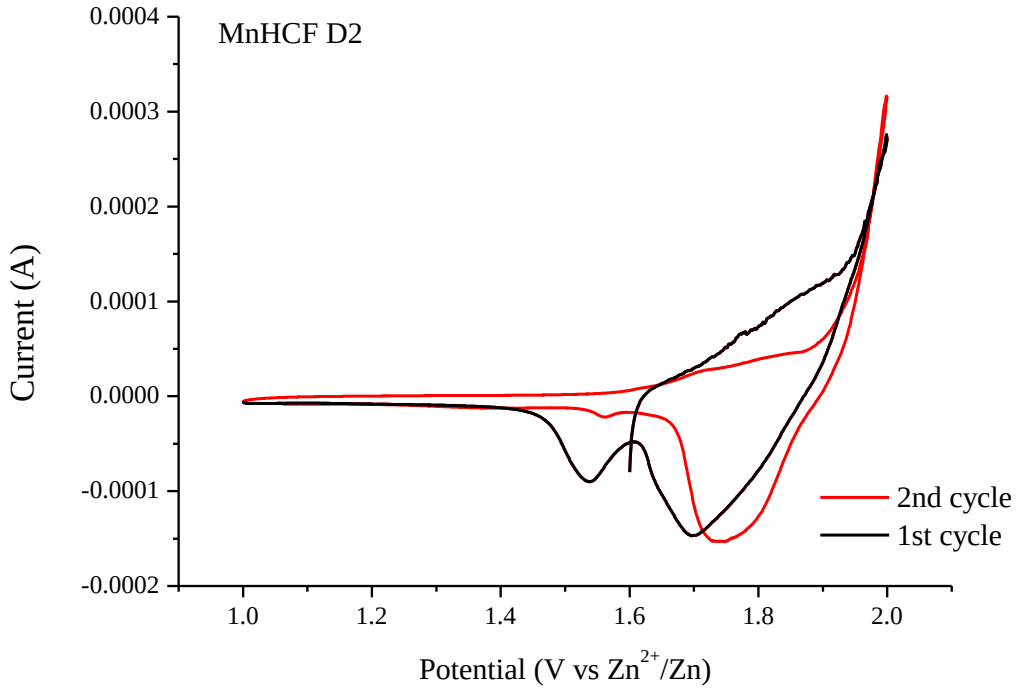

Figure 58: cyclic voltammetry scan for the sample D2 of the MnHCF series – coin cell

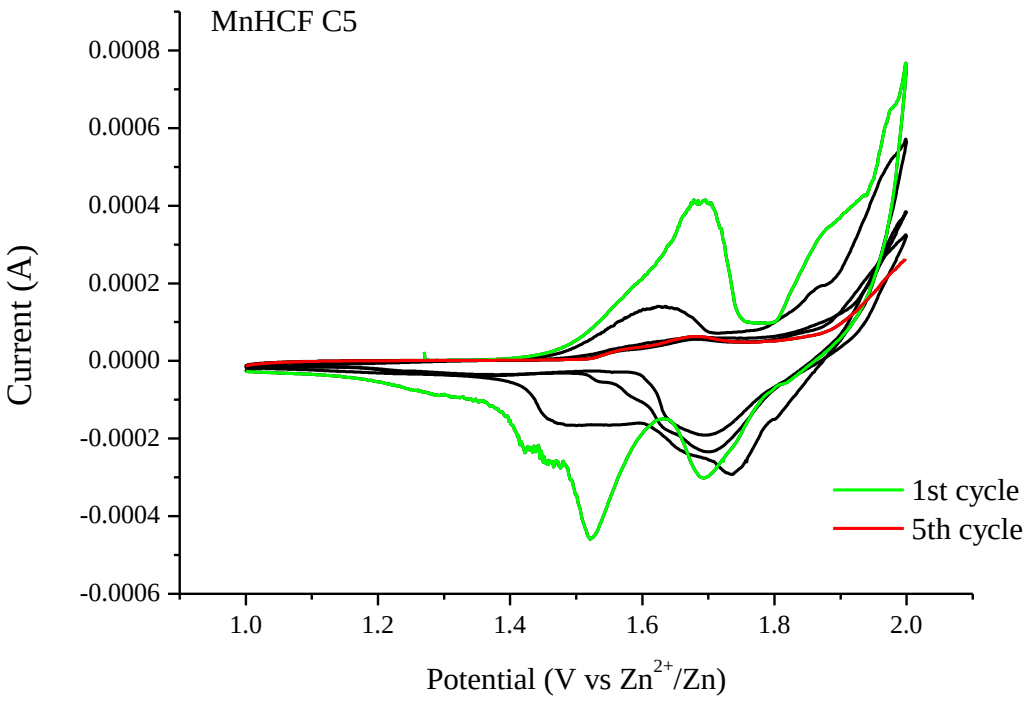

Figure 59: cyclic voltammetry scan for the sample C5 of the MnHCF series – coin cell

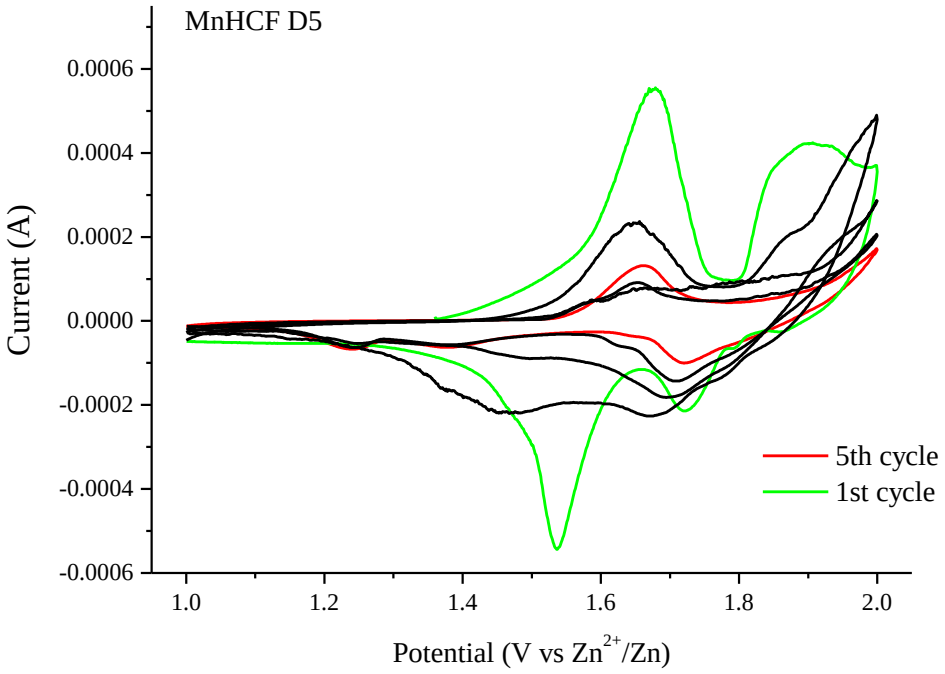

Figure 60: cyclic voltammetry scan for the sample D5 of the MnHCF series – coin cell

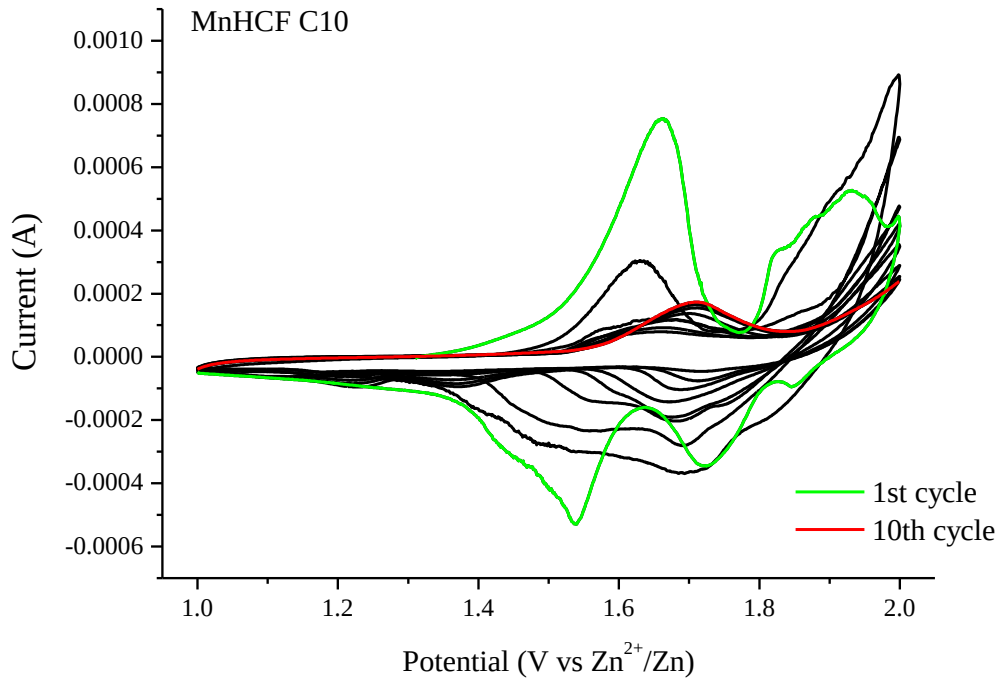

Figure 61: cyclic voltammetry scan for the sample C10 of the MnHCF series – coin cell

5.1.2. Titanium hexacyanoferrate – three-electrode cell

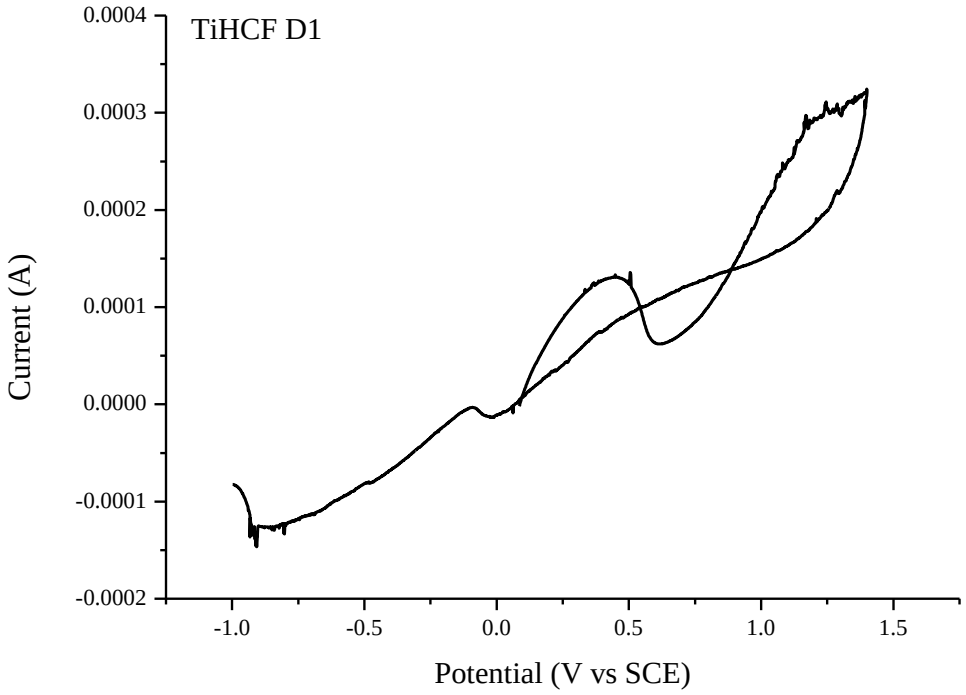

Figure 62: cyclic voltammetry scan for the sample D1 of the TiHCF series – three-electrode cell

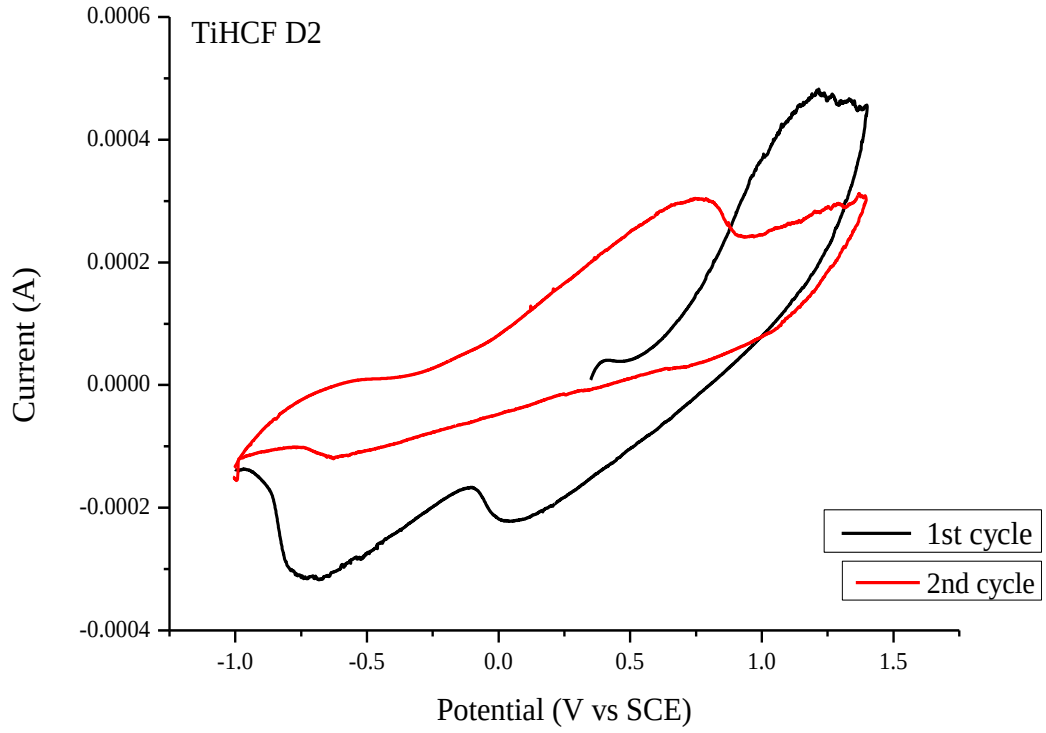

Figure 63: cyclic voltammetry scan for the sample D2 of the TiHCF series – three-electrode cell

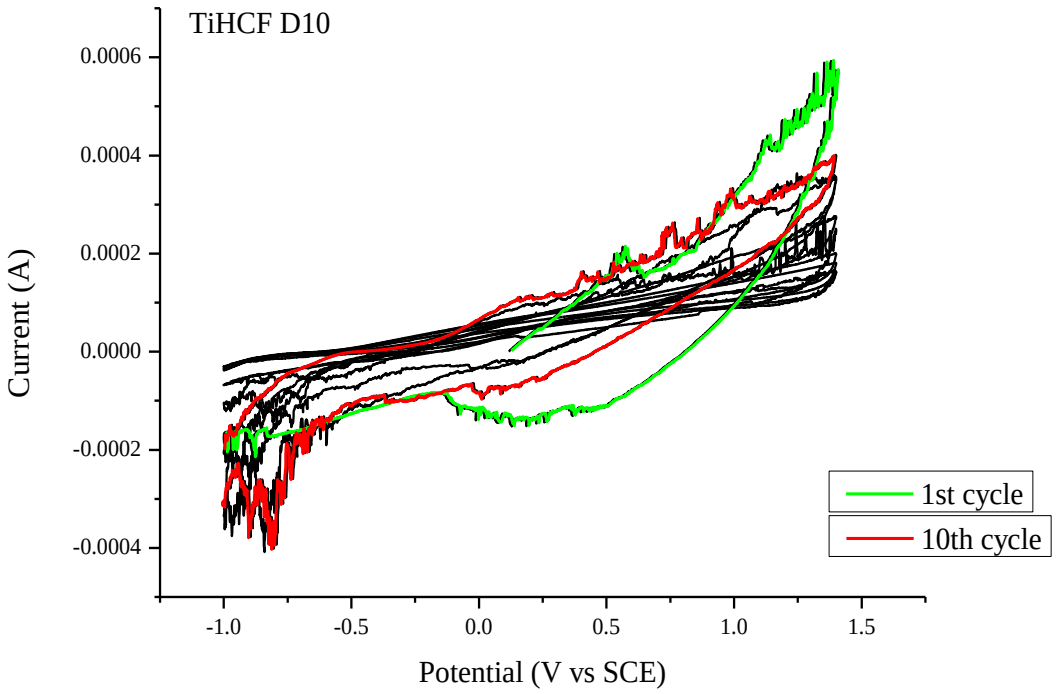

Figure 64: cyclic voltammetry scan for the sample D10 of the TiHCF series – three-electrode cell

5.2. X-Ray Photoelectron Spectroscopy

5.2.1. Manganese hexacyanoferrate – coin cell

5.2.1.1. XPS fitting of the detailed spectra in MnHCF series

5.2.1.1.1. XPS fitting of the detailed spectra of Fe 2p peaks

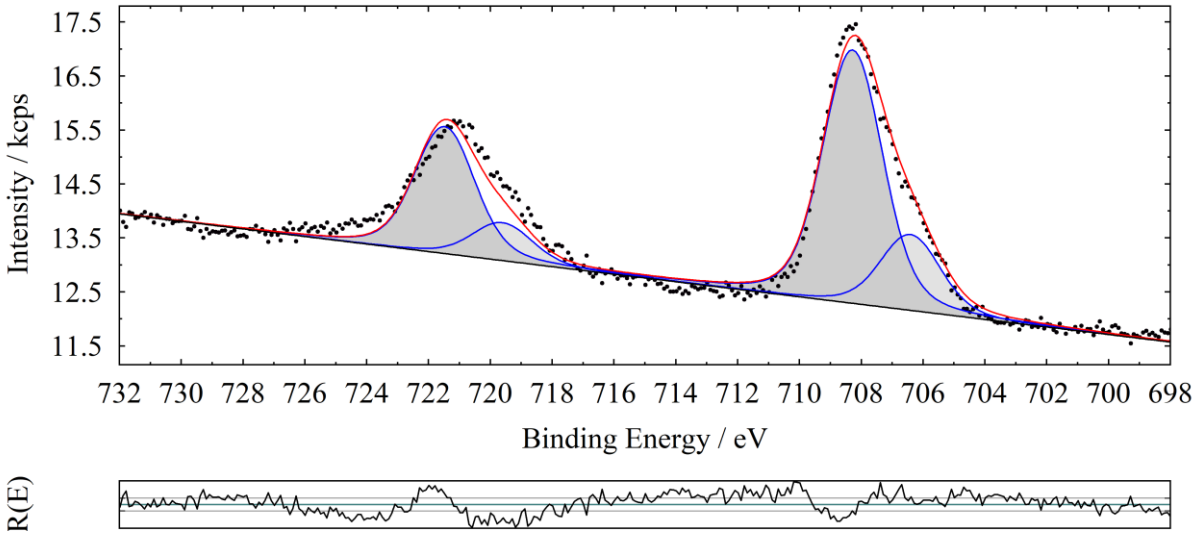

Figure 65: Fe 2p peaks of the pristine powder for the MnHCF series

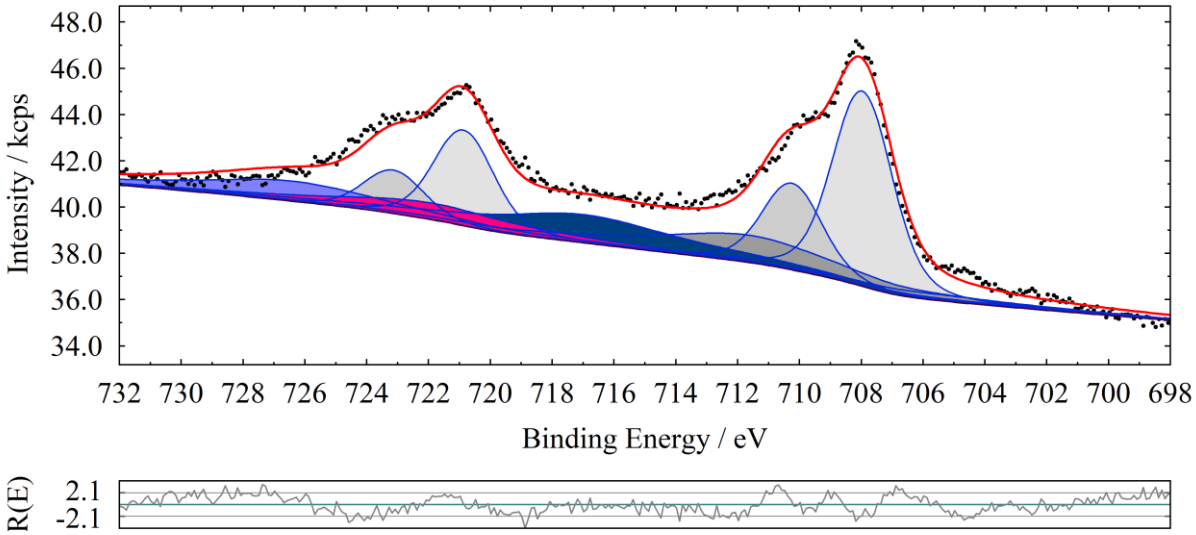

Figure 66: Fe 2p peaks of the C1 sample for the MnHCF series

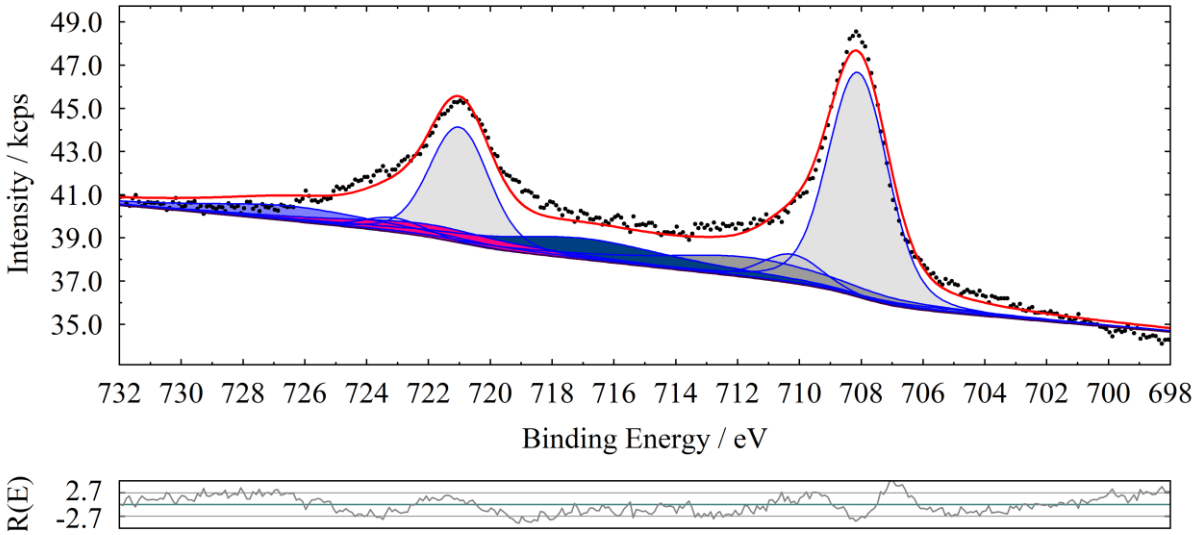

Figure 67: Fe 2p peaks of the D1 sample for the MnHCF series

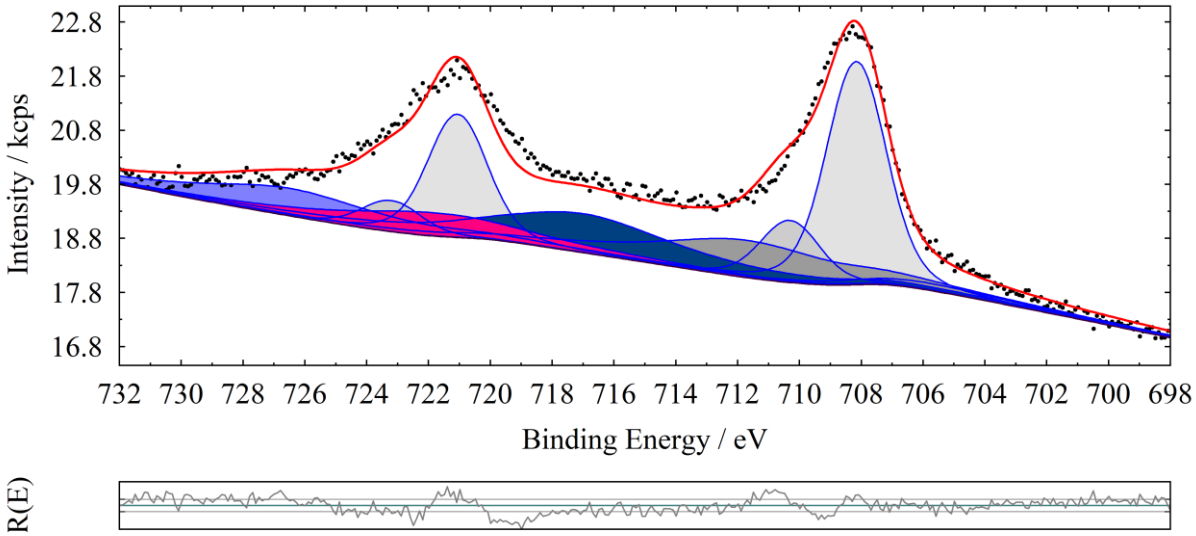

Figure 68: Fe 2p peaks of the D2 sample for the MnHCF series

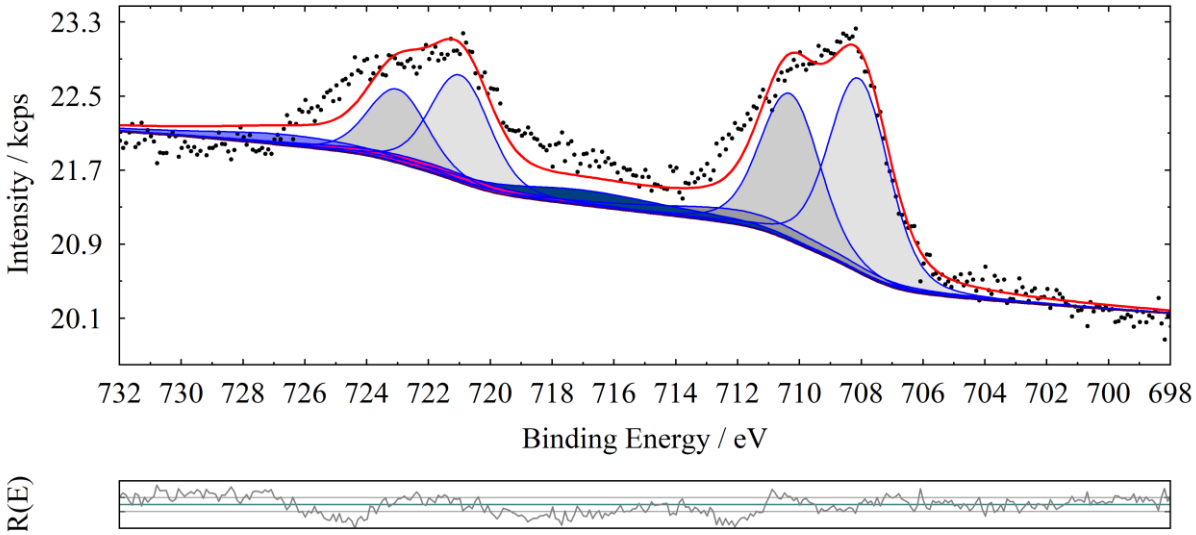

Figure 69: Fe 2p peaks of the C5 sample for the MnHCF series

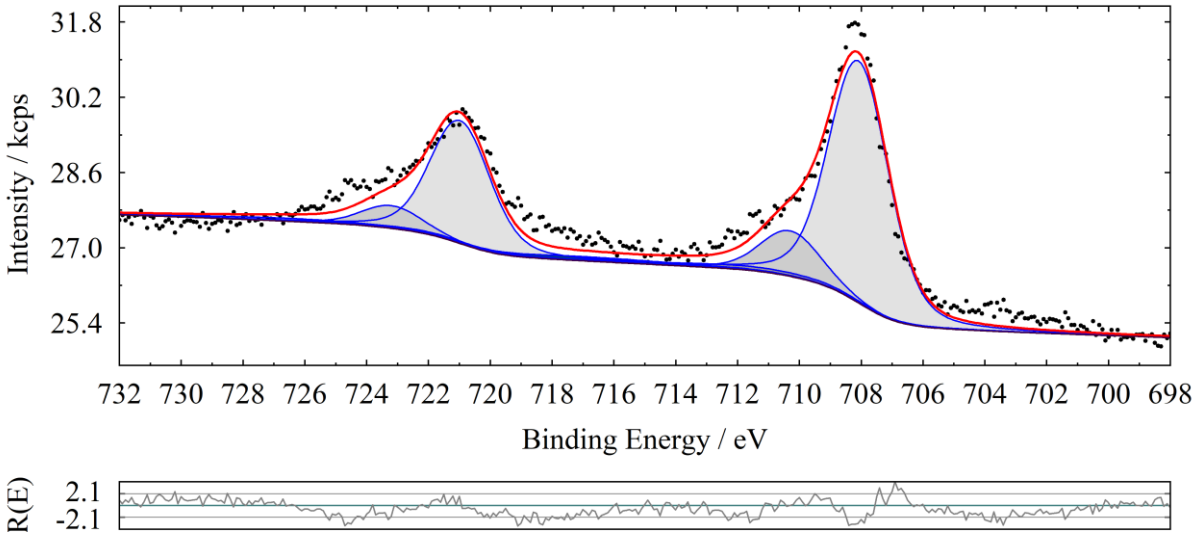

Figure 70: Fe 2p peaks of the D5 sample for the MnHCF series

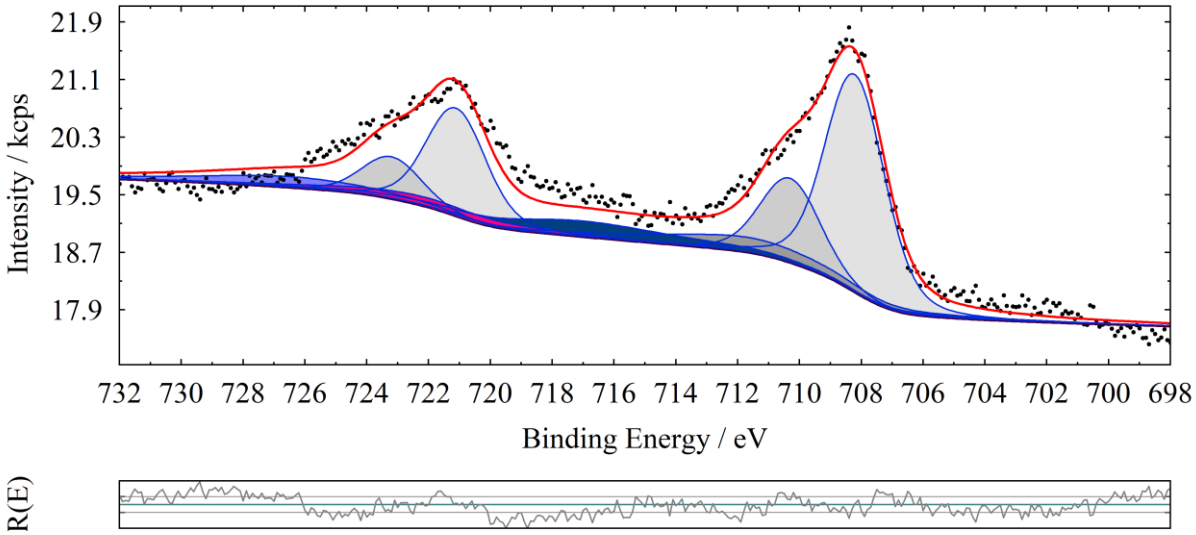

Figure 71: Fe 2p peaks of the C10 sample for the MnHCF series

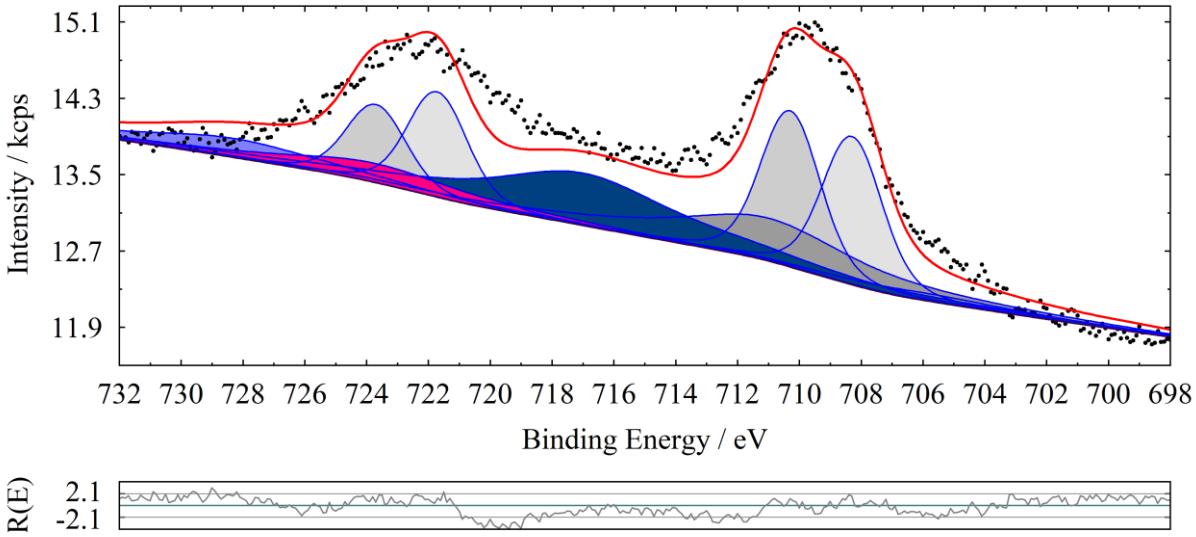

Figure 72: Fe 2p peaks of the D10 sample for the MnHCF series

5.2.1.1.2. XPS fitting of the detailed spectra of O 1s peak

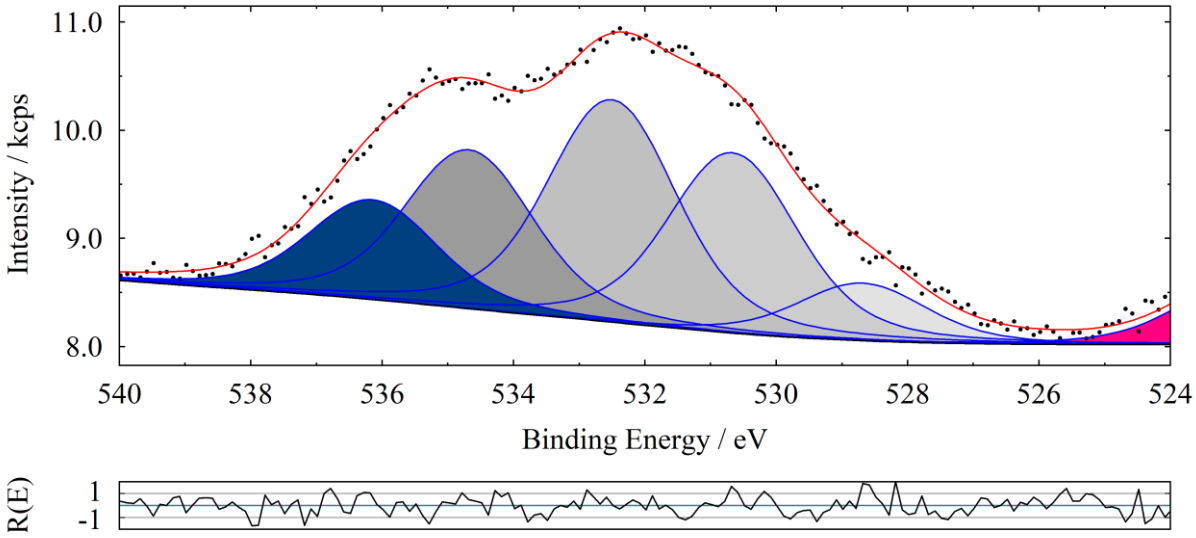

Figure 73: O 1s peaks of the pristine powder for the MnHCF series – coin cell

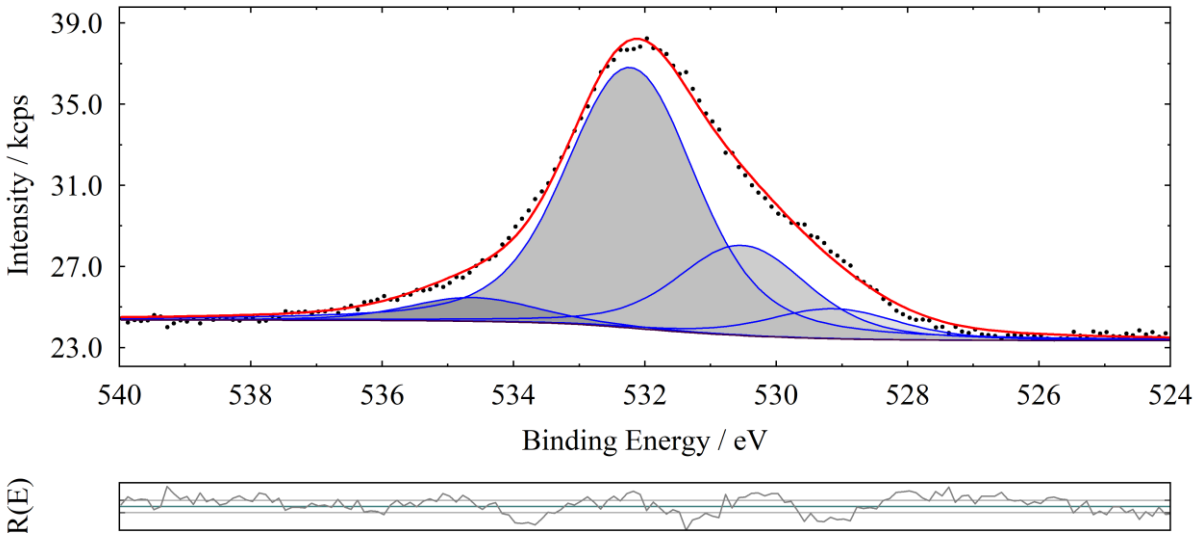

Figure 74: O 1s peaks of the C1 sample for the MnHCF series – coin cell

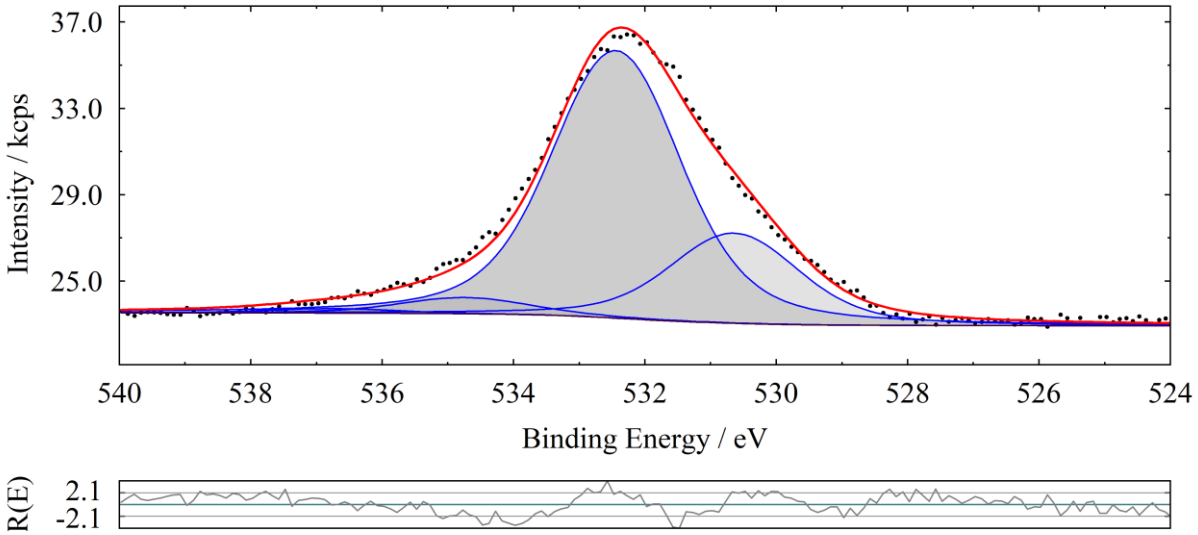

Figure 75: O 1s peaks of the D1 sample for the MnHCF series – coin cell

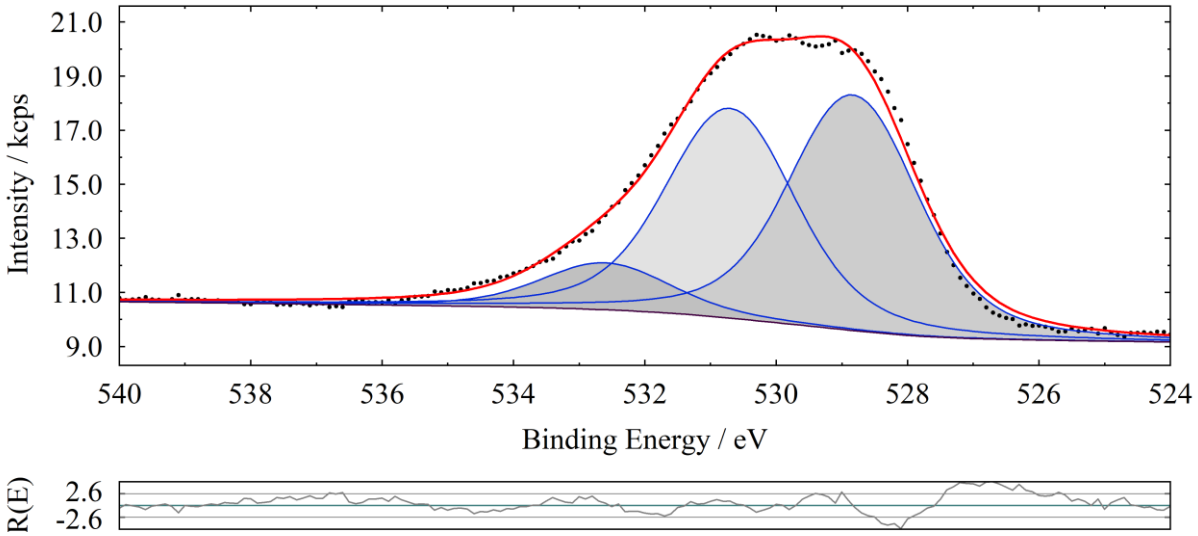

Figure 76: O 1s peaks of the C2 sample for the MnHCF series – coin cell

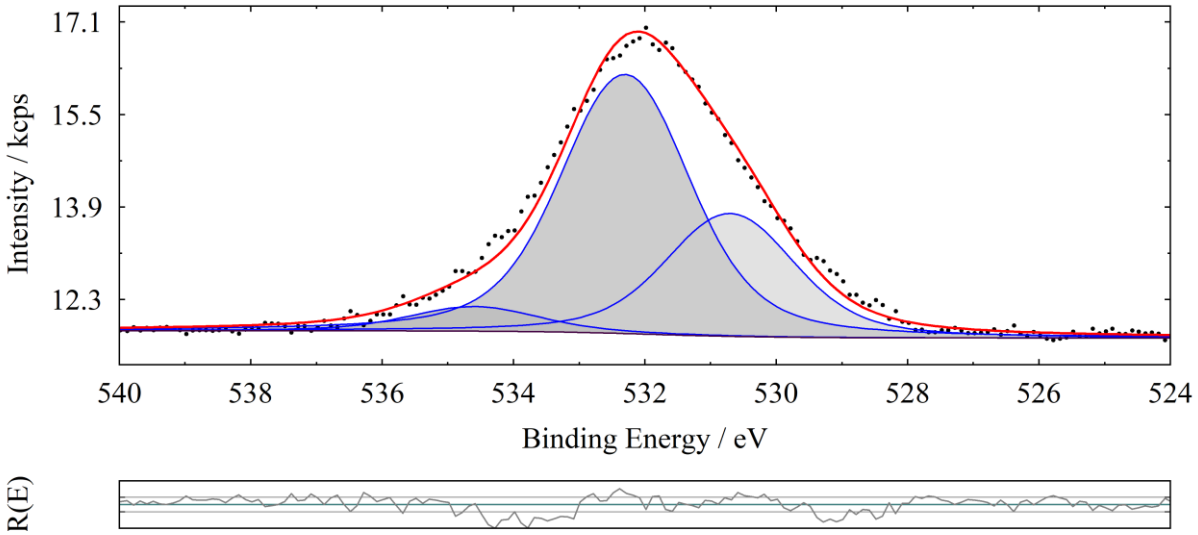

Figure 77: O 1s peaks of the D2 sample for the MnHCF series – coin cell

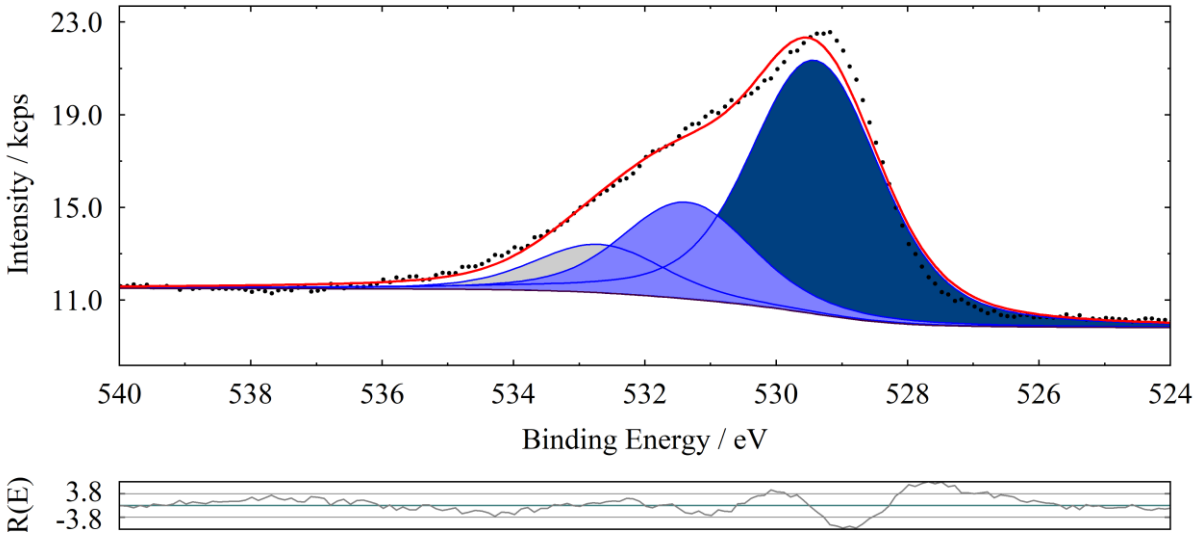

Figure 78: O 1s peaks of the C5 sample for the MnHCF series – coin cell

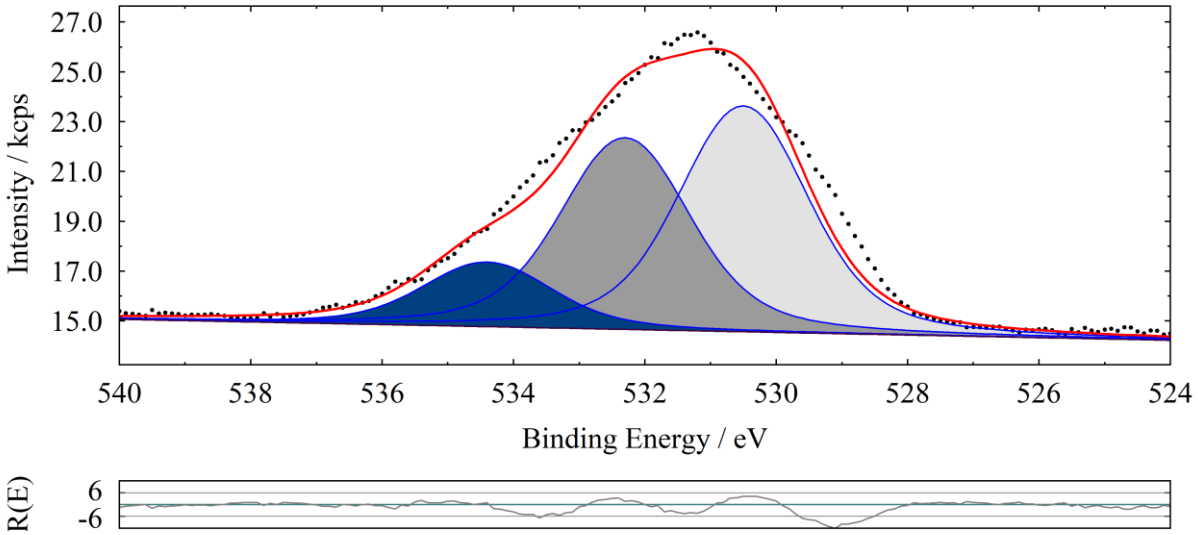

Figure 79: O 1s peaks of the D5 sample for the MnHCF series – coin cell

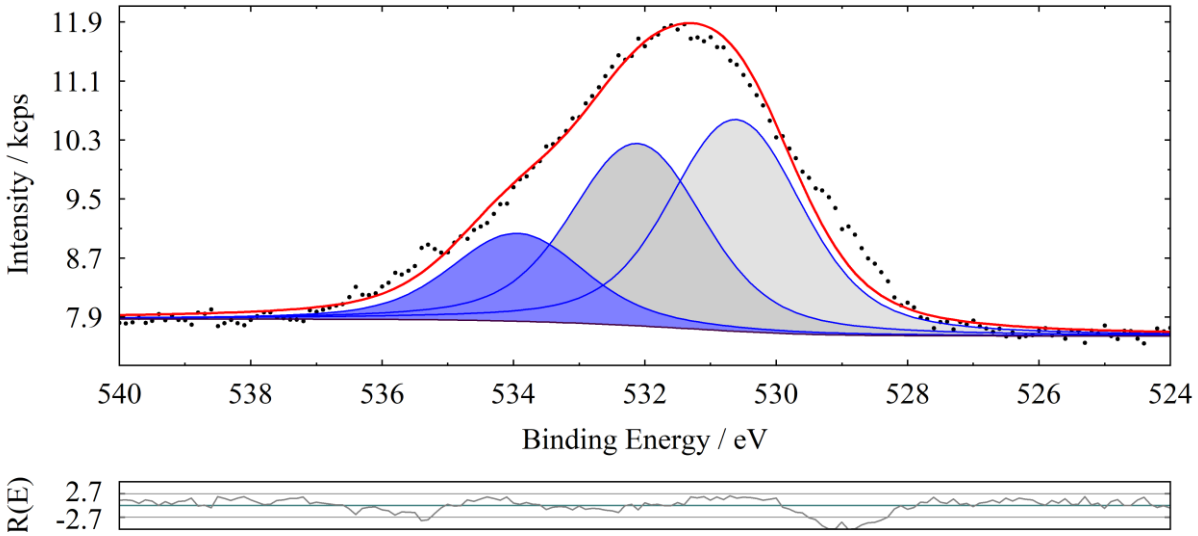

Figure 80: O 1s peaks of the D10 sample for the MnHCF series – coin cell

5.2.1.1.3. XPS fitting of the detailed spectra of Zn 2p peak

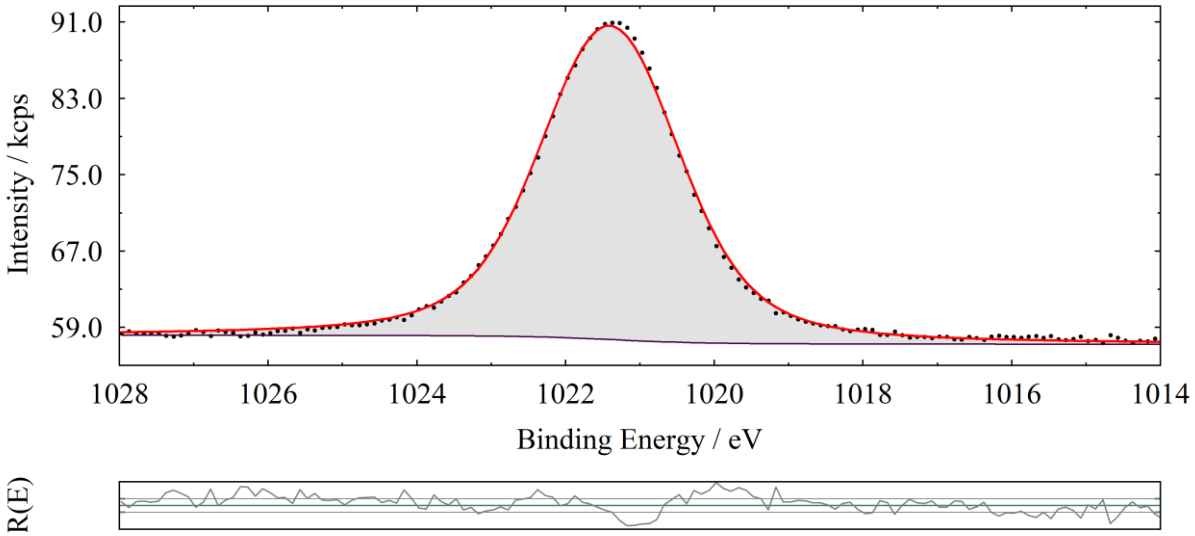

Figure 81: Zn 2p peaks of the C1 sample for the MnHCF series – coin cell

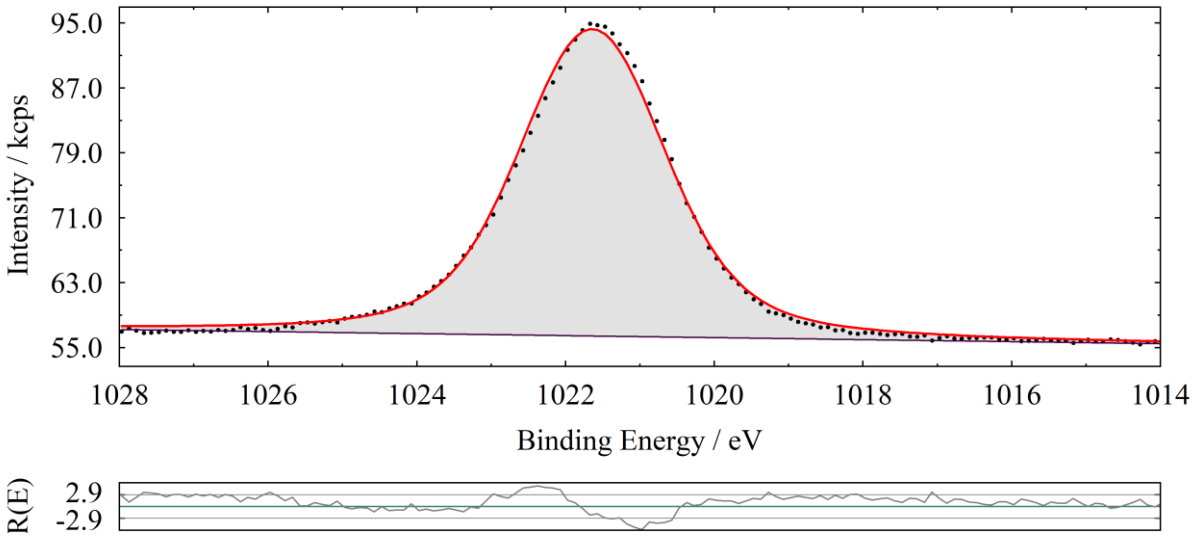

Figure 82: Zn 2p peaks of the D1 sample for the MnHCF series – coin cell

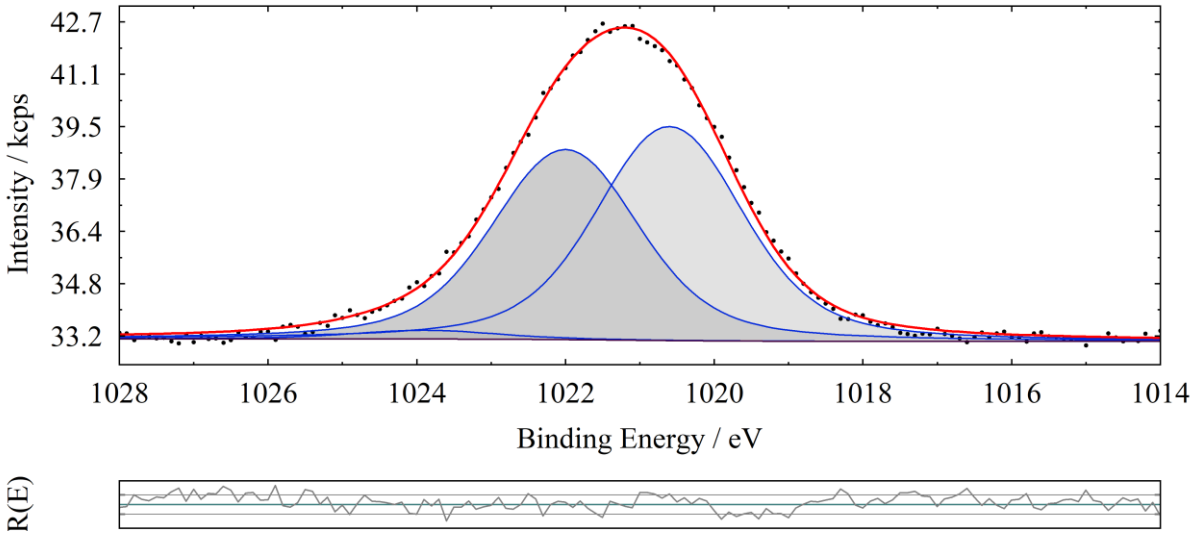

Figure 83: Zn 2p peaks of the C2 sample for the MnHCF series – coin cell

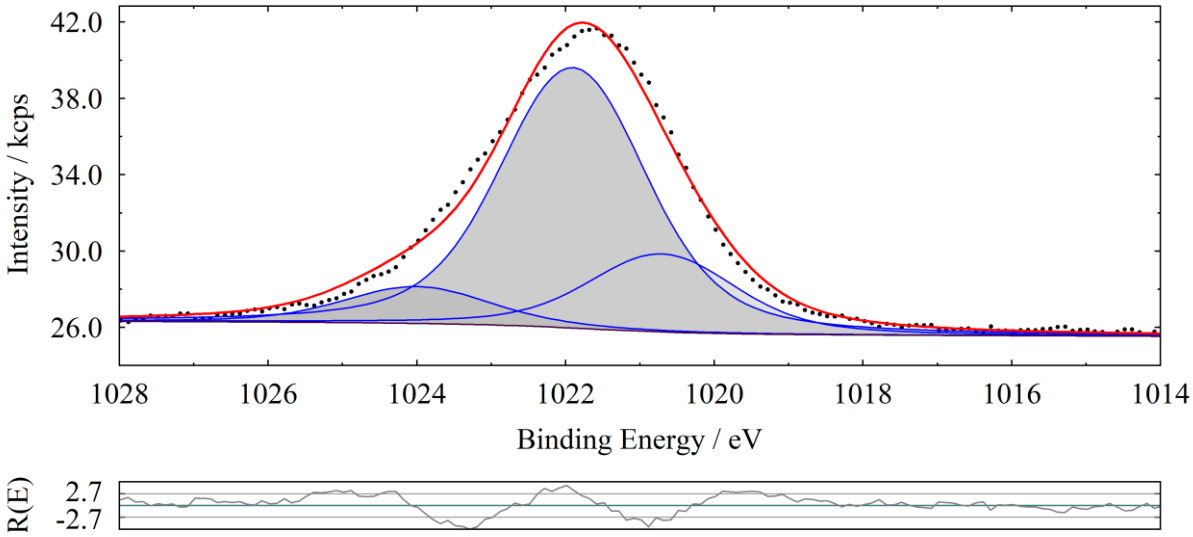

Figure 84: Zn 2p peaks of the D2 sample for the MnHCF series – coin cell

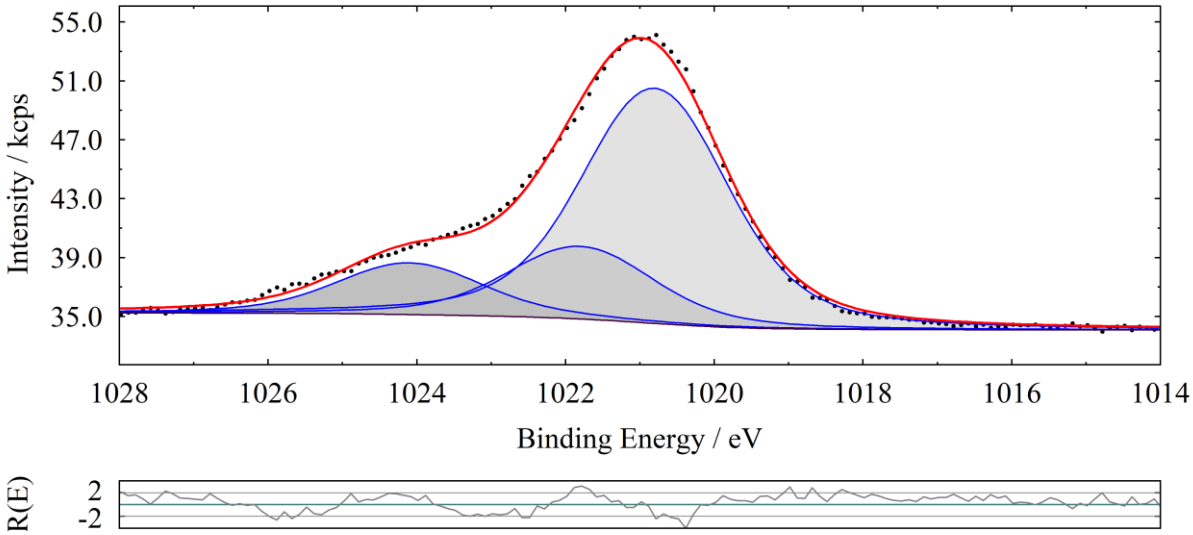

Figure 85: Zn 2p peaks of the C5 sample for the MnHCF series – coin cell

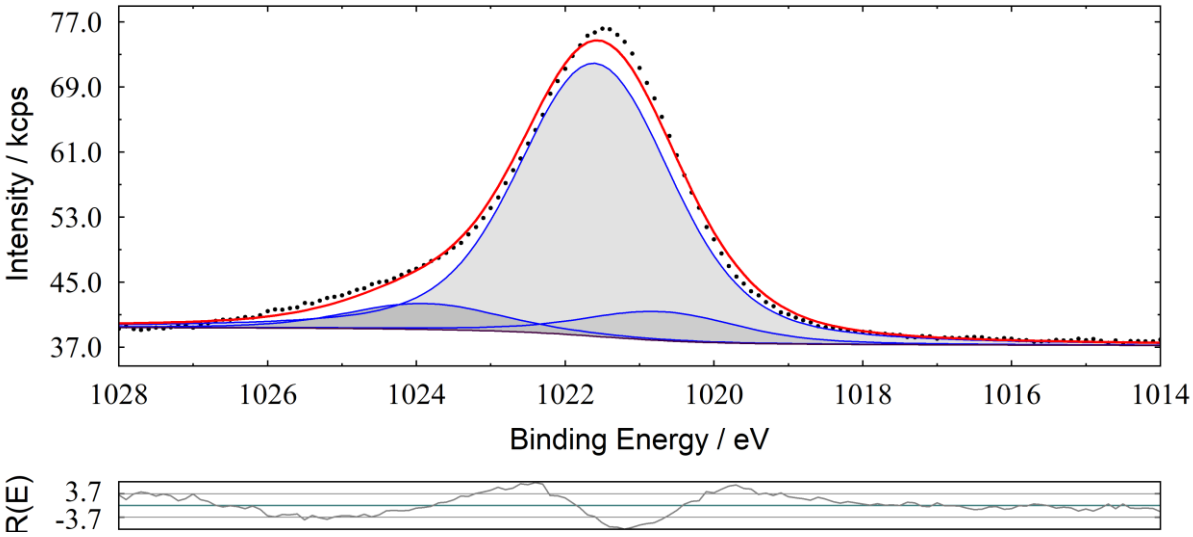

Figure 86: Zn 2p peaks of the D5 sample for the MnHCF series – coin cell

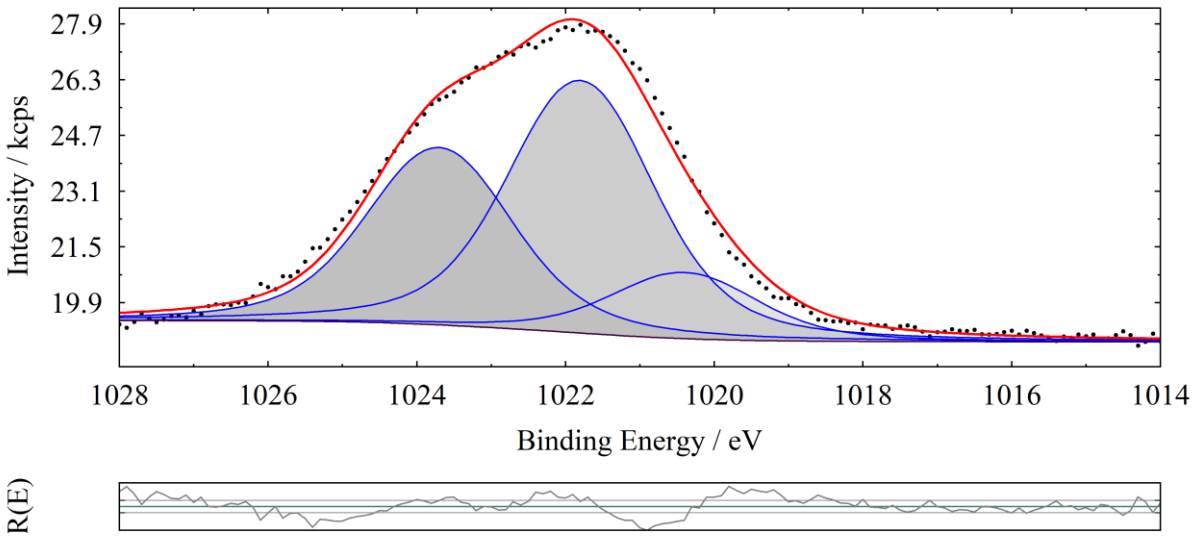

Figure 87: Zn 2p peaks of the D10 sample for the MnHCF series – coin cell

5.2.1.2. Binding energies and relative contribution to the respective orbital of the different elements

BINDING ENERGIES (eV)					
Sample	**N 1s**	**Na 1s**	**C 1s**	**O 1s**	**F 1s**
Pristine powder	395.8 (27.4%) 397.6 (71.8%) 400.9 (0.8%)	1071.6	282.3 (17.8%) 283.5 (28.9%) 284.7 (46.6%) 286.0 (5.4%) 288.1 (1.4%)	528.9 (12.5%) 530.7 (39.2%) 532.5 (48.4%)	-
Pristine pellet	397.6 (97.6%) 400.9 (2.4%)	1071.7	284.3 (66.6%) 285.6 (12.0%) 286.8 (9.2%) 288.1 (3.2%) 290.2 (0.8%) 291.2 (4.2%) 292.4 (4.0%)	530.7 (30.7%) 532.4 (69.3%)	688.99 (75.5%) 690.96 (15.4%) 692.71 (9.1%)
C1	397.6 (88.3%) 399.5 (10.7%) 400.9 (1.0%)	1071.72	284.0 (58.7%) 285.2 (18.7%) 286.4 (9.3%) 287.9 (3.5%) 289.8 (0.1%) 291.0 (6.3%) 292.4 (3.4%)	529.7 (9.7%) 530.7 (24.6%) 532.4 (65.7%)	688.64 (84.5%) 689.85 (11.7%) 691.15 (3.8%)
D1	397.6 (90.8%) 399.5 (7.6%) 400.9 (1.7%)	1072.03	284.1 (61.2%) 285.3 (16.8%) 286.5 (10.4%) 287.8 (3.6%) 291.0 (3.9%) 292.2 (4.1%)	530.7 (25.2%) 532.5 (74.8%)	688.73 (76.9%) 690.3 (16.1%) 691.99 (7.1%)
C2	397.6 (83.6%) 399.5 (16.4%)	-	283.1 (40.0%) 284.2 (22.2%) 285.4 (16.7%) 286.6 (3.8%) 287.9 (4.3%) 289.99 (4.0%) 291.2 (9.1%)	529.0 (47.8%) 530.7 (42.6%) 532.6 (9.5%)	688.0 (77.8%) 689.9 (15.6%) 691.0 (6.5%)

Table 15: binding energies and relative contribution (in at. %) to the respective orbital in parenthesis of the different elements (N, Na, C, O and F) for MnHCF series - coin cell

BINDING ENERGIES (eV)					
Sample	**N 1s**	**Na 1s**	**C 1s**	**O 1s**	**F 1s**
D2	397.6 (73.2%) 399.4 (23.1%) 400.9 (3.7%)	-	283.3 (19.0%) 284.0 (41.4%) 285.6 (18.7%) 286.8 (4.1%) 288.1 (3.3%) 290.2 (2.5%) 291.4 (10.2%) 292.6 (0.8%)	529.4 (63.7%) 530.6 (0.1%) 531.3 (21.7%) 532.5 (14.5%)	688.4 (88.0%) 690.4 (12.0%)
C5	397.6 (62.0%) 399.5 (27.0%) 400.9 (11.0%)	-	283.3 (12.2%) 284.3 (41.4%) 285.6 (20.6%) 286.8 (11.8%) 288.1 (7.0%) 290.2 (1.9%) 291.4 (5.3%)	530.5 (46.7%) 532.3 (39.8%) 534.4 (13.4%)	688.4 (92.1%) 690.2 (7.9%)
D5	397.6 (78.1%) 399.5 (17.1%) 400.9 (4.8%)	-	284.3 (45.0%) 285.5 (30.6%) 286.8 (15.2%) 288.1 (5.8%) 290.0 (1.8%) 291.2 (0.2%) 292.3 (1.5%)	529.3 (47.6%) 530.7 (33.7%) 532.2 (18.8%)	688.5 (46.2%) 689.2 (53.8%)
C10	397.6 (72.8%) 399.1 (21.2%) 400.9 (6.1%)	-	283.3 (10.8%) 284.1 (47.7%) 285.3 (20.9%) 286.5 (8.5%) 287.8 (4.7%) 289.9 (0.9%) 291.2 (6.5%)	528.8 (43.9%) 530.7 (37.9%) 532.2 (18.3%)	688.4 (9.7%) 690.5 (90.3%)
D10	395.8 (41.3%) 397.5 (47.8%) 399.1 (11.0%)	-	283.5 (19.9%) 284.1 (29.4%) 285.3 (16.9%) 286.5 (13.4%) 288.1 (5.8%) 289.9 (0.3%) 291.0 (9.3%) 292.2 (6.0%)	529.4 (63.7%) 530.6 (0.1%) 531.3 (21.7%) 532.5 (14.5%)	688.6 (6.2%) 690.4 (93.8%)

Table 16:binding energies and relative contribution (in at. %) to the respective orbital in parenthesis of the different elements (N, Na, C, O and F) for MnHCF series - coin cell

BINDING ENERGIES (eV)			
Sample	**Mn 3p**	**Fe 3p**	**Zn 2p**
Pristine powder	47.6	55.0	-
Pristine pellet	48.4	54.5	1022.0
C1	48.6	54.6	1021.5
D1	48.8	54.5	1021.7
C2	47.7	54.4	1020.6 (51.8%) 1022.0 (46.1%) 1023.9 (2.1%)
D2	-	54.5	1020.7 (20.8%) 1021.9 (69.4%) 1024.0 (9.8%)
C5	48.9	54.4	1020.8 (71.6%) 1022.3 (16.3%) 1024.1 (12.1%)
D5	49.0	54.6	1020.5 (3.6%) 1021.6 (88.7%) 1023.6 (7.8%)
C10	48.7	54.6	1020.7 (50.4%) 1021.8 (41.1%) 1024.0 (8.5%)
D10	-	55.3	1020.5 (16.9%) 1022.0 (49.8%) 1023.8 (34.1%)

Table 17: binding energies and relative contribution (in at. %) to the respective orbital in parenthesis of the metals (Mn, Fe and Zn) for MnHCF series – coin cell

ATOMIC PERCENTAGES							
Sample	**N**	**Na**	**C**	**O**	**Mn**	**Fe**	**F**
Pristine powder	23.3	6.7	57.5	4.7	3.9	3.9	-
Pristine pellet	8.1	2.4	64.5	4.9	1.2	1.5	17
C1	10	0.5	60.5	9.3	0.4	1.7	14.6
D1	10.4	0.7	58.3	9.3	0.1	1.8	15.4
C2	6.1	-	45.9	24	2.5	1.7	16.6
D2	9.7	-	59.1	7.3	-	1.5	19.7
C5	10.8	-	39.3	30.9	4.3	1.5	7.6
D5	15.4	-	38.1	26.2	1.6	2.9	4.2
C10	11.2	-	42.5	25.3	2.9	2.1	10.3
D10	8.3	-	55.3	10.1	-	1.6	20

Table 18: atomic percentages of the different elements for MnHCF series – coin cell

5.2.2. Titanium hexacyanoferrate – three-electrode cell

5.2.2.1. XPS fitting of the detailed spectra of the TiHCF series

5.2.2.1.1. XPS fitting of the detailed spectra of Ti 2p peaks

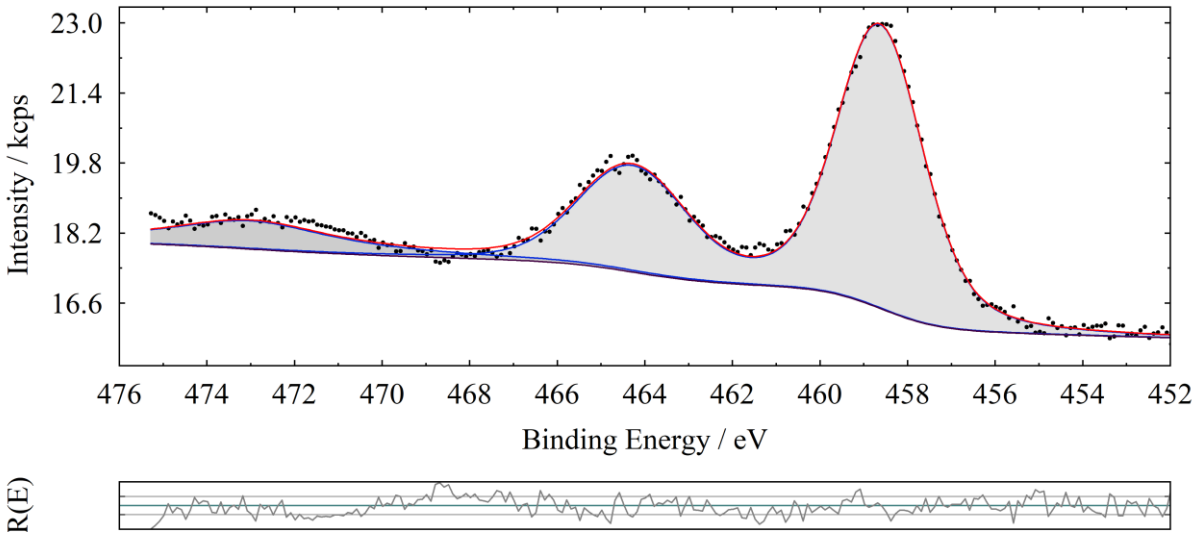

Figure 88: Ti 2p peaks of the pristine pellet for the TiHCF series – three-electrode cell

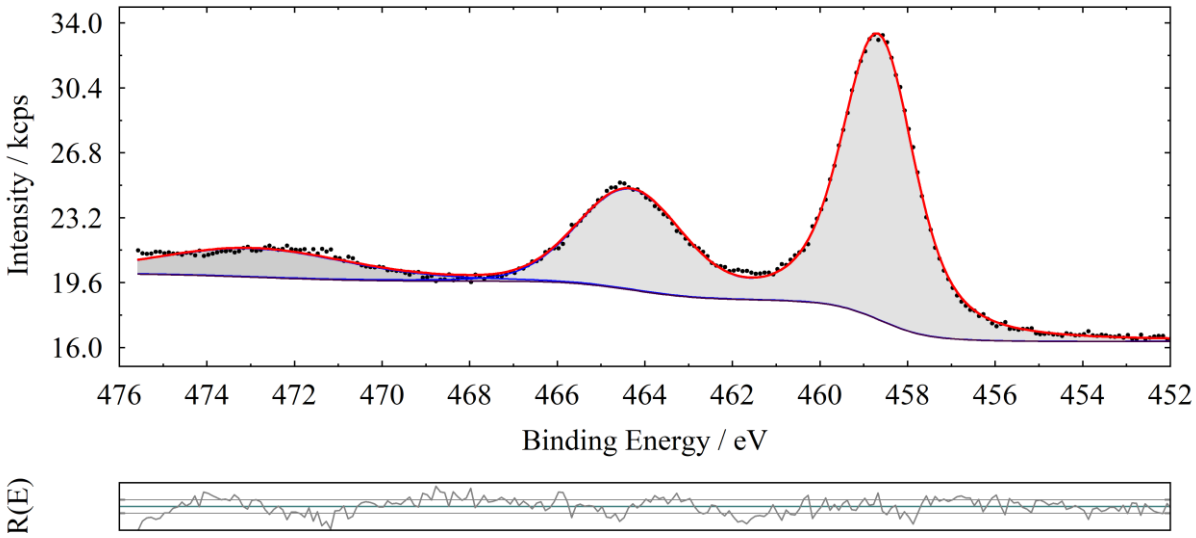

Figure 89: Ti 2p peaks of the C1 sample for the TiHCF series – three-electrode cell

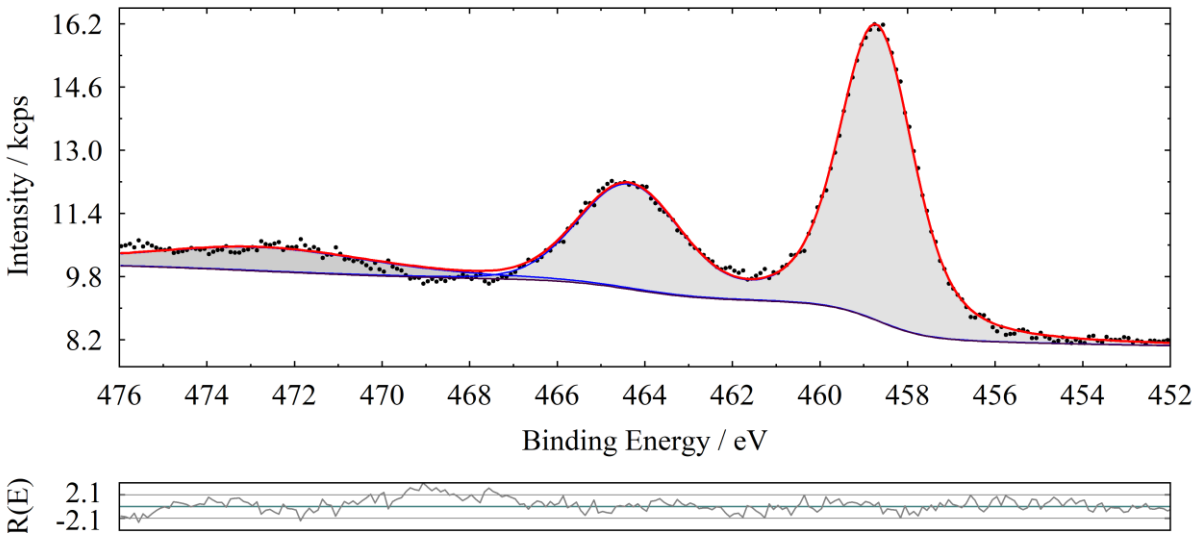

Figure 90: Ti 2p peaks of the D1 sample for the TiHCF series – three-electrode cell

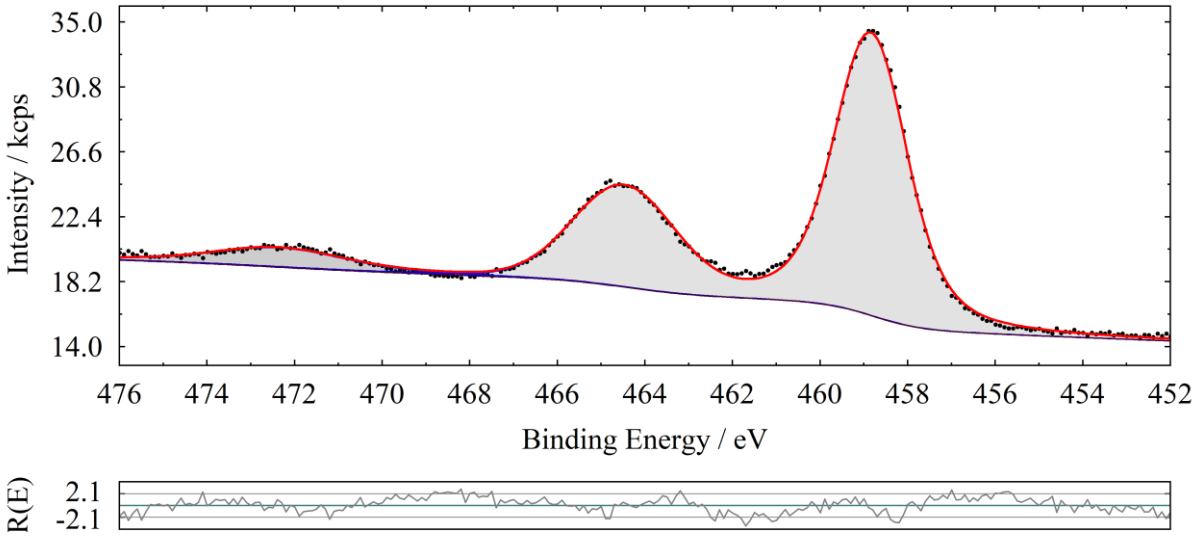

Figure 91: Ti 2p peaks of the D2 sample for the TiHCF series – three-electrode cell

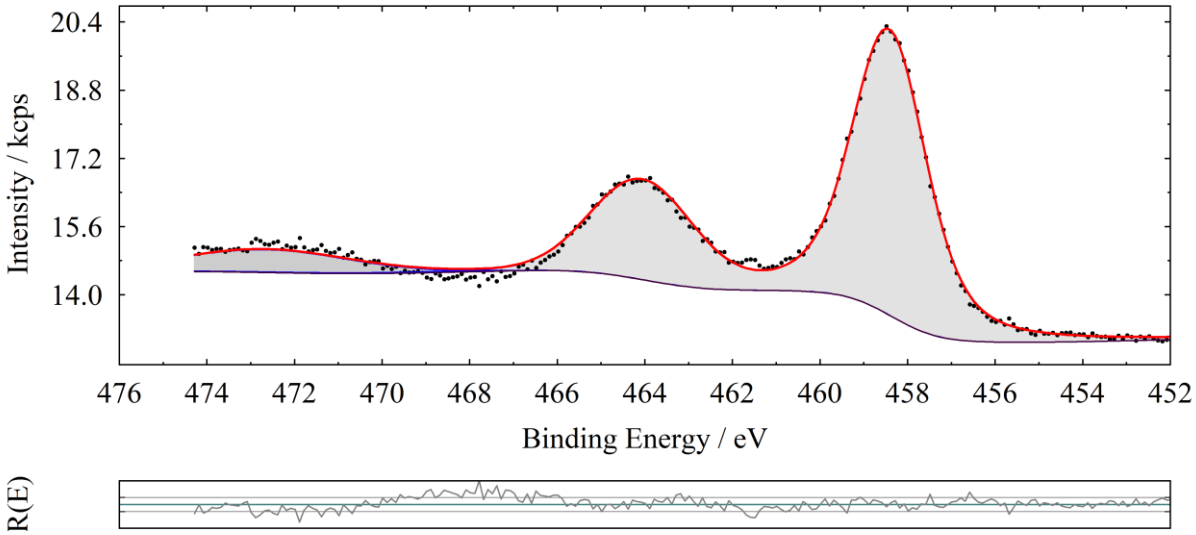

Figure 92: Ti 2p peaks of the D10 sample for the TiHCF series – three-electrode cell

5.2.2.1.2. XPS fitting of the detailed spectra of O 1s peak

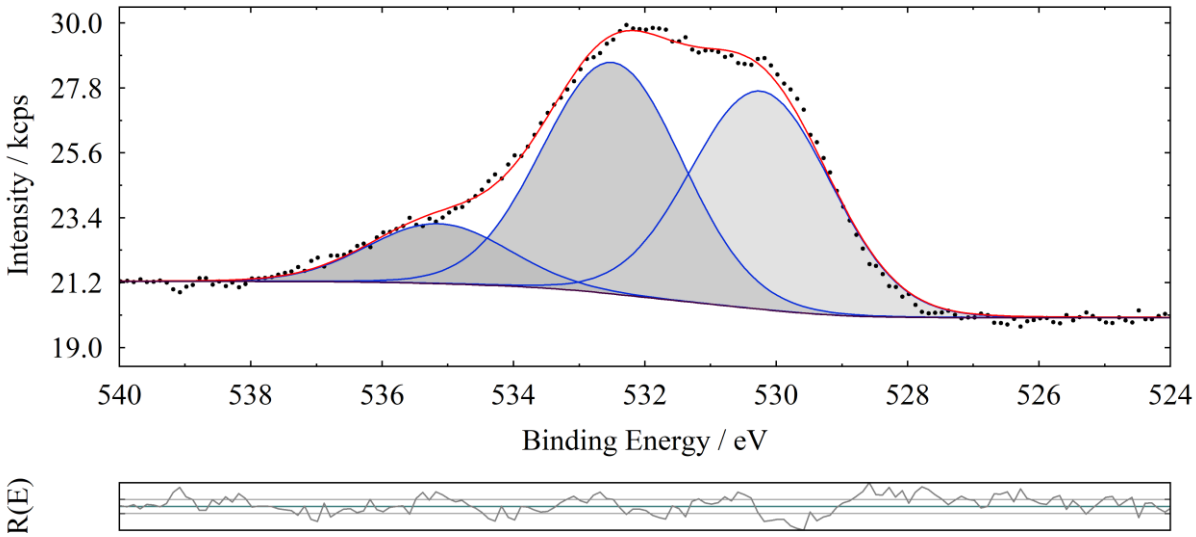

Figure 93: O 1s peak of the pristine pellet for the TiHCF series – three-electrode cell

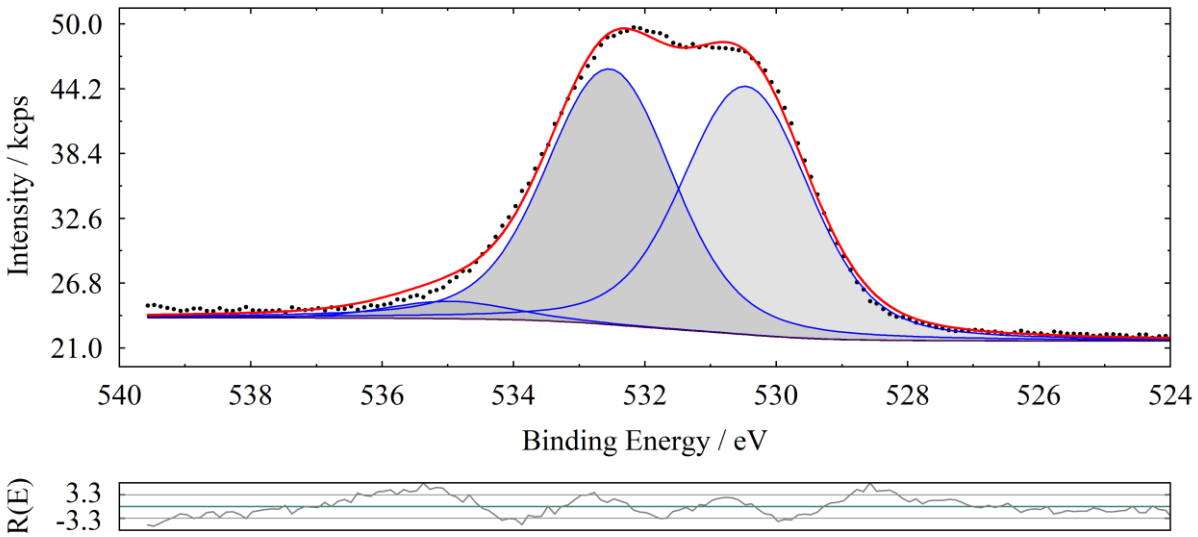

Figure 94: O 1s peak of the C1 sample for the TiHCF series – three-electrode cell

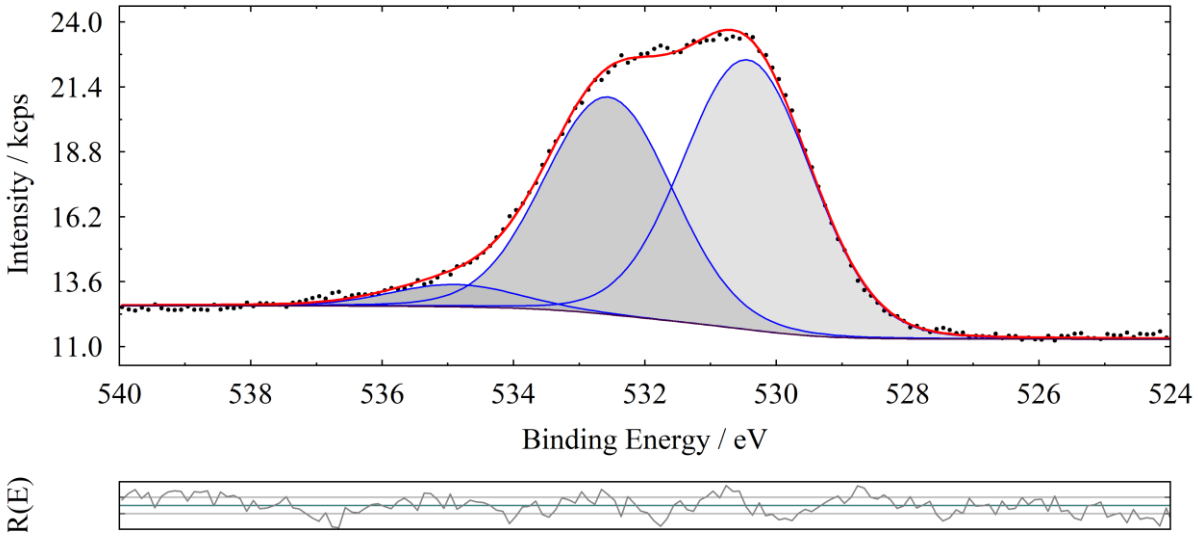

Figure 95: O 1s peak of the D1 sample for the TiHCF series – three-electrode cell

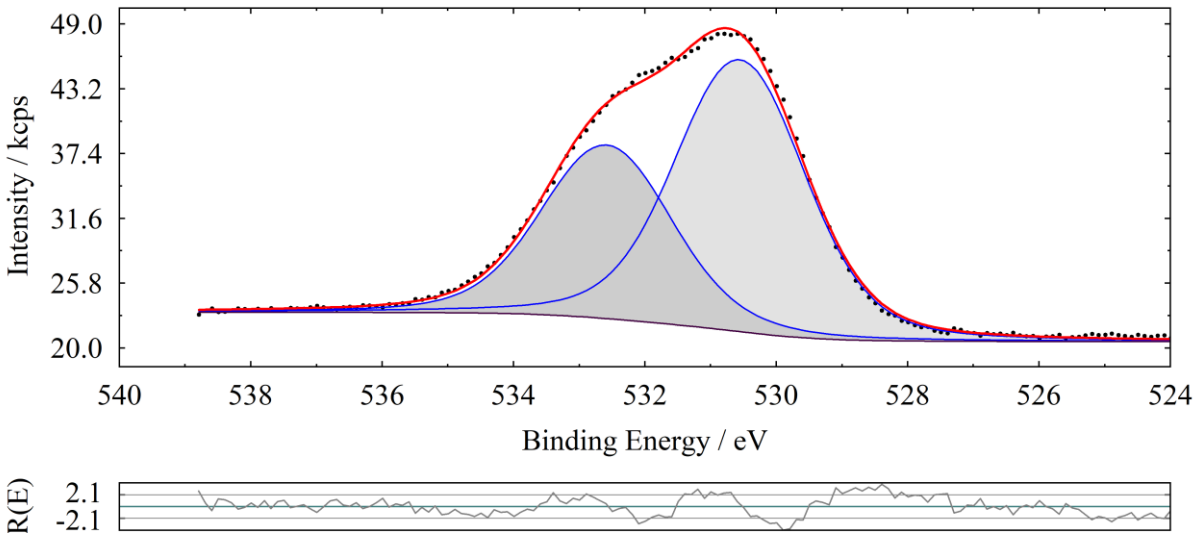

Figure 96: O 1s peak of the D2 sample for the TiHCF series – three-electrode cell

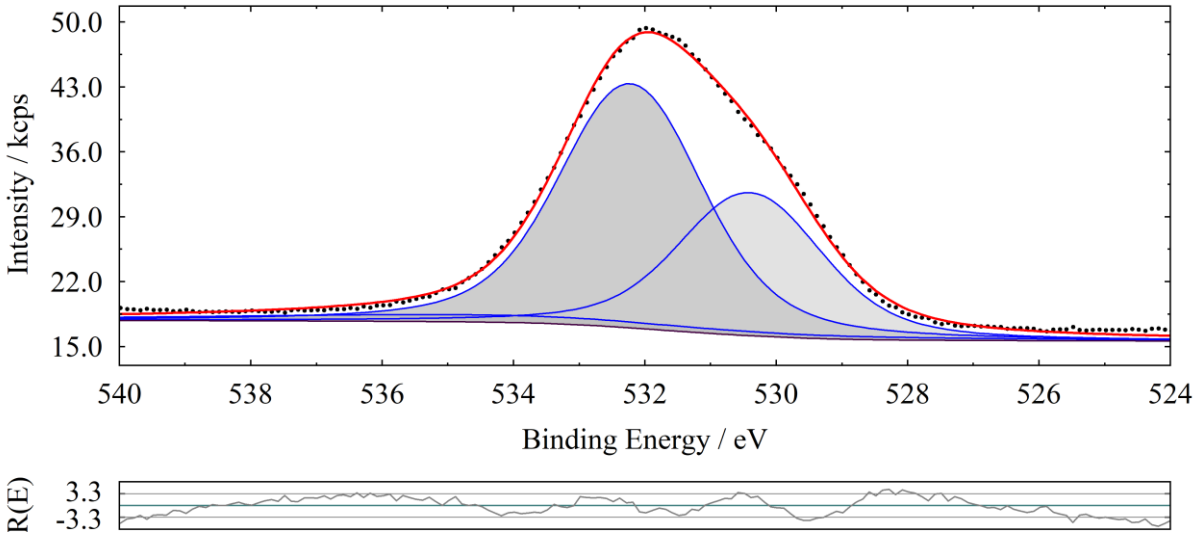

Figure 97: O 1s peak of the D10 sample for the TiHCF series – three-electrode cell

5.2.2.2. Binding energies and relative contribution to the respective orbital of the different elements

BINDING ENERGIES (eV)					
Sample	**N 1s**	**Na 1s**	**C 1s**	**O 1s**	**F 1s**
Pristine powder	397.6 (90.7%) 399.7 (3.7%) 402.2 (5.6%)	1071.8	284.6 (93.2%) 286.4 (3.5%) 288.2 (3.4%)	530.4 (45.7%) 532.4 (54.3%)	
Pristine pellet	397.6 (85.6%) 399.4 (8.6%) 401.9 (5.8%)	1071.7	284.5 (65.7%) 286.4 (11.3%) 288.6 (3.6%) 291.7 (16.7%) 293.0 (2.7%)	530.2 (48.6%) 532.5 (51.4%)	684.6 (0.8%) 689.0 (90.9%) 691.7 (8.3%)
C1	397.6 (70.6%) 399.7 (21.1%) 401.5 (8.4%)	-	284.4 (64.5%) 286.2 (20.0%) 288.7 (4.2%) 291.7 (9.2%) 292.6 (2.1%)	530.5 (49.6%) 532.6 (50.4%)	684.1 (1.3%) 689.0 (82.4%) 690.0 (16.3%)
D1	397.6 (75.0%) 399.9 (13.5%) 402.0 (6.8%)	1072.0	284.4 (69.7%) 286.4 (14.3%) 288.65 (4.7%) 291.6 (10.0%) 292.9 (1.2%)	530.5 (53.6 %) 532.5 (44.8%)	684.6 (2.2%) 688.9 (88.7%) 690.6 (9.1%)
D2	397.6 (68.2%) 399.9 (23.4%) 401.7 (8.4%)	1071.9	284.5 (61.7%) 286.4 (17.3%) 288.9 (4.3%) 291.7 (13.0%) 292.5 (3.7%)	530.6 (61.0%) 532.6 (39.0%)	684.5 (1.5%) 689.0 (89.9%) 690.6 (8.6%)
D10	397.6 (48.9%) 399.9 (46.2%) 401.6 (4.9%)	1071.5	284.3 (63.2%) 286.1 (23.2%) 288.3 (9.8%) 291.3 (10.1%) 292.1 (3.7%)	530.4 (36.9%) 532.2 (63.1%)	684.9 (3.9%) 688.6 (88.6%) 690.8 (7.5%)

Table 19: binding energies and relative contribution (in at. %) to the respective orbital in parenthesis of the different elements (N, Na, C, O and F) for TiHCF series – three-electrode cell

BINDING ENERGIES (eV)			
Sample	**Ti 2p**	**Fe 3p**	**Zn 2p**
Pristine powder	458.7	54.7	
Pristine pellet	458.6	54.8	1021.9
C1	458.7	54.9	1021.6
D1	458.7	54.8	1021.8
D2	458.8	54.8	1021.7
D10	458.4	55.2	1021.6

Table 20: binding energies of the metals (Ti, Fe and Zn) for TiHCF series – three-electrode cell

ATOMIC PERCENTAGES									
Sample	**N**	**Na**	**C**	**O**	**Ti**	**Fe**	**F**	**Zn**	**Al**
Pristine powder	23.9	3.8	49.5	11.9	3.9	4.5	-	-	-
Pristine pellet	8.0	1.2	54.9	6.1	1.4	1.7	26.6	0.1	-
C1	3.3	-	58.5	18	3.0	1.4	15.8	-	-
D1	5.5	2.4	55	16.9	2.7	1.6	15.7	0.3	-
D2	4.6	1.2	52	17.3	3.7	1.4	19.7	0.1	-
D10	4.5	0.9	49.1	22.7	1.5	1.6	16.5	0.2	3.2

Table 21: atomic percentages of the different elements for TiHCF series – three-electrode cell

5.2.3. Titanium hexacyanoferrate – symmetric coin cell

5.2.3.1. Binding energies and relative contribution to the respective orbital of the different elements

BINDING ENERGIES (eV)					
Sample	**N 1s**	**Na 1s**	**C 1s**	**O 1s**	**F 1s**
Pristine powder	397.6 (90.7%) 399.7 (3.7%) 402.2 (5.6%)	1071.8	284.6 (93.2%) 286.4 (3.5%) 288.2 (3.4%)	530.4 (45.7%) 532.4 (54.3%)	-
Pristine pellet	397.6 (85.6%) 399.4 (8.6%) 401.9 (5.8%)	1071.7	284.5 (65.7%) 286.4 (11.3%) 288.6 (3.6%) 291.7 (16.7%) 293.0 (2.7%)	530.2 (48.6%) 532.5 (51.4%)	684.6 (0.8%) 689.0 (91.0%) 691.7 (8.2%)
C1 - A	397.6 (83.1%) 399.8 (9.8%) 401.9 (7.1%)	1071.7	284.5 (63.5%) 286.7 (17.7%) 288.9 (4.6%) 292.1 (13.0%) 293.4 (1.3%)	530.4 (30.0%) 532.6 (70.0%)	684.4 (0.9%) 689.2 (86.3%) 690.9 (12.8%)
C1 - C	397.6 (80.9%) 399.8 (11.5%) 401.9 (7.6%)	1071.8	284.4 (58.1%) 286.4 (21.1%) 289.0 (4.3%) 292.1 (14.8%) 293.3 (1.7%)	530.4 (36.1%) 532.4 (63.9%)	684.4 (0.8%) 689.2 (80.8%) 690.9 (18.3%)
D1 - A	397.6 (78.8%) 399.7 (13.8%) 402.0 (7.4%)	1071.8	284.5 (61.2%) 286.5 (18.7%) 289.0 (5.1%) 292.2 (14.0%) 293.4 (1.1%)	530.6 (30.5%) 532.7 (54.3%) 535.8 (15.2%)	684.4 (0.9%) 689.3 (86.4%) 691.5 (12.7%)
D1 - C	397.6 (80.2%) 399.6 (11.7%) 402.2 (8.2%)	1071.6	284.5 (60.1%) 286.4 (19.4%) 289.0 (4.9%) 292.2 (15.5%) 293.4 (0.1%)	530.4 (32.9%) 532.7 (59.8%) 535.6 (7.4%)	689.3 (92.3%) 691.5(7.7%)

Table 22: binding energies and relative contribution (in at. %) to the respective orbital in parenthesis of the different elements (N, Na, C, O and F) for TiHCF series - symmetric coin cell

BINDING ENERGIES (eV)			
Sample	**Ti 2p**	**Fe 3p**	**Zn 2p**
Pristine powder	458.7	54.7	-
Pristine pellet	458.7	54.8	0.1
C1 - A	458.6	55.1	0.3
C1 - C	458.6	55	0.2
D1 - A	458.7	55	0.1
D1 - C	458.6	55	0.1

Table 23: binding energies of the different metals (Ti, Fe and Zn) for TiHCF series - symmetric coin cell

ATOMIC PERCENTAGES								
	N	**Na**	**C**	**O**	**Ti**	**Fe**	**F**	**Zn**
Pristine powder	23.9	3.8	49.5	11.9	3.9	4.5	-	-
Pristine pellet	8.0	1.2	54.9	6.1	1.4	1.7	26.6	0.1
C1 - A	6.7	0.8	57.8	11	1.2	1.6	20.7	0.3
C1 - C	6.3	0.7	56.1	8.9	1.2	1.5	25.2	0.2
D1 - A	7.4	0.5	56.8	9.3	1.1	1.7	23.1	0.1
D1 - C	7.4	1.0	56.4	10.1	1.3	1.7	22.2	0.1

Table 24: atomic percentages of the different elements for TiHCF series - symmetric coin cell

6. BIBLIOGRAPHY

1. Bellis M., (2008) *"Biography of Alessandro Volta – Stored Electricity and the First Battery".*

2. Crompton T. R., (2000) "*Battery Reference Book"* (third ed.).

3. Tarascon, J. M., & Armand, M. (2001). *"Issues and challenges facing rechargeable lithium batteries"*, Nature, 414(6861), 359–67.

4. K. C. Kam, M. M. Doeff. *"Electrode Materials for Lithium-Ion Batteries",* Material Matters, 2012, 7, 4.

5. Li M., (2018), *"Synthesis, Characterisation and Electrochemical study of Titanium Hexacyanoferrate Electrode material",* unpublished master's thesis, University of Bologna.

6. Hwang J. Y., Myung S. T., Sun Y. K., (2017) *"Sodium-ion batteries: present and future",* New Journal of Chemistry, 44 (5), 1678.

7. Lin M., Schroeder M. A., Borodin O., Pollard T. P., Ding M. S., Wang C., Xu K., (2020*) "Realizing high zinc reversibility in rechargeable batteries"*, Nature Energy, 5 (10): 743-749.

8. Zhu Y., Cui Y., N. Alshareef H., (2021) *"An Anode-Free Zn-MnO_2 Battery",* Nano Letters, 21, 1446-1453.

9. World Health Organization, (October 2013) *"WHO Model List of Essential Medicines"*.

10. Kjeldgaard S., Dugulan I., Mamakhel A., Wagemaker M., Brummerstedt Iversen B., Bentien A., (2021) "*Strategies for sunthesis of Prussian blue analogues"*, R. Soc. Open Sci. 8: 201779.

11. Herren F., Fischer P., Ludi A., Haelg W., (1980) *"Neutron diffraction study of Prussian Blue, $Fe_4[Fe(CN)_6]_3 x H_2O$. Location of water molecules and long-range magnetic order",* Inorganic Chemistry 19.

12. Lee H. W., Wang R. Y., Pasta M., Lee S. W., Liu N., Cui Y., (2014) *"Manganese hexacyanomanganate open framework as a high-capacity positive electrode material for sodium-ion batteries"* Nature Communication.

13. Ware M., (2008) *"Prussian Blue: Artists', Pigment and Chemists' Sponge",* Journal of Chemical Education, vol. 85, n. 5, p. 612.

14. Mullaliu A., Asenbauer J., Aquilanti G., Passerini S., Giorgetti M., (2019) *"Highlight the Reversible Manganese Electroactivity in Na-Rich Manganese Hexacyanoferrate Material for Li- and Na-Ion Storage",* Small Methods.

15. Li M., Mullaliu A., Passerini S., Giorgetti M., (2021), *"Titanium Activation in Prussian Blue Based Electrodes for Na-Ion Batteries: A Synthesis and Electrochemical Study",* Batteries, 7, 5.

16. Sun X., Ji X. Y., Zhou Y. T., Shao Y., Zang Y., Wen Z. Y., Chen C. H., (2016) *"A new gridding cyanoferrate anode material for lithium and sodium-ion batteries:* $Ti_{0.75}Fe_{0.25}[Fe(CN)_6]_{0.96} \cdot 1.9H_2O$ *with excellent electrochemical properties",* Journal of Power Sources.

17. Petrucci R. H., Herring F. G., e al, (2018) *"Chimica Generale: Principi ed applicazioni moderne",* 10° edizione, Piccin Editore.

18. Nicholson R. S., (1965) *"Theory and application of Cyclic Voltammetry for Measurements of Electrode Reaction Kinetics",* Analytical Chemistry, 37, 11, 1351-1355.

19. Elgrishi N., Rountree K. J., McCarthy B. D., Rountree E. S., Eisenhart T. T., Dempsey J. L., (2017), *"A Practical Beginner's Guide to Cyclic Voltammetry",* American Chemical Society and Division of Chemical Education, Inc.

20. A. J. Bard and L. R. Faulkner, (2001) "*Electrochemical methods"*, Second Edition Wiley.

21. Hercules D. M., Hercules S. H., *"Analytical Chemistry of Surfaces"*, Journal of Chemical Education, pp. 402-409.

22. Moulder J. F., Stickle W. F., Sobol P. E., Bomben K. D., (1992) *"Handbook of X-ray Photoelectron Spectroscopy",* Edited by Chastain J., Perkin-Elmer Corporation, Physical Electronics Division, Minnesota, United States of America.

23. Hoffman S., (2016) "*Surface and interface analysis*", Kirk-Othmer Encyclopedia of Chemical Technology, editor: Wiley.

24. Chusuei C. C., Goodman D. W., (2002) "*X-Ray Photoelectron Spectroscopy"*, Encyclopedia of Physical Science and Technology, pp. 921-938.

25. Schlesinger R., (2016) *"Theory of Experimental Methods"*.

26. Hou Z., Zhang X., Xiaona L., Zhu Y., Liang J., Qian Y., (2017) *"Surfactant widens the electrochemical window of an aqueous electrolyte for better rechargeable aqueous sodium/zin battery",* J. Mater. Chem. A., 5, 730.

27. Li M., (2019) "*Synthesis, Characterisation and Electrochemical study of Titanium Hexacyanoferrate Electrode material"*, unpublished master's thesis.

28. Ni G., Xu X., Hao Z., Wang W., Li C., Yang Y., Zhou C., Qin L., Chen W., Yao X., Cai J., (2021) "*Tuning the Electrochemical Stability of Zinc Hexacyanoferrate through Manganese Substitution for Aqueous Zinc-Ion Batteries"*, ACS Applied Energy Materials, 4, 602-610.

29. Musella E., Mullaliu A., Ruf T., Huth P., Tonelli D., Aquilanti G., Denecke R., Giorgetti M., (2020) *"Detailing the Self-Discharge of a Cathode Based on a Prussian Blue Analogue",* MDPI, Energies, 13, 4027.

30. Hendrickson D. N., Hollander J. M., Jolly W. L., (1969) *"Nitrogen N 1s Electron Binding Energies, Correlations with Molecular Orbital Calculated Nitrogen Charges",* Inorganic Chemistry, 2642.

31. A. Cano, J. Rodríguez-Hernández, L. Reguera, E. Rodríguez-Castellón, E. Reguera, (2019) *"On the Scope of XPS as Sensor in Coordination Chemistry of Transition Metal Hexacyanometallates",* European Journal of Inorganic Chemistry.

32. Lukas J., Lochmann L., Kalal J., (1990) *"An investigation of poly(tetrafluoroethylene) surfaces after etching with anion radicals by means of XPS photoelectron spectroscopy",* Die Angewandte Makromolekulare Chemie 181 (1990) 183 -190 (NK 3094).

33. Taylor A., M. Lancaster G., Wayne Rabalais J., (1978) *"Surface alteration of graphite, graphite monofluoride and teflon by interaction with Ar^+ and Xe^+ beams",* Application of Surface Science 1, 503-518.

34. Yatsimirskii K. B., Nemoshkalenko V. V., Nazarenko Yu. P., Aleshin V. G., Zhilinskaya V. V., Tomashevsky N. A., (1977) *"Use of X-Ray Photoelectron and Mössbauer Spectroscopies in the study of iron pentacyanide complexes",* Journal of Electron Spectroscopy and Related Phenomena, 10, 239-245.

35. M. Oku, (1993) *"X-Ray Photoelectron Spectroscopic Studies on the Kinetics of Photoreduction of Fe^{III} in Single-Crystal $K_3(Fe, Co)(CN)_6$ Surfaces cleaved in situ",* Journal of Chemical Society, vol. 89, no. 4, pp. 743-748.

36. Yamashita T., Hayes P., (2007) *"Analysis of XPS spectra of Fe^{2+} and Fe^{3+} ions in oxide materials"*, Applied Surface Science, 254, 2441-2449.

37. Maggay I. V. B., De Juan L. M. Z., Lu J. S., Mai T. N., Tetsu Y., Chan T. S., Liu W. R., (2018) *"Electrochemical properties of novel FeV_2O_4 as an anode for Na-ion Batteries"*, Scientific Reports, 8:8839.

38. Wang Y., Zhong H., Hu L., Yan N., Hu H., Chen Q., (2013) *"Manganese hexacyanoferrate/MnO_2 composite nanostructures as a cathode material for supercapacitors"*, Journal Mater. Chemistry A.

39. Langell M., Hutchings C. W., Nassir M. H., Carson G. A., (1996) *"High resolution electron energy loss spectroscopy of MnO (100) and oxidized MnO (100)"*, Journal of Vacuum Science and Technology A – Vacuum, Surfaces, and Films.

40. Audi A. A., Sherwood P. M. A., (2002) "*Valence-band x-ray photoelectron spectroscopic studies of manganese and its oxides interpreted by a cluster and band structure calculations",* Surf. Interface Anal., 33, 274-282.

41. Nefedov V. I., Salyn Ya. V., Leonhardt G., Scheibe R., (1977) "*A comparison of different spectrometers and charge correction used in X-ray Photoelectron Spectroscopy"*, Journal of Electron Spectroscopy and Related Phenomena, 10, 121-124.

42. Battistoni C., Dormann J. L., Fiorani D., Paparazzo E., Viticoli S., (1981) "*An XPS and Mössbauer study of the Electronic Properties of $ZnCr_xGa_{2-x}O_4$ Spinel Solid Solutions"*, Solid State Communications, Vol. 39, pp. 581-585.

43. Galmiz O., Stupavska M., Wulff H., Kersten H., Brablec A., Cernak M., (2015) "*Deposition of Zn-containing films using atmospheric pressure plasma jet"*, Open Chem., 13, 198-203.

44. Clark D. T., Feast W. J., Kilcast D., Musgrave W. K. R., (1973) *"Application of ESCA to Polymer Chemistry. III. Structures and Bonding in Homopolymers of Ethylene and the Fluoroethylenes and Detemination of the Compositions of Fluoro Copolymers",* Journal of Polymer Science: Polymer Chemistry Edition Vol. 11, 389-411.

45. Piwowarczyk J., Jędrzejewski R., Moszyński D., Kwiatkowski K., Niemczyk A., Baranowska J., (2019) *"XPS and FTIR Studies of Polytetrafluoroethylene Thin Films Obtained by Physical Methods",* Polymer (Basel), 1629.